d'Collection

Doctoral Thesis

Impedance Characterization and Synthesis for the EMC-Aware Design of AC Motors

Younggon Ryu

Department of Electrical Engineering

Graduate School of UNIST

2018

Impedance Characterization and Synthesis for

the EMC-Aware Design of AC Motors

Younggon Ryu

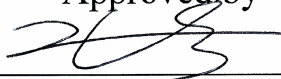Department of Electrical Engineering

Graduate School of UNIST

Impedance Characterization and Synthesis for

the EMC-Aware Design of AC Motors

A thesis

submitted to the Graduate School of UNIST

in partial fulfillment of the

requirements for the degree of

Doctor of Philosophy

Younggon Ryu

06. 14. 2018

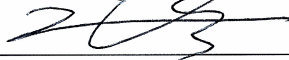Approved by

_____

Advisor

Jingook Kim

Impedance Characterization and Synthesis for

the EMC-Aware Design of AC Motors

Younggon Ryu

This certifies that the thesis of Younggon Ryu is approved.

06. 14. 2018
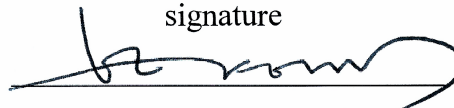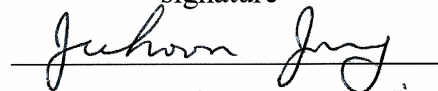
signature

_____

Advisor: Jingook Kim

signature

_____

Committee Member : Franklin Bien

signature

_____

Committee Member : Jee Hoon Jung

signature

_____

Committee Member: Katherine Ann Kim

signature

_____

Committee Member : Ki Jin Han

Abstract

These days, the pulse width modulation (PWM) inverter-fed drive is commonly used for the motor drive systems. As the switching speed increases, the fast rising and falling transients generate significant electromagnetic (EM) emission in the system, which can affect to other integrated devices. Since there are hundreds of turns in the winding structure, the ac motor operates as one of the main EM noise path in the system. Therefore, the study of the high-frequency characteristic for the ac motor, and design method of the ac motor to be robust against the electromagnetic interference (EMI) issues are getting important.

In this thesis, an electromagnetic compatibility (EMC) aware design method of an ac motor is presented by the network parameter analysis of the input impedance including the high-frequency coupling elements.

To estimate the high-frequency characteristics of the ac motor, an equivalent circuit modeling method is presented. From the wide-frequency response of the windings, the frequency-dependent per-unit-length (PUL) transmission line (*RLGC*) parameters are extracted, and a PUL equivalent circuit model is constructed by investigating the frequency characteristics of the *RLGC* parameters. Moreover, the shunt admittance model describing the stepwise decrease of capacitance is developed by applying Debye and Lorentz model. To verify the availability of the constructed equivalent circuit model, the input impedance and the transfer impedance for the entire length of the phase line are compared with the measurement. The input impedances matched with high accuracy over the wide-frequency region.

After establishing the equivalent circuit model for the phase winding structure of the ac motor, an extraction method of the six-port multi-network parameters for all the three-phase windings is presented because the phase-to-phase coupling may conduct EM noise by the excitation from the other phases. Under the assumption of a symmetric structure, the multi-port network parameters are obtained by the conversion of two-port mixed-mode network parameters, which include the relations between common-mode (CM) and differential-mode (DM). The method simplifies the calculation to extract the impedance parameters of the three-phase winding structure without the full six-port measurement. Furthermore, the phase-to-phase coupling can be estimated by the converted network matrices. In addition, the method is extended to the shaft structure to capture the winding-to-shaft coupling characteristics in the ac motor. The extracted impedance parameters include the coupling effects between CM noise, DM noise, and the end-sides of the shaft. For verification, the calculated impedances are compared with the measured input impedance for the phase line. The suggested multi-port network parameter extraction method can be used to estimate the EM coupling parameters between any structure part of the ac motor, CM noise, and DM noise by simple two-port mixed-mode network conversion.

Using the equivalent circuit model and multi-port network analysis method, a design method of the

EMC-aware ac motor is proposed by investigating the CM input impedance of the phase windings. The most effective coupling elements of the input impedance are defined with comparing the presented PUL equivalent circuit. Moreover, the electromagnetic (EM) field simulation including all the conductors of the ac motor is performed for the models of the separated parts of the ac motor structure. The multi-port networks are constructed from the EM simulation data, and the input impedance of the full-winding structure is extracted by the calculation of the network parameter matrices. The change of the input impedances due to the variation of the design parameters is studied through parametric analysis of the automated design code. By comparing the extracted input impedances for the different ac motor models, the EMC design method for the ac motor is established with considering the core loss and torque ripple together. To verify the design method, the CM current is measured for the redesigned ac motors when the motors are operating in the drive system. The result shows that the CM current is reduced up to 10dB by adjusting the motor design parameter. Consequently, the proposed method can predict the input impedance of the motor with high accuracy in the motor design stage before manufacturing. In addition, the proposed method can be applied to any type of ac motors and various design parameters.

Contents

List of figures

List of tables

Nomenclature

ASD	Adjustable Speed Drive
CE	Conducted Emission
CISPR	Comité International Spécial des Perturbations Radioélectriques
CM	Common Mode
EM	Electromagnetic
EMC	Electromagnetic Compatibility
EMI	Electromagnetic Interference
FE	Finite Element
IEC	International Electrotechnical Commission
LISN	Line Impedance Stabilization Network
PUL	Per Unit Length
PWM	Pulse Width Modulation
RE	Radiated Emission
S-parameter	Scattering Parameter
Z-parameter	Impedance Parameter

Chapter I

Introduction

1.1. The General Description of Electromagnetic Compatibility

These days, the electromagnetic compatibility (EMC) for the electromagnetic (EM) devices have been studying to minimize the undesired electromagnetic interference (EMI) issues caused by the high-frequency and the high-speed switching semiconductors, communication circuit or drive systems. The simple description of the EMI problem is shown in Fig. 1-1. The source is the device or system, which generates the EM emissions, and the victim is the equipment which affected the EM emissions. The EM emission is transferred from the source to the victim in two forms, conducted emission (CE) and radiated emission (RE). The classification of the CE and the RE are shown in Fig. 1-2. The CE is the internal EM emissions which is transferred in forms of voltage or current through the capacitive or inductive EM couplings in the system. The RE is the EM noise propagated as the EM field wave through the space. The EM devices are required to be designed so that the EM emission can satisfy the regulations specified in Comité International Spécial des Perturbations Radioélectriques (CISPR) or International Electrotechnical Commission (IEC). Recently, the compliance with these EMI regulations has been recognized as an essential requirement for the electrical devices, therefore the analysis of EM fields for the electrical devices or products in the design stage is becoming important.
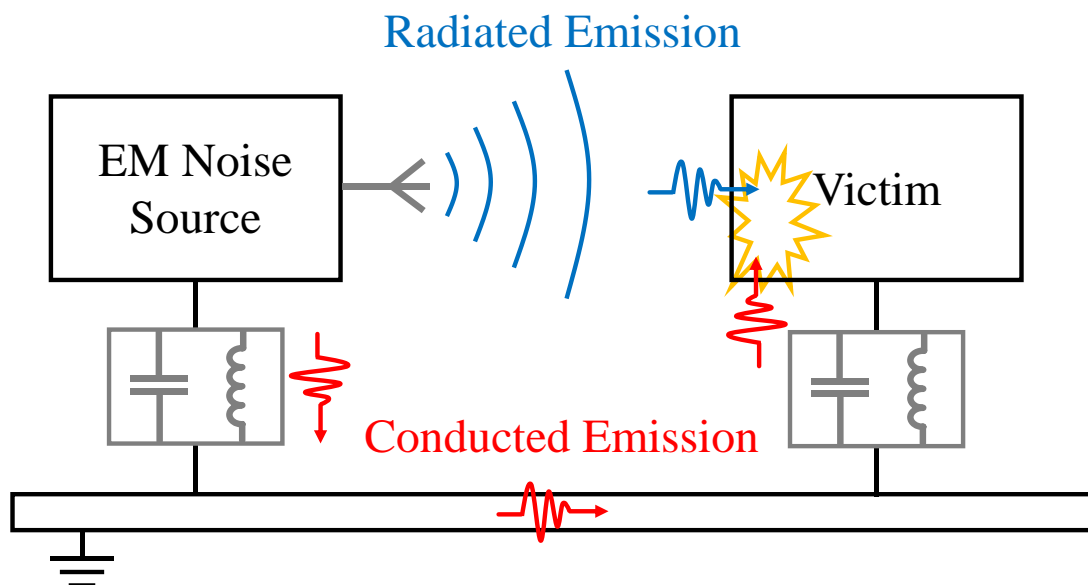
Fig. 1-1. The description of electromagnetic interference.
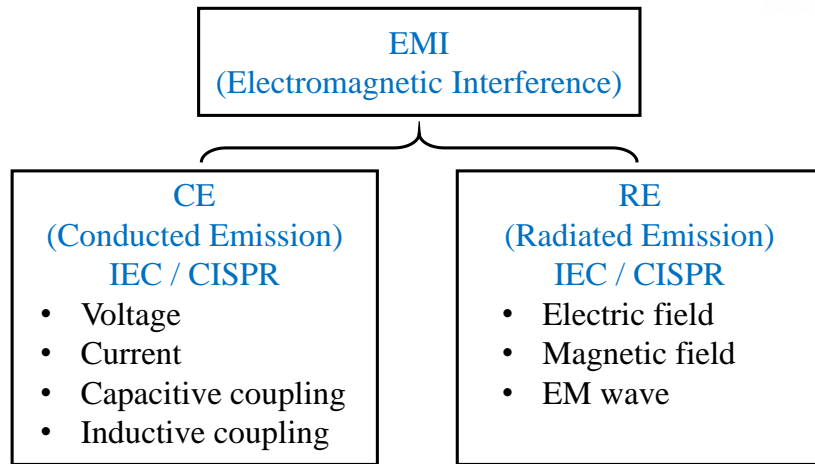
Fig. 1-2. The Classification of the electromagnetic interference.

1.2. EMI Issues in the Motor Drive System

Automotive EMI issues are one of the most urgent technical challenges among the EMC applications. As the automobile electric system evolves into a smart system with the information and the communication technology, various integrated circuits and sensors are mounted, which increases the sensitivity to the EM noise. Moreover, the EMI problems in the electric vehicles are associated with the high-power systems, such as the smart grids or the motor drive system. Therefore, the high-power EM noise generated in the motor drive system can be transmitted to the other electrical circuit devices in the electric vehicle.

$$i_{CM} = C \frac{dv}{dt}$$
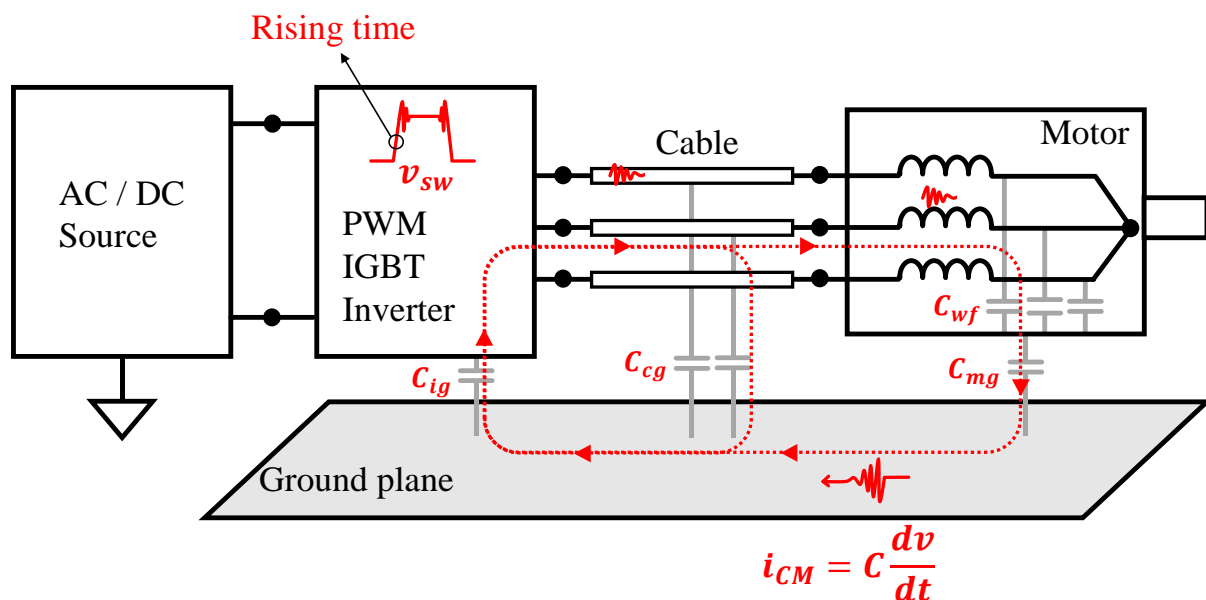
Fig. 1-3. The electromagnetic interference issues in the motor drive system.

The schematic description of the EMI problem in the adjustable speed drive (ASD) system is shown in Fig. 1-3. To obtain the variable frequencies for the speed control, pulse width modulation (PWM) drive is commonly used. As the switching frequency of the inverters increases, the rising and the falling transients become shorter, and the rapid changes generate high dv/dt, which causes serious EMI issues in the motor drive system. The produced high-frequency harmonics flow to the ac motor through the terminal cables. The generated common-mode (CM) current forms a loop through the parasitic couplings, and it may interfere with the operation of the other electrical devices while cycling the motor drive system through the reference ground.

The measured line-to-line voltage of a 200HP ac motor which is driven by the PWM ASD is shown in Fig. 1-4 (a) [1]. The green-dot line is the traditional line-frequency of the sinusoidal 60Hz. Comparing the two waveforms, the modulated signal by the ASD has many elements of the high dt/dv that generates the high-frequency harmonics. The produced CM current by the high-frequency harmonics in the motor drive system is shown in Fig. 1-4 (b). The generated CM current can be transmitted to the other equipment through the CM ground. Since the CM current is generated by the high-power system, it can have high peaks (10~20A in the Fig. 1-4), therefore it can damage not only the inverter or the ac motors but also the other sensitive circuit devices which is integrated with the motor drive system.
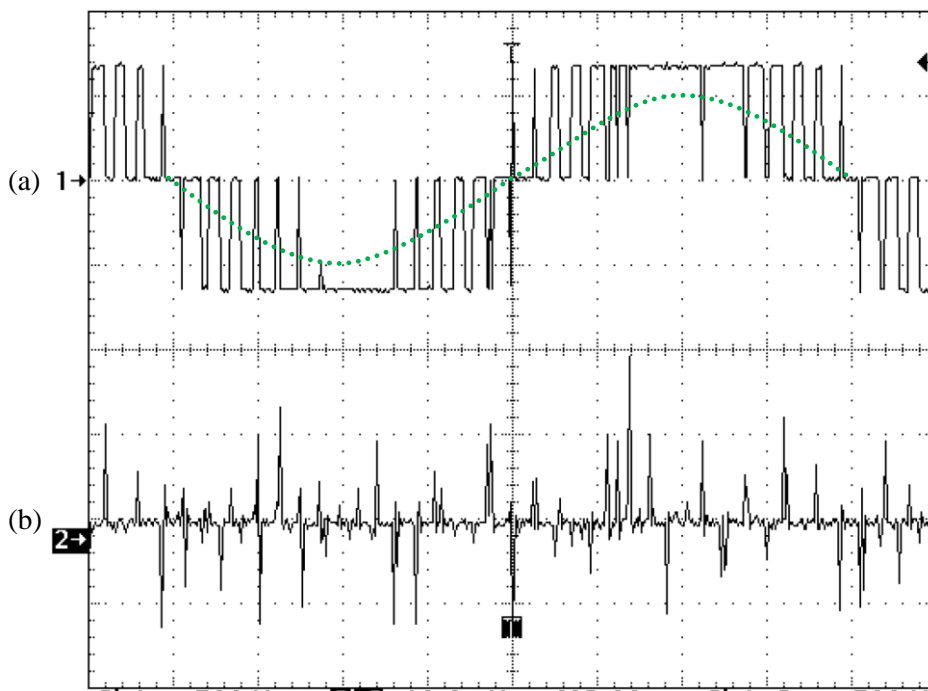
Fig. 1-4. The measured line-to-line voltage and CM current in the 200HP ac motor drive system (2ms/Div.) [1]. (a) The pulse-width-modulated line-to-line voltage in the ac motor. (500V/Div.) (b) The CM current in the system. (10A/Div.)

The measured CM current at each part of a 0.75kW induction motor drive system is shown in Fig. 1-5 [2]. The peak of the inverter-to-ground CM current is about 0.5A, while the motor-to-ground CM current is almost 0.7 A which is larger than the inverter-to-ground CM current. Therefore, the measured total CM current is almost 1.2 A. From the measured results of the parts of the CM currents, we can know that although the EM noise is generated in the inverter drive by PWM switching, the overall CM current in the system is highly dependent on the ac motor structure and the CM input impedance characteristics.
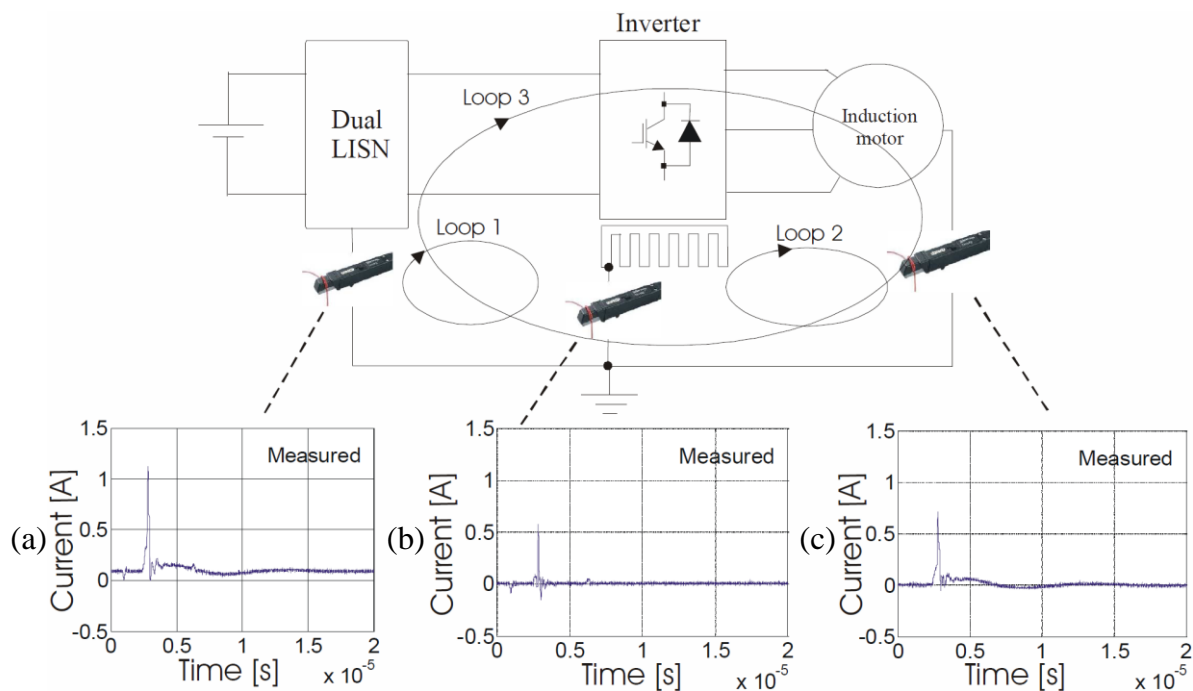
Fig. 1-5. The measured CM current at each part of a 0.75kW induction motor drive system [2]. (a) Total CM current in the system. (b) Inverter-to-ground CM current. (c) Motor-to-ground CM current.

The breakdown and the insulation failure in the motor drive system due to the high-frequency harmonics are shown in Fig. 1-6. In the high-frequency region, there is an antiresonance that the input impedance of the ac motor becomes very low as shown in Fig. 1-6 (a). If the high order harmonic frequencies which is generated from the PWM inverter switching close to the lowest impedance at antiresonant frequency, the insulation failure of the stator winding structure of the ac motor is occurred. The interwinding insulation failure and the winding-to-stator insulation failure in the stator winding structure of the ac motor due to the surge voltages are shown in Fig. 1-6 (b). To prevent from these insulation failures, the ac motor should be designed to be endurable for the high peaks of the generated harmonics. Therefore, the high-frequency parameters of the ac motor should be defined firstly to design

the ac motor having high input impedance. For that, establishing an accurate equivalent model which include the high-frequency parameters is important to investigate the characteristics of the input impedance of the ac motor.
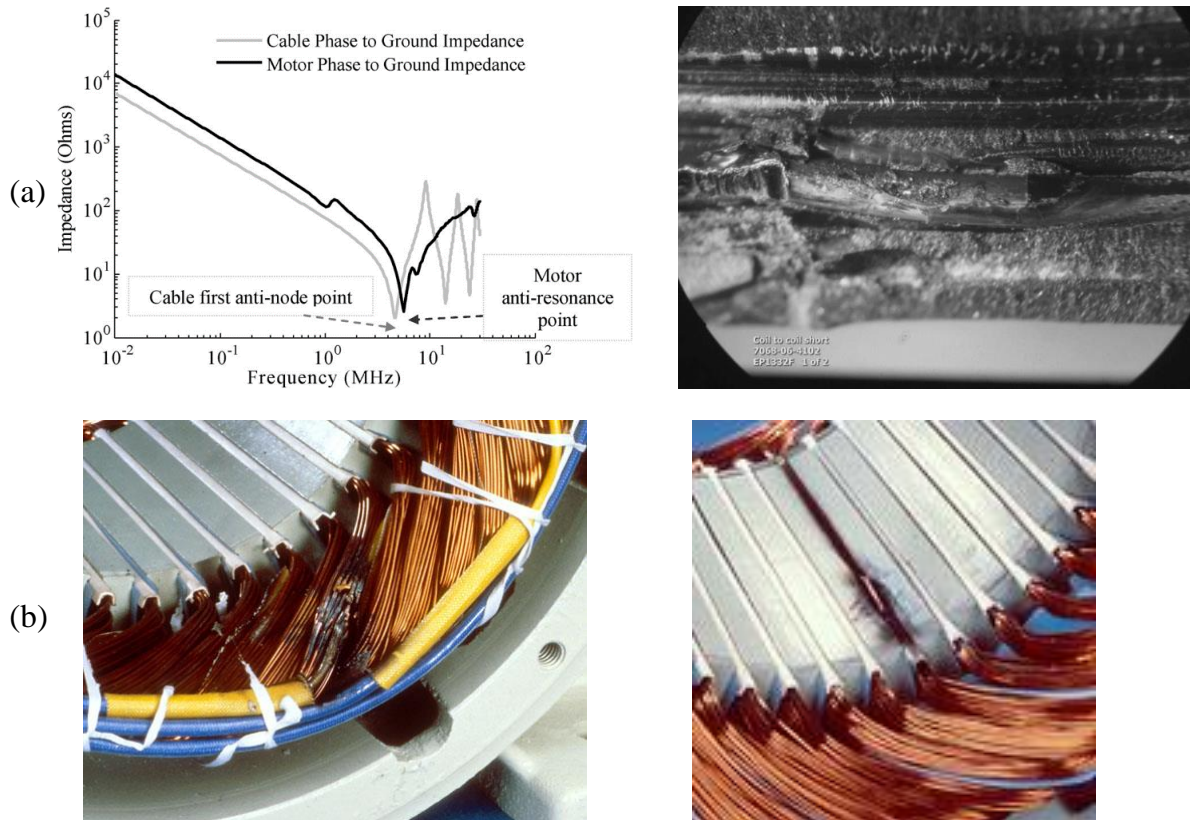
Fig. 1-6. The input impedance of an ac motor and the insulation failures. (a) The input impedance including high-frequency antiresonance in the ac motor, and the interwinding insulation failure [3]. (b) The interwinding insulation failure and the winding-to-stator insulation failure in the stator winding structure of the ac motor due to the surge voltages [4].

1.3. Coupling Mechanism of the Stator Winding Structure

In order to construct the equivalent circuit model and extract the characteristics of the input impedance of the ac motor, an analysis of the EM coupling mechanism inside the ac motor structure is necessary. The structures of the disassembled ac motor are shown in Fig. 1-7 to investigate the EM coupling mechanism. Fig. 1-7 (a) shows the fully assembled ac motor, and Fig. 1-7 (b) shows the stator winding structure inside of the enclosure frame. The slot-winding structure which is the cross-section of the stator winding structure is shown in Fig. 1-7 (c), and the simplified end-winding structure is

shown in Fig. 1-7 (d).

In the slot-winding structure, there are a number of coils and windings which have tens or hundreds of turns. Therefore, the interwinding coupling can be one of the important EM coupling characteristics of the stator winding structure. Another coupling element is called the winding-to-frame coupling, which forms a path through the back yoke to the motor frame as a ground. This element is the main component of the path of the CM current, therefore it must be considered carefully in the equivalent circuit model. The last one is the phase-to-phase coupling if the motor is designed as a double-layer winding structure.

In the end-winding structure, the winding-to-frame coupling is smaller than that in the slot winding because the space between the winding and the frame is much larger. However, the phase-to-phase coupling is not negligible because the phase windings are crossed each other in the end winding. The interwinding coupling also can be the important element in the end-winding structure by the continuing turns from the slot-winding.
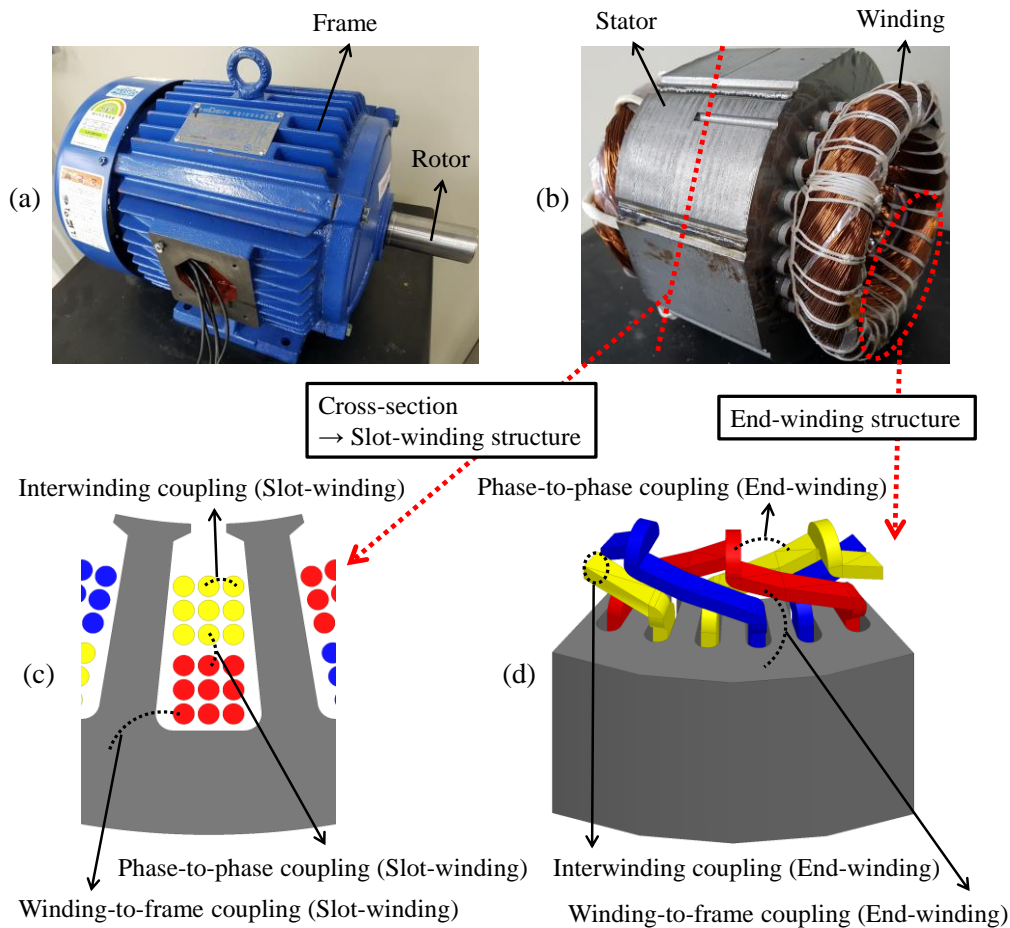
Fig. 1-7. (a) The fully assembled ac motor. (b) The stator winding structure. (c) The EM coupling mechanism in the slot-winding structure. (d) The EM coupling mechanism in the end-winding structure.

1.4. Previous Researches

The study of the EM emission which is generated in the motor drive system has been recognized as an important research topic from 1990s, as the switching speed of the drive circuit increases. The effects of the high-frequency oscillation at the ac motor terminals by the high-speed PWM switching have been studied [5-7]. A technique to calculate the interturn voltages in the winding structure during the transient condition is described in 1995 [5]. Moreover, a concept of the network modeling for the transient over-voltage associated with the PWM-fed ac machine is presented in 1998 [6]. In addition, the effect of the PWM voltage waveform on the voltage distribution among the stator windings in an induction motor is studied in 1999 [7].

In the 2000s, several studies have been proposed to reduce the EM noise in the ac motor drive system. The design methods to reduce the CE noise in the inverter were introduced in [8-10]. In addition, the studies on the development of the CM filters were conducted [11-12]. However, even if these researches investigate the high-frequency characteristics by observing time-domain responses and ringing for the inverter drive, the EM emission for the ac machine was not their focus. To solve the EMI issues effectively in the entire ac motor drive system, not only the circuit device but also the EM characteristics of the motor should be considered as discussed in Fig. 1-5 and Fig. 1-6. Furthermore, due to the structural changes in the inverter or the additional filters, the size and cost of overall circuit device may increase. Therefore, the EMC design method for the ac motor should be established. However, the EMC design for the ac motor is not easy because there is not enough degree of freedom of design in the complete mechanical structure of the ac motor. Therefore, for an efficient EMC motor design, the EMI characteristics of the ac motor should be analyzed firstly, which requires an equivalent circuit model including the high-frequency effects.

To understand the high-frequency behavior of the ac motors, the traditional low-frequency equivalent circuit model should be modified by including various parasitic EM coupling elements of the winding structure. For that, the high-frequency ac machine models have been proposed over the years. A number of the equivalent circuit models of previous studies were constructed by including the turn-to-turn mutual couplings [13-17]. However, these proposed distributed-parameter models are too complicated because of a lot of mutual elements as shown in Fig. 1-8, and some of them are not easy to calculate without finite element (FE) calculation. Moreover, the proposed models are not enough to understand the high-frequency characteristics because the frequency range of these models is limited to below the high-frequency antiresonance [18-19]. In addition, several measurement-based equivalent models shown in Fig. 1-9 provide a good correlation with the measured input impedances from low to high frequency [20-24]. In these high-frequency equivalent circuit models, the high-frequency parameters

are defined from the measured resonant frequencies and curve fitting of the CM input impedance. However, the physical meaning of some elements is not clear, and the elements are difficult to calculate and determine. Moreover, the measurement-based methods cannot be used to predict the high-frequency characteristics during an initial motor design stage before prototyping. Therefore, a new equivalent circuit modeling method of the ac motor is required, which can identify all the physical characteristics of the winding structure clearly.
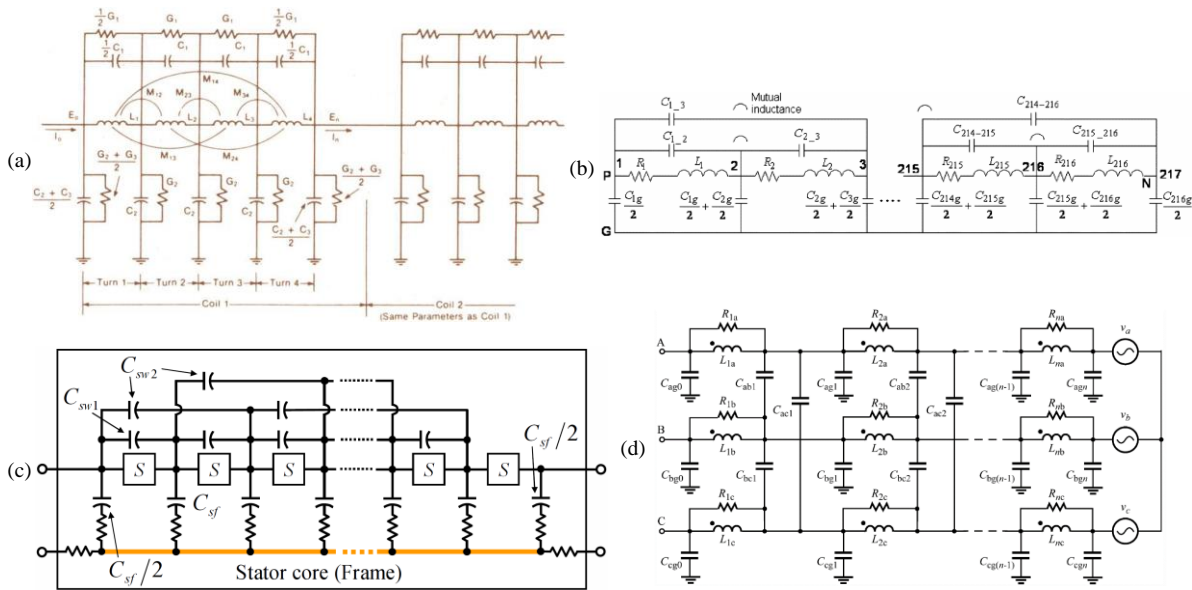
Fig. 1-8. The distributed-parameter models including high-frequency elements for the winding structure of the ac motor. (a) Turn, coil, and winding circuit [13]. (b) Distributed-parameter winding circuit obtained from FE analysis [14]. (c) Equivalent circuit of one coil of stator windings [15]. (d) Coupled three-phase equivalent circuit model of an electric machine [17].
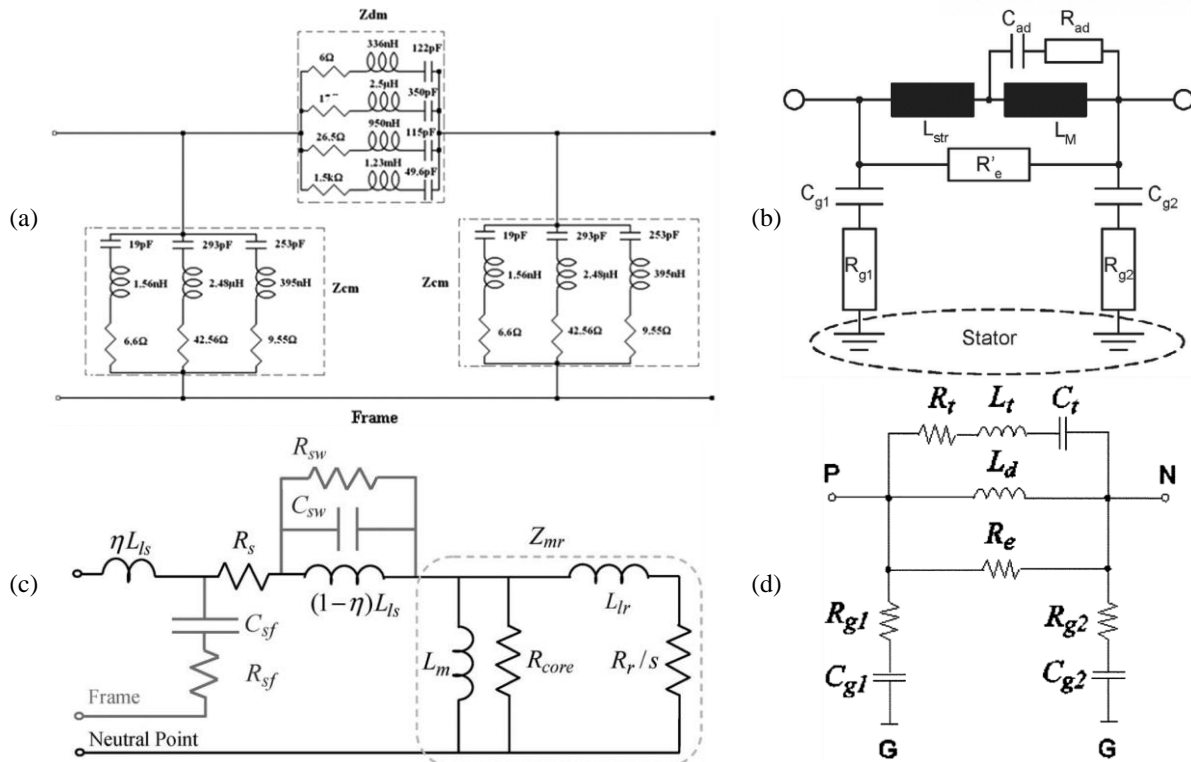
Fig. 1-9. The lumped-parameter models by curve fitting from measured data. (a) Per phase equivalent circuit of the motor winding [21]. (b) Extended per phase circuit [20]. (c) Universal model of induction motor per phase [23]. (d) High-frequency per-phase motor equivalent circuit [24].

After establishing an accurate equivalent circuit model including the high-frequency couplings in the ac motor structure, the EM field calculation for the realistic ac motor structure as shown in Fig. 1-10 (a) is essential to predict the high-frequency characteristics in the motor design stage. However, the EM simulations for the motor structures have been generally used in the studies to analyze the operating characteristics with only single bulk conductor for the winding structure as shown in Fig. 1-10 (b). The typical EM simulation models for the motor structure are not suitable to predict the high-frequency effects because the EM field should be calculated for all the conductors to estimate the interactive EM coupling effects in the winding structure.

A number of studies considering the individual conductors in the winding structure have been conducted to predict the CM input impedance of the ac motor [25-29]. The physical models are constructed based on FE analysis to predict the high-frequency characteristic of ac motor in [25-27], and the constructed models are studied for the transient response; however, the distributed-circuit models are not easy to apply to a lot of winding turns. In [28], the RLC parameters for the detailed slot-winding structure are calculated by transmission line model. The physical calculation of all the coupling parameters is described well, but the complicated parameter matrix may be difficult to apply any type

9

of slot-winding structure. A method to predict the CM impedance of the stator winding is presented in [29]. The lumped parameters of the circuit model are defined well with considering geometrical parameters of the stator winding structure, and the calculated CM impedance are matched reasonably with the measurement. However, the extracted impedances are only compared in a limited area where does not include the high-frequency antiresonance, which is important factor of the EMI characteristics of the motor [3]. Therefore, establishing a method that accurately predicts the high-frequency characteristics for the complicated winding structure in the wide-frequency is indispensable to design the ac motor which is strong against EMI issues, before the ac motor is manufactured.
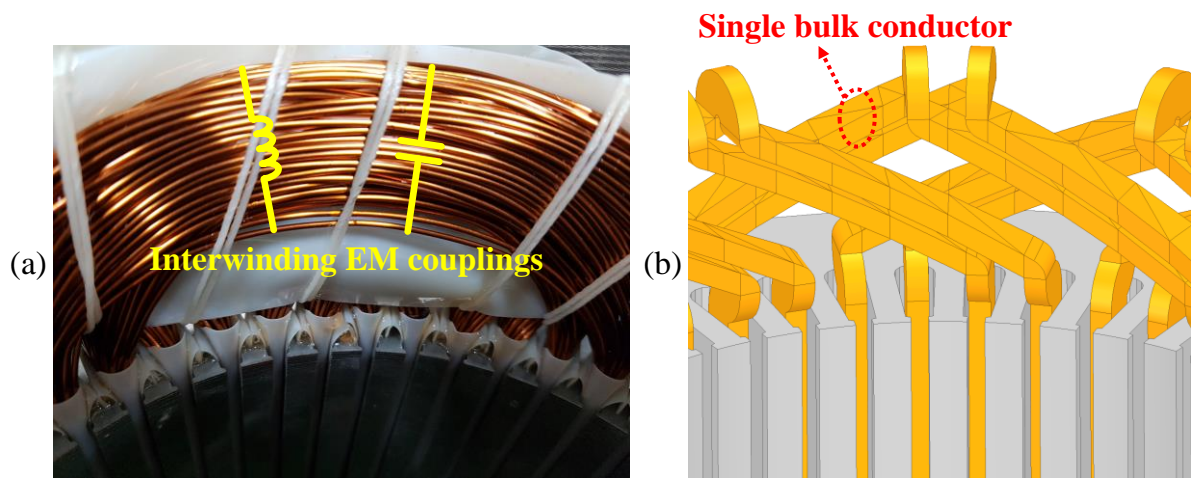
Fig. 1-10. (a) The real motor winding structure with the interwinding couplings. (b) The typical model of the motor winding structure for the EM field calculation.

1.5. Objective of This Work

In this thesis, a design method of an EMC-aware ac motor is proposed by characterizing the CM input impedance of the winding structure. The summarized procedure of this study is shown in Fig. 1-11. To determine the EM coupling factors which affect motor input impedance, an equivalent circuit modeling method that evaluates all coupling elements generated in the ac motor structure is presented by applying transmission line model. All the values of the elements in the equivalent circuit model can be defined from the extracted transmission line parameters. The accuracy of the established equivalent circuit model is verified by comparing with the measured input impedance of an induction motor.

To consider the EM coupling effect for the three-phase windings, a multi-port network parameter extraction method is constructed. The multi-port network parameters of the three-phase winding structure can be extracted by using a conversion method of two-port mixed-mode network. By using

the proposed extraction method, it is possible to investigate not only the input impedance and the transfer impedance of each phase winding, but also all the interaction EM coupling characteristics of the three-phase winding structure.

To predict the characteristics of the input impedance of the ac motor in the design stage, an EM field analysis method considering all the realistic winding structure is presented. The *RLGC* raw matrix data for all conductors of the winding is extracted by EM field simulation, and the impedance characteristic for the phase winding is extracted through the multi-port network construction by the proposed method. Moreover, the structural elements of the ac motor corresponding to the EM coupling parameter affecting mostly the input impedance of the motor are determined from the proposed equivalent circuit model. Finally, the method for the EMC-aware motor design is presented by investigating the variation of the input impedance due to the change of the design parameter which is related to the main structural elements for the EM couplings.
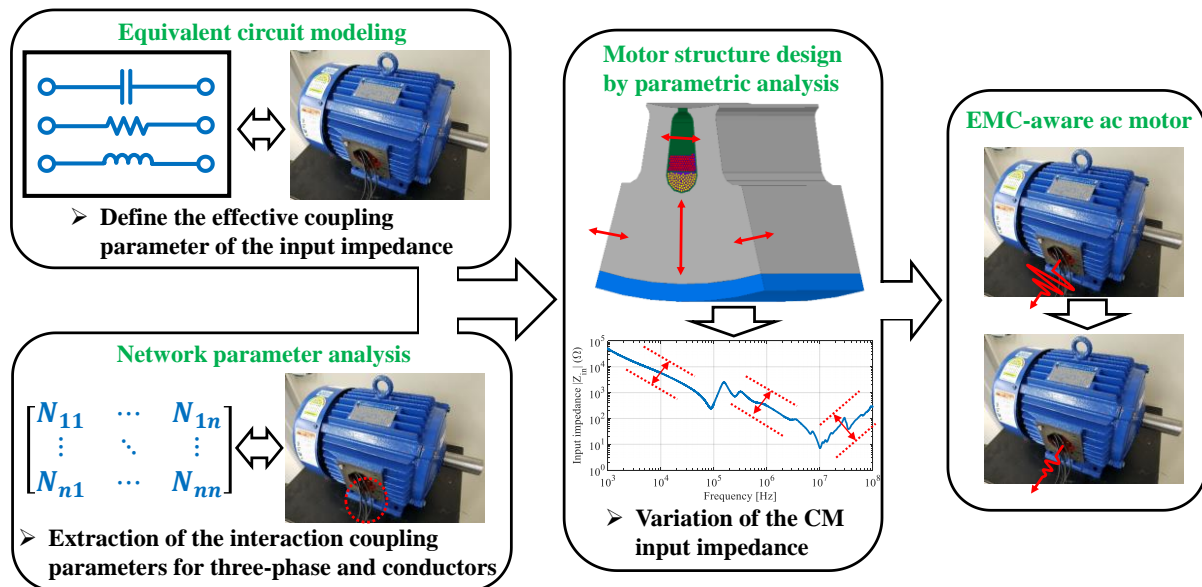
Fig. 1-11. The procedure summary of this research.

In Chapter II, the equivalent circuit modeling method generated from transmission line model is proposed to facilitate the high-frequency parameter extraction for the winding structure of the ac motor. From analysis of the propagation constant (γ) and characteristic impedance (Z_c) for the phase winding of the ac motor, per-unit-length (PUL) *RLGC* transmission line parameters are extracted. The PUL equivalent circuit models estimate the high-frequency characteristics of the motor stator winding structure through investigation of the characteristics of the extracted *RLGC* parameters. Moreover, the PUL equivalent circuit model is improved to consider the different characteristic of the admittance in

the high-power motor. To construct the PUL admittance model precisely, Debye and Lorentz model is applied. The resistance of the insulation sheet is also modeled in the improved admittance model by analysis of the PUL conductance. In addition, the series PUL impedance model is enhanced by including the skin effect of the winding conductors. The accuracy of the proposed PUL equivalent circuit model is verified by comparison of the input impedances with the measurement results.

In Chapter III, a method that extracts the multi-network parameter of the ac motor is proposed from the characterization of the mixed-mode network parameters (conversion of common-mode network and differential-mode network). Under the assumption of the symmetry of windings, the proposed method enables the creation of the multi-port network parameter, including couplings, without a full six-port measurement for the three-phase windings. In addition, a simple modeling method which can distinguish the phase-to-phase coupling from the self-coupling in the phase winding is presented by using the extracted multi-network parameters. Therefore, the influence of the phase-to-phase coupling for the phase line can be investigated by comparing the input impedances of coupled and uncoupled models.

In Chapter IV, the EMC-aware design method of the ac motor is proposed by extraction of the input impedances of the phase windings. To predict the EM characteristic of the winding structure, it is modeled separately in several parts, slot-winding structure, end-winding structure and external line structure in the EM simulation. The input impedance of the full-winding structure including all the conductors is extracted by calculation of the cascaded multi-port network parameter matrices of the simulated structure parts. The prediction method of the input impedance is verified by comparison with measurement in the wide-frequency area. Moreover, the variation of the input impedance depending on the motor design parameters are investigated through automated design code. The initial design parameters for the parametric analysis are number of slots, poles, parallel conductors and parallel circuits. Then, all the modeling and calculation procedures are conducted automatically by the design code. The EMC design method of the ac motor is presented by the analysis of the input impedances of the ac motor models extracted by the different design parameters. The general motor operation characteristics, such as core loss and torque ripple are also considered together. To validate the EMI characteristics of the modeled ac motors, an experiment is conducted by measuring the redesigned prototype motors which has different number of the parallel circuits, one of critical design parameter for the input impedance. The CM currents are measured when the produced ac motors are operating in the motor drive system. From the characteristic of the CM current, the design method of the EMC-aware motor is verified.

Chapter II

Equivalent Circuit Modeling Method Including the High-Frequency Parasitic Couplings for the Stator Winding Structure

2.1. Introduction

The image descriptions of the winding structure in the ac motor is shown in Fig. 2-1 [30]. As shown in the figure, the phase windings of the ac motor are usually wound symmetrically on the stator. The phase windings consist of several coils, and the coils also have tens of turns. Therefore, the phase winding is generally made by a long conductor line which is tens or hundreds of meters in the length. Consequently, the phase winding is a long transmission line, therefore the transmission line theory can be an effective method to analyze the EM characteristics of the winding structures.

The basic concept of the transmission line theory is shown in Fig. 2-2 [31]. The infinitesimal length of a transmission line in Fig. 2-2 (a) can be modeled as a lumped-element circuit in Fig. 2-2 (b). The R, L, G, and C are the series resistance, series inductance, shunt conductance, and shunt capacitance respectively, in meter. From the PUL $RLGC$ elements, the propagation constant (γ), and the characteristic impedance (Z_c) can be defined as follows:

$$\gamma = \sqrt{(R + j\omega L)(G + j\omega C)} \tag{2.1}$$

$$Z_c = \sqrt{\frac{R + j\omega L}{G + j\omega C}} \tag{2.2}$$

Since the propagation constant and characteristic impedance can also be represented by the network parameters, such as scattering (S) or impedance (Z) parameters, they can be useful for EM analysis of the three-phase terminals.
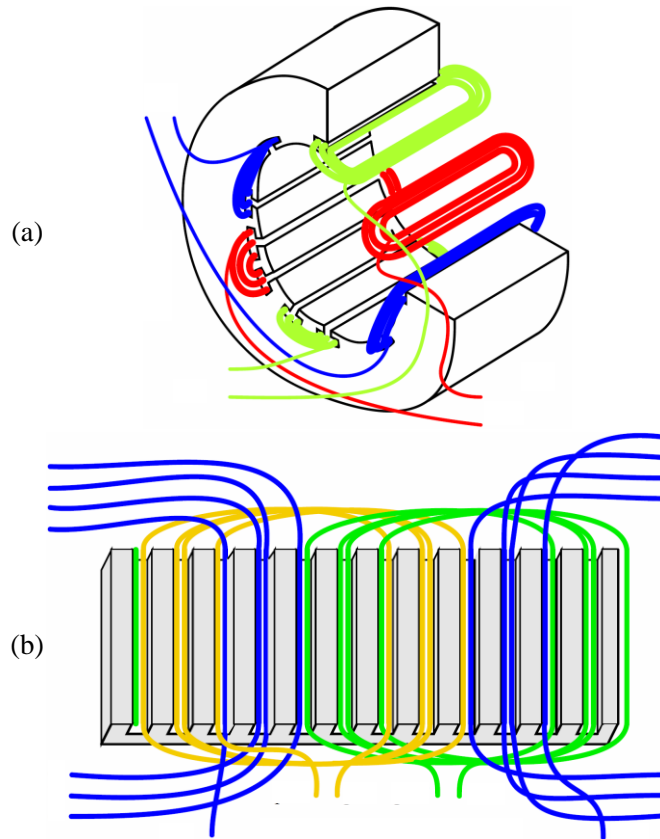
Fig. 2-1. (a) The schematic of the three-phase windings of an ac motor. (b) An image of the unfolded slot structure.
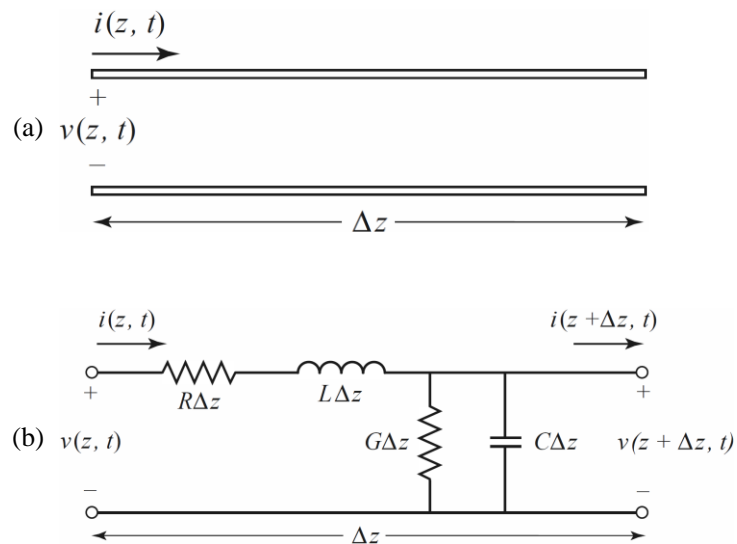
Fig. 2-2. Voltage and current definitions and equivalent circuit for an incremental length of transmission line. (a) The voltage and current of the transmission line. (b) Lumped-element of the PUL *RLGC* equivalent circuit.

2.2. Extraction of the Transmission Line Parameters for the Stator Winding Structure

This section presents, how to apply the transmission line model to the phase winding structure. First, some simple winding structures of an ac motor are simulated by EM field simulation to extract the S-parameters as the raw data as shown in Fig. 2-3 (a). The simulation is implemented for three cases as one conductor, three conductors, and ten conductors in a slot. Assigning the end sides of each conductor as ports and the stator core as a ground, the S-parameter matrices of slot conductors can be obtained for the wide-frequency region. By importing the simulated slot structure models and connecting them in a circuit simulator as shown in Fig. 2-3 (b), the two-port S-parameters can be obtained for a coil winding structure. The figure shows to construct the most complex ten turns winding structure among the simulation models, and the other winding models, one turn and three turns, also can be constructed in the same way.
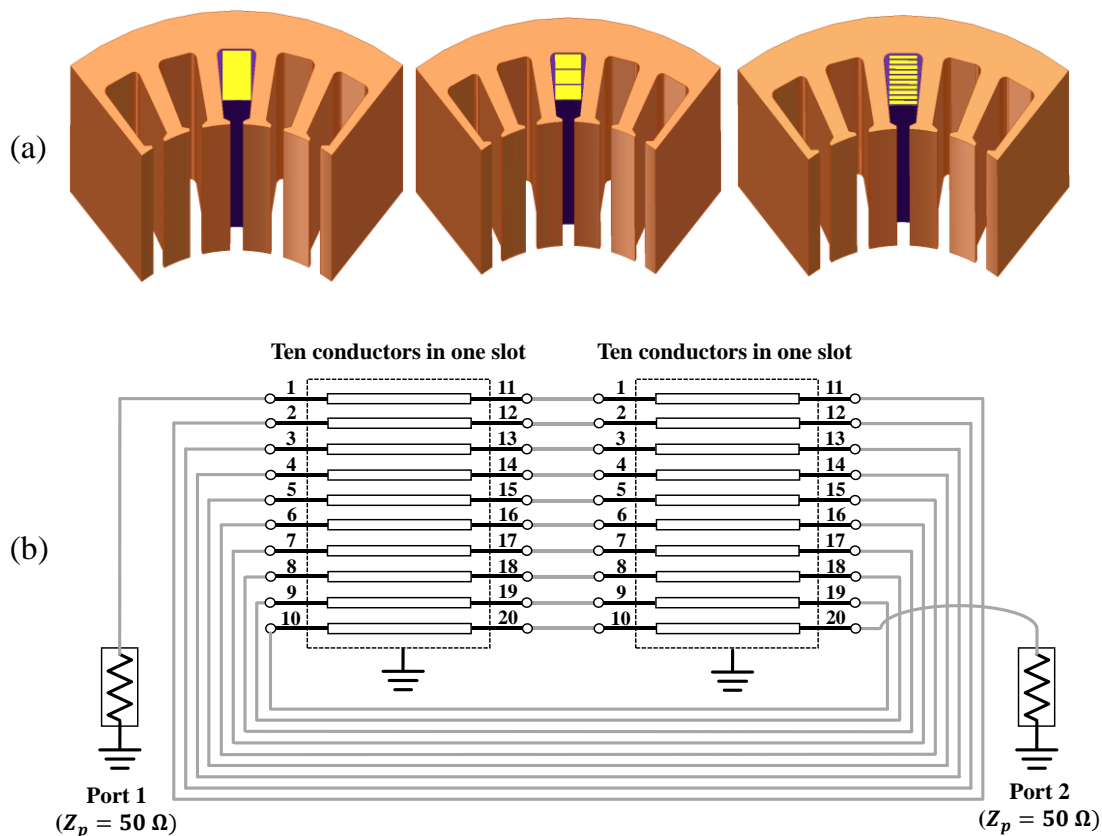
Fig. 2-3. (a) The simulated winding structures for one turn, three turns, and ten turns in a slot by 3D EM field simulation. (b) The circuit connections to construct ten turns of a winding structure by a circuit simulator.

The propagation constant and the characteristic impedance can be calculated from the raw-data of the S-parameters of the simulated winding structures by using the conversion method of the two-port network parameters [31-32]. By the relation between the transmission parameters (ABCD) and S-parameter matrices, the propagation constant and characteristic impedance are obtained as follow:

$$\begin{bmatrix} A & B \\ C & D \end{bmatrix} = \begin{bmatrix} \cosh(\gamma l) & Z_c \sinh(\gamma l) \\ \dfrac{1}{Z_c}\sinh(\gamma l) & \cosh(\gamma l) \end{bmatrix}$$
$$= \begin{bmatrix} \dfrac{(1+S_{11})(1-S_{22})+S_{12}S_{21}}{2S_{21}} & Z_p\dfrac{(1+S_{11})(1+S_{22})-S_{12}S_{21}}{2S_{21}} \\ \dfrac{1}{Z_p}\dfrac{(1-S_{11})(1-S_{22})-S_{12}S_{21}}{2S_{21}} & \dfrac{(1-S_{11})(1+S_{22})+S_{12}S_{21}}{2S_{21}} \end{bmatrix} \qquad (2.3)$$

where, l can be the total length of the phase line, and Z_p is the reference port impedance that is normally set 50Ω. The hyperbolic sine and the hyperbolic cosine functions can be calculated by the exponential functions with considering the propagation constant and length as follows:

$$\cosh(\gamma l) = \frac{e^{\gamma l} + e^{-\gamma l}}{2}, \quad \sinh(\gamma l) = \frac{e^{\gamma l} - e^{-\gamma l}}{2} \qquad (2.4)$$

Through the calculation of the relations between (3) and (4), The propagation constant and characteristic impedance expressed by the S parameters can be extracted as follows:

$$\gamma = \frac{1}{l}\ln\left(A \pm \sqrt{BC}\right)$$
$$= \frac{1}{l}\ln\left(\frac{(1+S_{11})(1-S_{22})+S_{12}S_{21}}{2S_{21}} \pm \sqrt{\frac{\left((1+S_{11})(1+S_{22})-S_{12}S_{21}\right)\left((1-S_{11})(1-S_{22})-S_{12}S_{21}\right)}{(2S_{21})^2}}\right)$$

$$(2.5)$$

$$Z_c = \pm\sqrt{\frac{B}{C}} = \pm Z_p\sqrt{\frac{(1+S_{11})(1+S_{22})-S_{12}S_{21}}{(1-S_{11})(1-S_{22})-S_{12}S_{21}}} \qquad (2.6)$$

Since the calculated propagation constant and characteristic impedance through (5) and (6) involve multiple values, their solutions are not only one. Therefore, the physically reasonable values should be chosen carefully. To find the reasonable value of the propagation constant, the positive attenuation

constant (α) should be selected among the solutions because the other one is for the wave traveling in the negative direction. The calculated solutions and the selected value of attenuation constant for the ten turns winding structure are shown in Fig. 2-4. As the propagation constant is the value of logarithmic function of a complex number, the phase constant (β) has the infinite number of solutions. To select the proper values of the phase constant, the travelling phase values of S-parameters from -180° to 180° are unwrapped to be continuous. By using the modified S-parameters, the available value of the phase constant can be extracted. The calculated solutions and the corrected values of the phase constants for the ten turns winding structure are shown in Fig. 2-5.
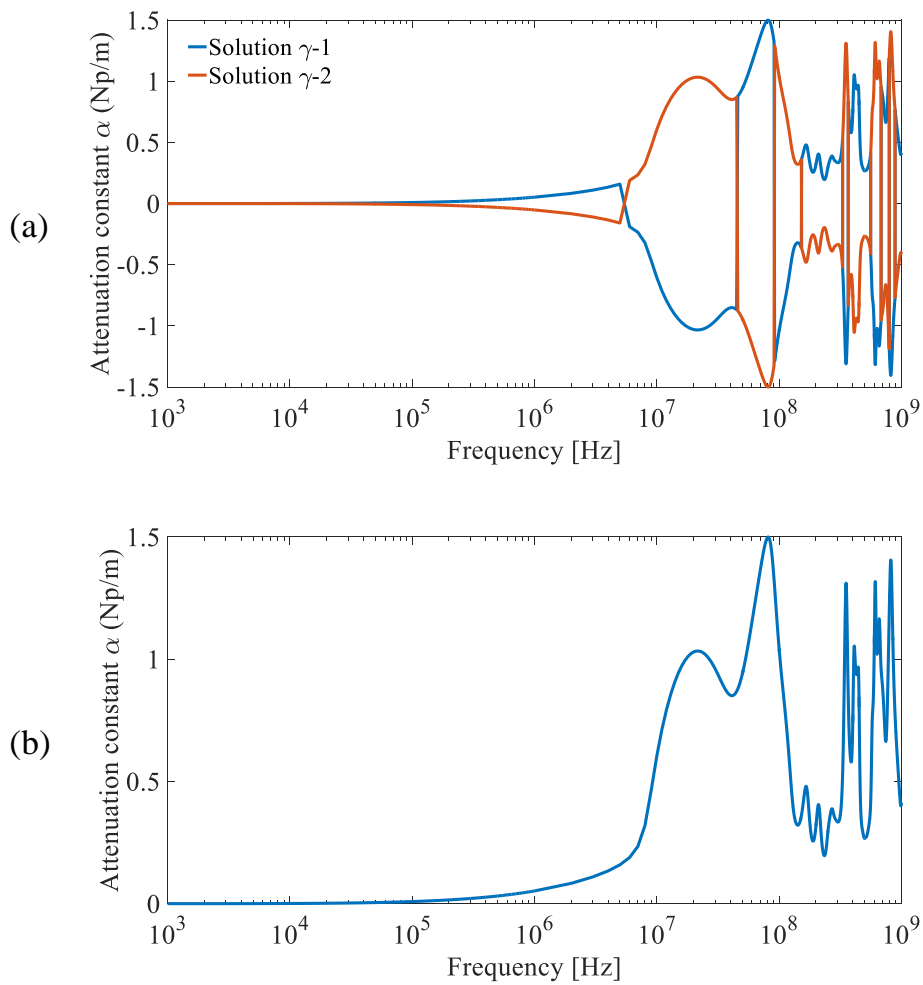
Fig. 2-4. (a) The calculated solutions of the attenuation constant for ten turns winding structure. (b) The corrected real solution of the attenuation constant for the ten turns winding structure.
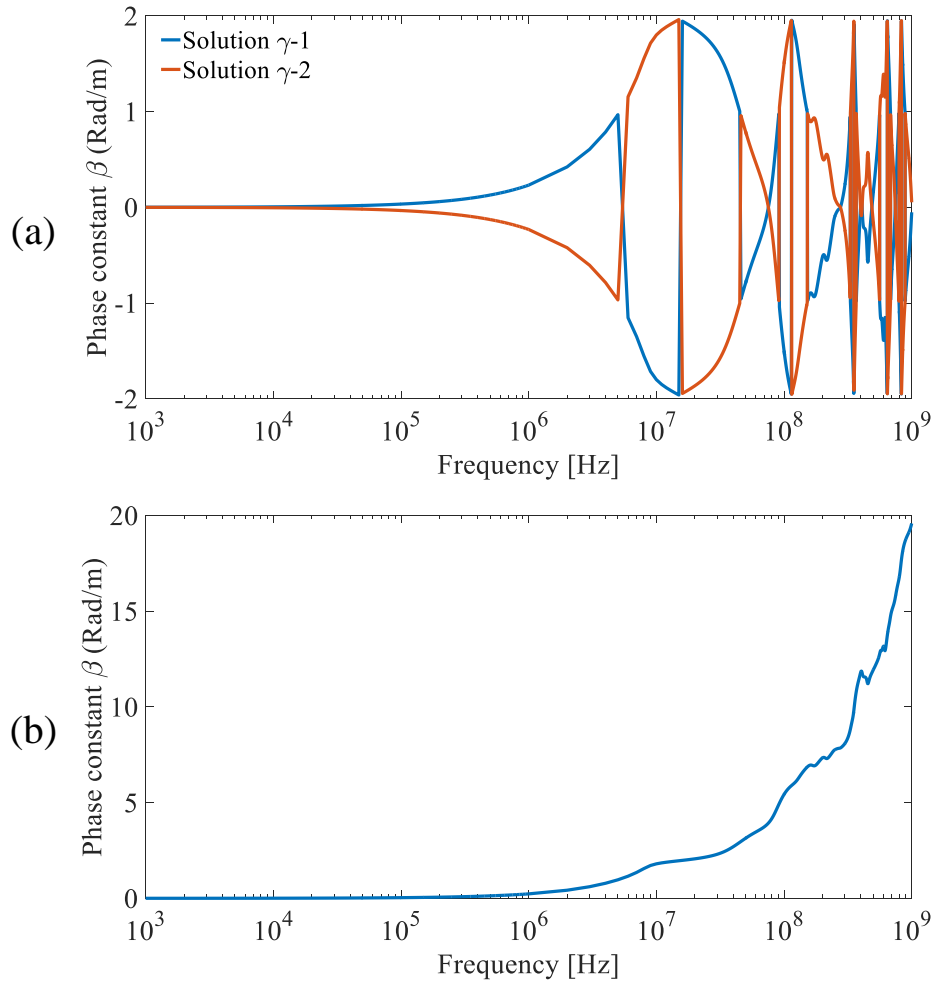
Fig. 2-5. (a) The calculated solutions of the phase constant for ten turns winding structure. (b) The corrected and unwrapped solution of the phase constant for the ten turns winding structure.

For the characteristic impedance, the solution should be selected so that its real value is positive to maintain the passive characteristic of the stator winding. The calculated solutions for the characteristic impedance by (2.6) are shown in Fig. 2-6.
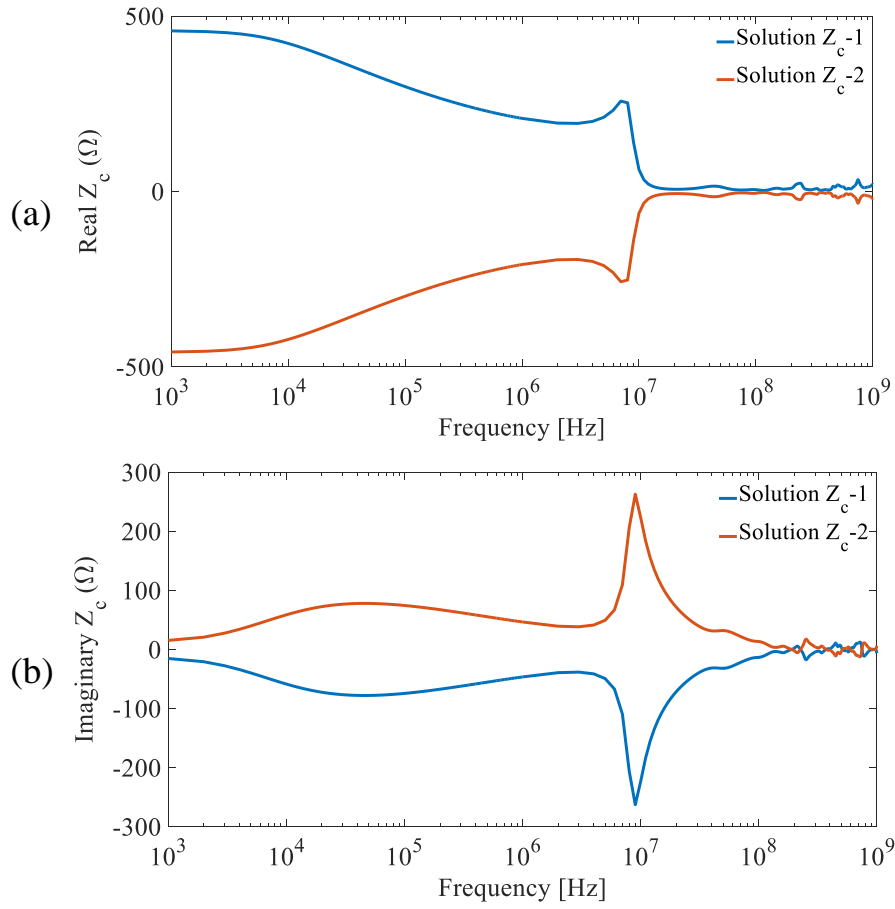
Fig. 2-6. (a) The calculated solutions of the real part of characteristic impedance for ten turns winding structure. (b) The calculated solutions of the imaginary part of characteristic impedance for ten turns winding structure.

Once the values of the propagation constant and characteristic impedance are defined, finally the PUL RLGC parameters can be obtained by following formulas:

$$R_{PUL} = \Re(\gamma Z_p), \quad L_{PUL} = \frac{\Im(\gamma Z_p)}{\omega}, \quad G_{PUL} = \Re\left(\frac{\gamma}{Z_p}\right), \quad C_{PUL} = \frac{\Im\left(\dfrac{\gamma}{Z_p}\right)}{\omega} \quad (2.7)$$

The calculated PUL RLGC parameters for the three cases of the simulated winding structures are shown in Fig. 2-7. Since L_{PUL} has a positive or a negative real number, its polarity is also shown in the figure.
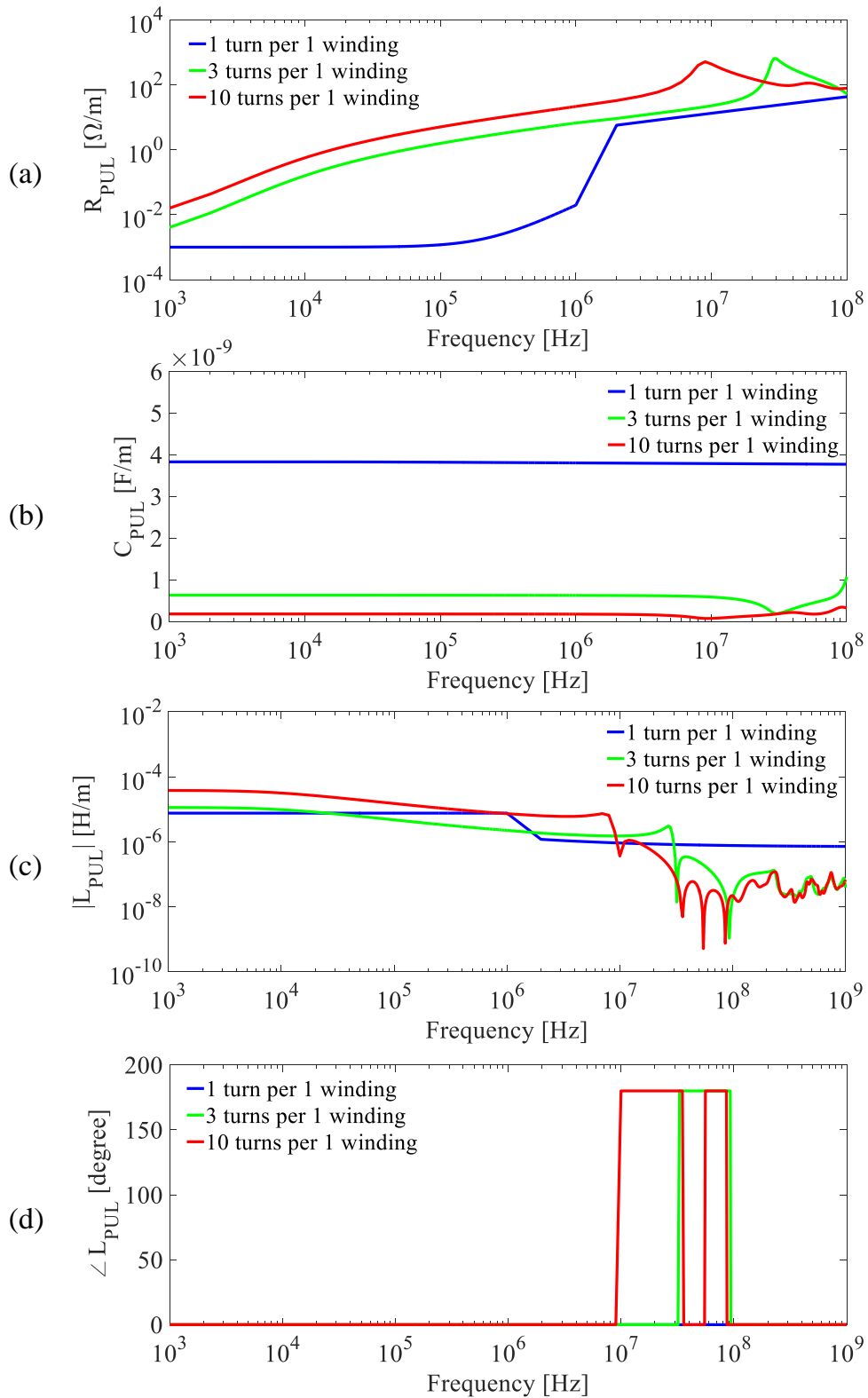
Fig. 2-7. The calculated PUL parameters for the simulated structures. (a) R_{PUL}. (b) C_{PUL}. (c) The magnitude of L_{PUL}. (d) The phase of L_{PUL}.

2.3. Construction of the PUL Equivalent Circuit Model

In this section, a modeling method of the PUL equivalent circuit which includes the high-frequency characteristics of the ac motor is proposed by using the calculated PUL RLGC parameters in the previous section. Fig. 2-8 shows the constructed PUL equivalent circuit model, and the method of defining the circuit elements in the model are discussed in the following subsections.
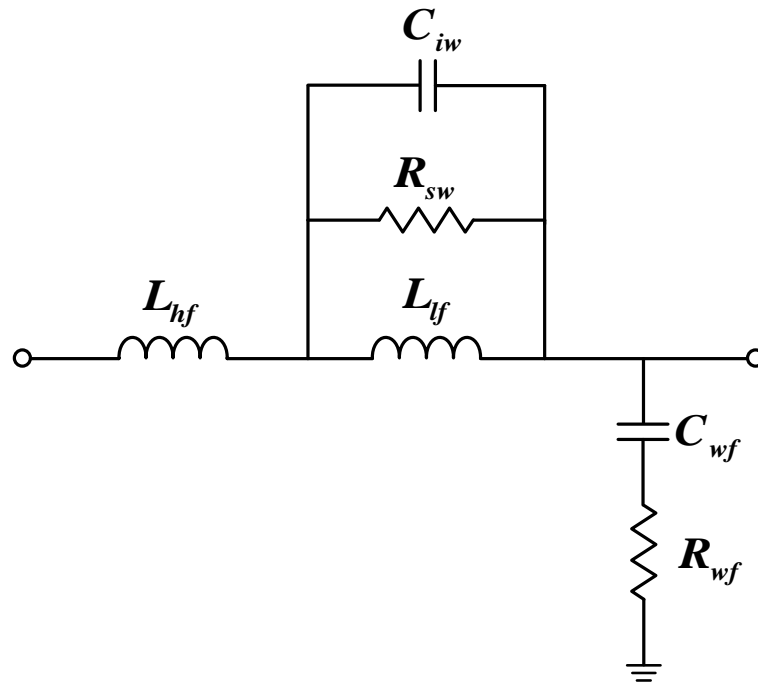
Fig. 2-8. The proposed PUL equivalent circuit for the motor winding structure.

2.3.1. Stator Winding Resistance

R_{sw} represents the resistive component that includes skin effect and eddy current losses in the conductor windings. Usually, it is difficult to define those resistances by analytical calculation. Instead, the value of R_{sw} can be obtained simply by choosing the peak value of R_{PUL} in Fig. 2-7. Since R_{sw} is involved in the parallel RLC circuit in the proposed equivalent circuit model as shown in Fig. 2-8, the peak value of R_{PUL} observed at the resonance can represent the lumped component R_{sw} in the equivalent circuit. In other frequency range, R_{PUL} follows the real value of $j\omega + \left(\frac{1}{j\omega C_{iw}} \parallel R_{sw} \parallel j\omega L_{lf} \right)$.

2.3.2. Winding-to-Frame Capacitance and Resistance

As shown in Fig. 2-6 (b), C_{PUL} is almost constant over the tested frequency area in all the simulated cases. Therefore, the value of C_{wf} in the PUL equivalent circuit model can be chosen simply as the constant value of C_{PUL}.

R_{wf} represents the resistive loss over the winding-to-frame insulators and the frame itself. This element can be observed when the first anti-resonance occurs in the high-frequency region. Therefore, it can be determined as following equation by using the calculated PUL *RLGC* values.

$$R_{wf} = \left| R_{PUL} + j\omega L_{PUL} + \frac{1}{G_{PUL} + j\omega C_{PUL}} \right|_{\omega=\omega_{antiresonance}} \tag{2.8}$$

2.3.3. Interwinding Capacitance

Interwinding capacitance C_{iw} is one of the most important parameters for the high-frequency analysis for the ac motor because it captures significant capacitive coupling between the conductors in both of slot and end-winding structure. C_{iw} causes the effective PUL inductance to be negative at ~10 MHz, where the magnitude of L_{PUL} decreases steeply and its phase is reversed, as shown in Fig. 2-7 (c) and (d). In the higher frequencies, L_{PUL} becomes a small value, because C_{iw} shorts out the low-frequency inductance L_{lf} in the proposed equivalent model.

To investigate the effect of C_{iw}, the winding inductance $L_{winding}$ can calculated analytically without considering C_{iw}. For example, a three-turn winding without interwinding capacitances can be simplified as shown in Fig. 2-9 (a). Then the value of $L_{winding}$ can be computed analytically from following formula:

$$\begin{bmatrix} V_1 \\ V_2 \\ V_3 \\ V_4 \\ V_5 \\ V_6 \end{bmatrix} = \begin{bmatrix} L_1 & M_{12} & M_{13} & & & \\ M_{12} & L_2 & M_{23} & & 0 & \\ M_{13} & M_{23} & L_3 & & & \\ & & & L_4 & M_{45} & M_{46} \\ & 0 & & M_{45} & L_5 & M_{56} \\ & & & M_{46} & M_{56} & L_6 \end{bmatrix} \begin{bmatrix} I_1 \\ I_2 \\ I_3 \\ -I_4 \\ -I_5 \\ -I_6 \end{bmatrix} \tag{2.9}$$
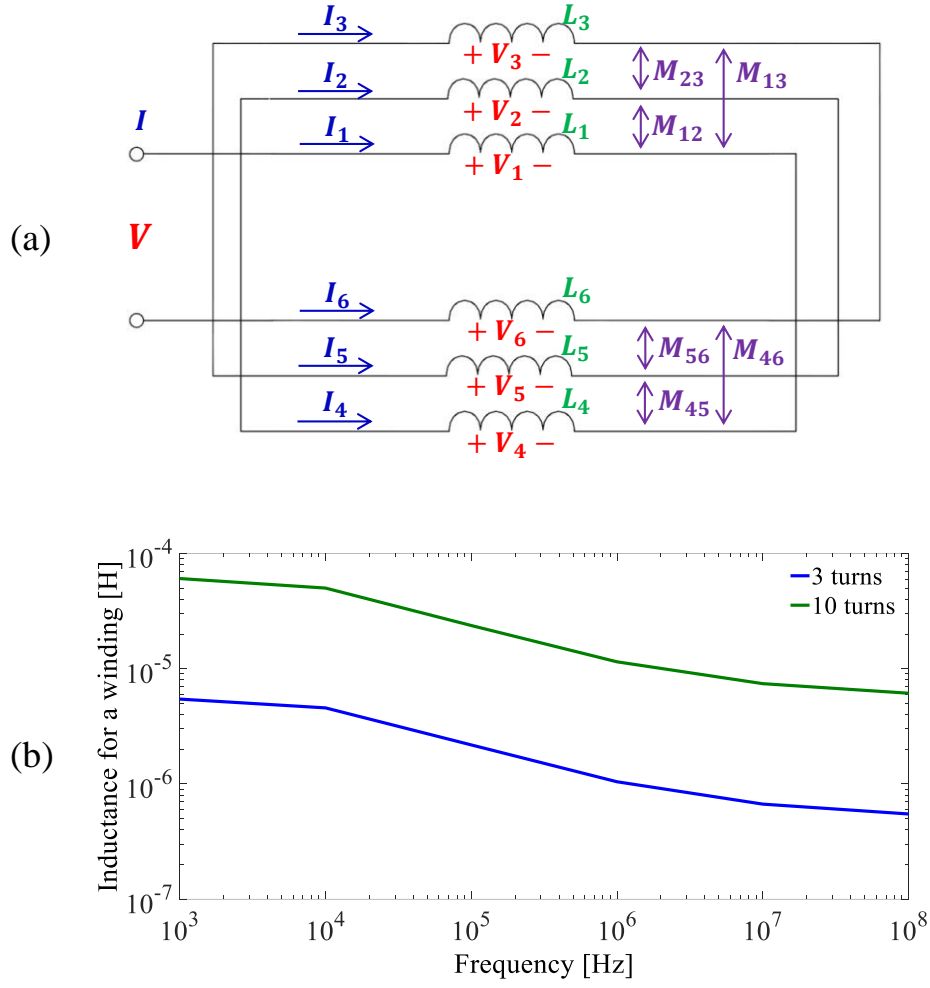
Fig. 2-9. (a) The circuit to calculate winding inductance (L_{3turns}) for three-turn winding. (b) The calculated winding inductances for three- and ten-turns.

From the symmetrical structure of the coil in Fig. 2-9 (a), the winding inductance can be calculated a following condition:

$$
\begin{aligned}
V &= V_1 - V_4 + V_2 - V_5 + V_3 - V_6 \\
I &= I_1 = I_2 = I_3 = -I_4 = -I_5 = -I_6 \\
L_1 &= L_4, \quad L_2 = L_5, \quad L_3 = L_6 \\
M_{12} &= M_{45}, \quad M_{23} = M_{56}, \quad M_{13} = M_{46}
\end{aligned}
\tag{2.10}
$$

$$
V = \left\{
\begin{array}{l}
(L_1 + M_{12} + M_{13})I + (L_2 + M_{12} + M_{23})I + (L_3 + M_{13} + M_{23})I \\
-(L_4 + M_{45} + M_{46})(-I) - (L_5 + M_{45} + M_{56})(-I) - (L_6 + M_{56} + M_{46})(-I)
\end{array}
\right\} j\omega \tag{2.11}
$$

The analytically calculated inductance for the three turns of the winding structure without the effect of C_{iw} can be extracted by following equation,

$$L_{3turns} = 2(L_1 + L_2 + L_3) + 4(M_{12} + M_{23} + M_{13}) \qquad (2.12)$$

The inductance of the ten turns of the winding structure also can be calculated in same method as follow:

$$L_{10turns} = 2(L_1 + L_2 + L_3 + \cdots + L_{10}) + 4(M_{12} + M_{13} + M_{14} + \cdots + M_{23} + \cdots + M_{34} + \cdots + M_{910}) \quad (2.13)$$

The results of the analytically calculated inductances for the three turns and ten turns winding structures are shown in Fig. 2-9 (b). Comparing Fig. 2-7 (c) with Fig. 2-9 (b), the effect of C_{iw} can be explained clearly. In the low frequency region, the value of L_{PUL} is exactly same with analytically calculated $L_{winding}$. However, it does not follow the trace of $L_{winding}$ any more in high-frequency region because of the effect of C_{iw}.

The value of C_{iw} can be obtained by the relating the response of L_{PUL} to the inductance of the series branch in the equivalent circuit model of Fig. 2-8 as follows:

$$L_{\mathrm{PUL}} = L_{hf} + \frac{R_{sw}L_{lf}}{R_{sw} + j\omega L_{lf} - \omega^2 R_{sw}L_{lf}C_{iw}} \qquad (2.14)$$

where C_{iw} should be found in the frequency range, which L_{PUL} is negative as shown in the result of Fig. 2-7 (d) because C_{iw} component becomes close to open or short circuit in the other frequency regions.

2.3.4. Stator Winding Inductance

L_{lf} and L_{hf} in the PUL equivalent circuit model represent winding inductances for low-frequency and high-frequency regions, respectively. L_{lf} can be determined as the almost constant value of the PUL inductance in the low-frequency region, where the effect of C_{iw} does not appear. The value of L_{hf} is defined as the converged value after C_{iw} is close to a short circuit component in the high-frequency resign as shown in the response of L_{PUL}.

2.3.5. The Input Impedance of the PUL Equivalent Circuit Model

Fig. 2-10 compares PUL input impedances $Z_{in,PUL}$ of the simulated winding structures by the PUL *RLGC* model in Fig. 2-2 (b) and the proposed equivalent circuit model in Fig. 2-8 respectively. As shown in the results, the proposed equivalent circuit models are in good agreements with the PUL *RLGC* model. Therefore, we can confirm that the estimated high-frequency parameters in the proposed

equivalent circuit can be applied for modeling the stator winding structure of the ac motors.
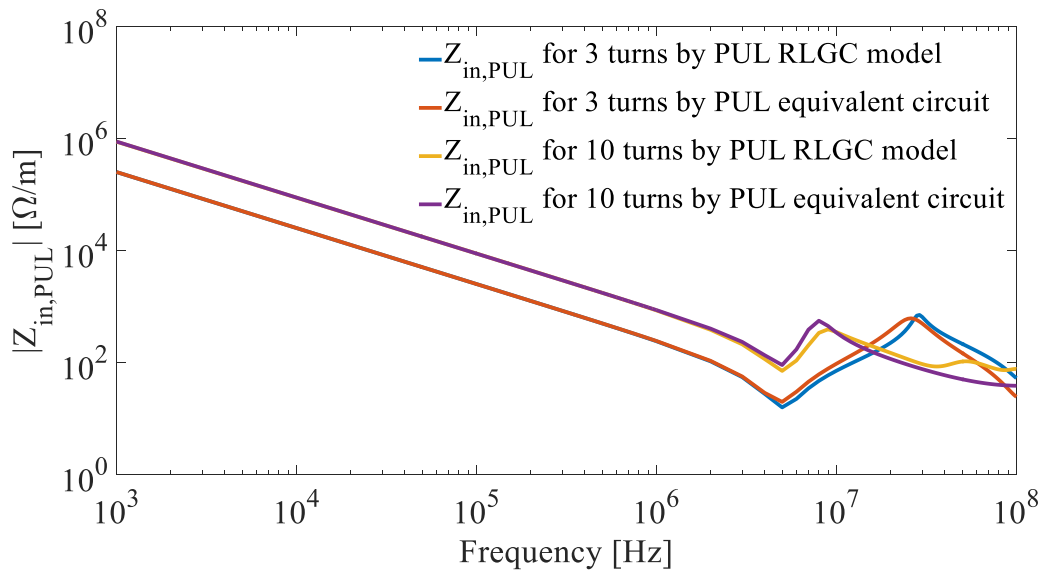
Fig. 2-10. The comparison of $Z_{in,PUL}$ between simulated structures and constructed equivalent circuits.

2.3.6. Verification of the Modeling Method of the PUL Equivalent Circuit by Measurement

To validate the equivalent circuit modeling method that described in the previous sections, the stator winding of a 200 W induction motor was characterized. In the tested motor, the number of turns for a winding is 92, and each phase winding has four coils. The total length of the phase winding is almost 95m. The measurement setup was established to characterize each phase line as two-port network using a network analyzer (Agilent E5061B) as shown in Fig. 2-11.
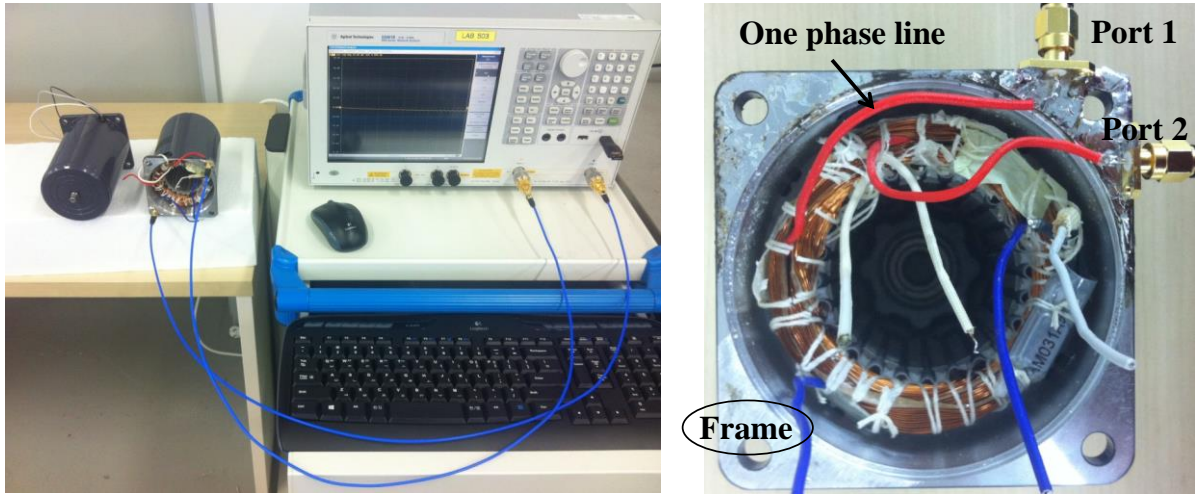
Fig. 2-11. The measurement setup to extract the S-parameters for the phase line of an 200W induction motor by the network analyzer.

By applying the proposed extraction method of the transmission line parameter, the PUL parameters of the measured induction motor is shown in Fig. 2-12. The captured values of R_{sw}, L_{lf}, L_{hf} and C_{wf}, for the PUL equivalent circuit model are indicated in the result graphs. The values of R_{wf} and C_{iw} can be calculated by (2.8) and (2.14) respectively. As can be expected from (2.14), the magnitude of L_{PUL} should decrease with the slope of $1/\omega^2$ in the frequency region, where the effect of C_{iw} appears. In the extracted result of Fig. 2-11 (c), the frequency range of the decreasing slope is clearly shown around from 100 kHz to 10 MHz.
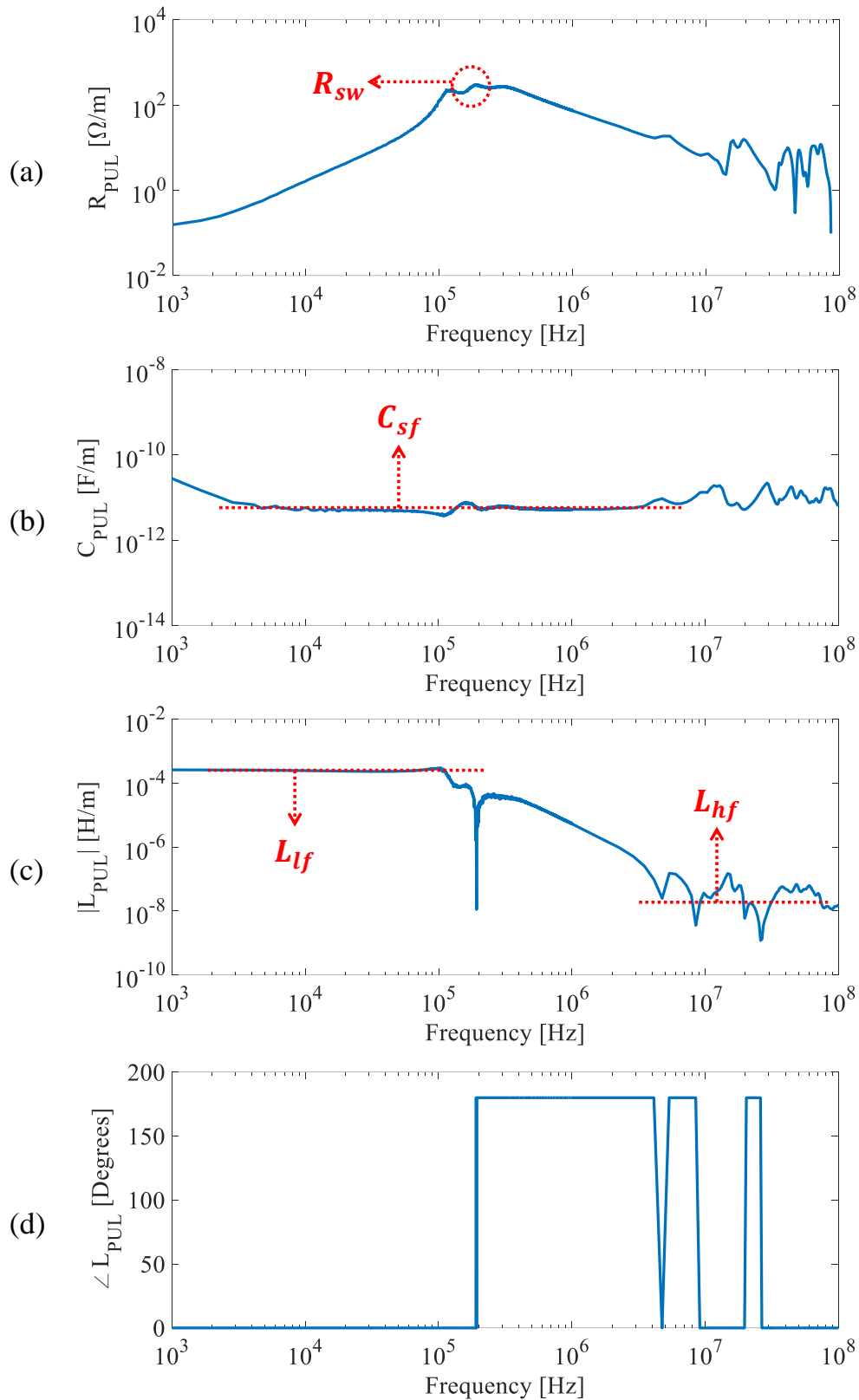
Fig. 2-12. Calculated PUL parameters for the measured AC machine. (a) R_{PUL}. (b) C_{PUL}. (c) Magnitude of L_{PUL}. (d) Phase of L_{PUL}.

27

Equivalent model of an infinitesimal section
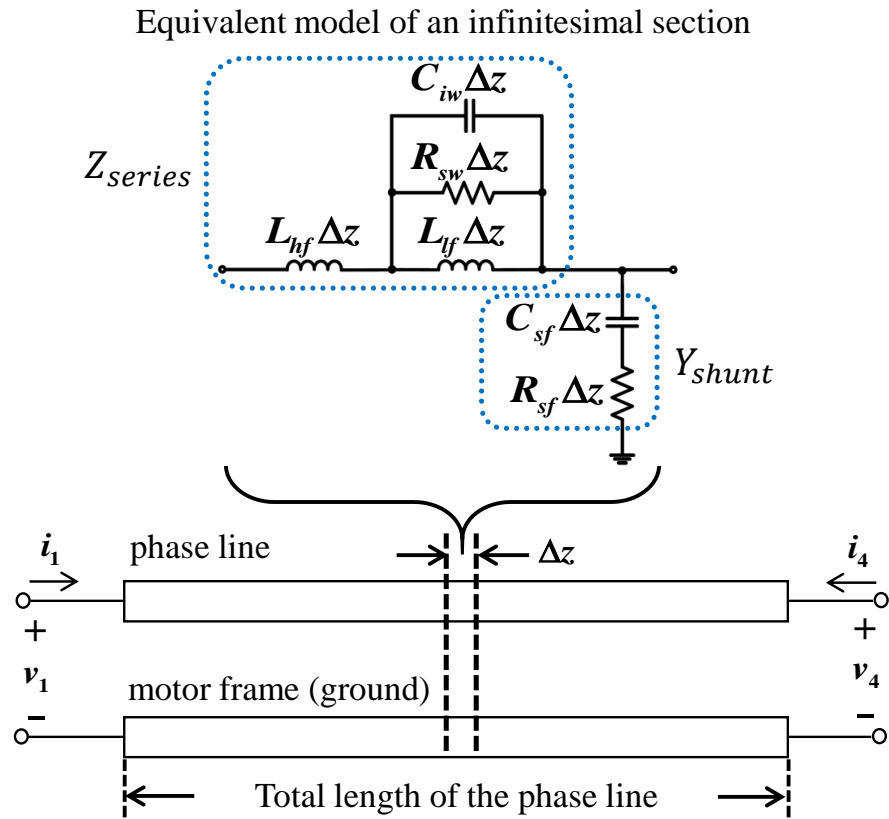
Fig. 2-13. The concept to extract the characteristic of the input impedance for the total length of the phase line by applying the constructed PUL equivalent circuit model.
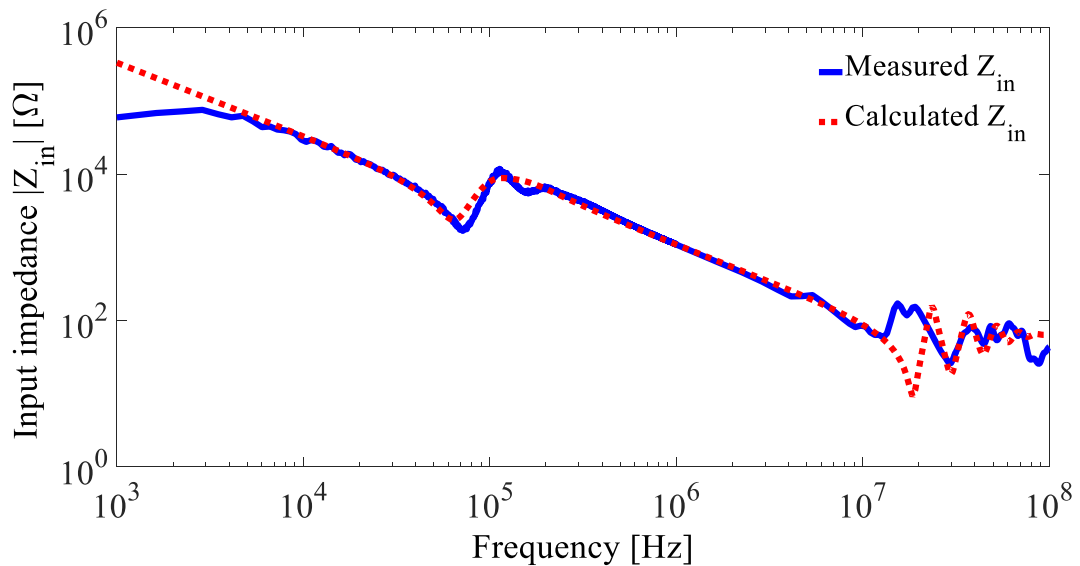
Fig. 2-14. Comparison between measured and calculated input impedance for the tested induction motor.

After the PUL equivalent circuit is constructed by the defined components, the characteristic of the input impedance Z_{in} for the total length of the phase line can be extracted. As shown in Fig. 2-13, we can obtain the distributed-element model of the phase winding by inserting PUL series impedance (Z) and shunt admittance (Y) into the following formulas for the conversion of the *ABCD* parameters of general transmission lines:

$$
\begin{bmatrix} A & B \\ C & D \end{bmatrix} = \begin{bmatrix} \cosh\left(l\sqrt{Z_{series}Y_{shunt}}\right) & \sqrt{\dfrac{Z_{series}}{Y_{shunt}}}\sinh\left(l\sqrt{Z_{series}Y_{shunt}}\right) \\ \sqrt{\dfrac{Y_{shunt}}{Z_{series}}}\sinh\left(l\sqrt{Z_{series}Y_{shunt}}\right) & \cosh\left(l\sqrt{Z_{series}Y_{shunt}}\right) \end{bmatrix} \tag{2.15}
$$

$$
\begin{bmatrix} Z_{11} & Z_{12} \\ Z_{21} & Z_{22} \end{bmatrix} = \begin{bmatrix} \dfrac{A}{C} & \dfrac{AD-BC}{C} \\ \dfrac{1}{C} & \dfrac{D}{C} \end{bmatrix} \tag{2.16}
$$

$$
Z_{in} = Z_{11} = \frac{A}{C} = \sqrt{\frac{Z_{series}}{Y_{shunt}}}\coth\left(l\sqrt{Z_{series}Y_{shunt}}\right) \tag{2.17}
$$

where the value l is the total length of the phase line. The input impedance Z_{in} for the phase line is the impedance seen from one terminal of the transmission line with the other terminal opened. The results of the measured and the calculated input impedances for the phase line with the total length are shown in Fig. 2-14. As shown in the results, the calculated result by using the constructed PUL equivalent circuit model shows a close match with the measured input impedance. By using the proposed method, a simple PUL lumped-element circuit can be obtained instead of using many complex lumped components for the equivalent circuit. In addition, it can be used to predict the high-frequency parameters during an initial motor design process by simulation data.

2.3.7. Characteristic of the Winding-to-Frame Capacitance for the High-Power AC Motor

In the proposed PUL equivalent circuit model of the previous section, the stator-to-frame capacitance element is defined from the constant value of the extracted PUL capacitance. However, the previous equivalent circuit model is difficult to apply for the high-power motor because the stator-to-frame capacitance does not have a constant value [33]. In the high-power motor, the stator-to-frame

capacitance decreases in several stages in the frequency range of interest. Therefore, the previous equivalent circuit model should be modified to include this characteristic for the high-power motors.
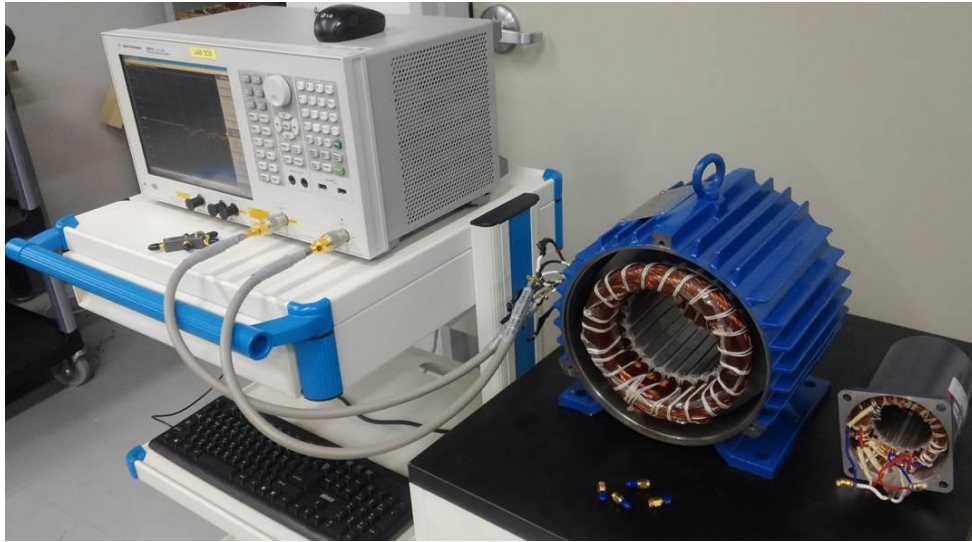
Fig. 2-15. Measurement to extract the S-parameters for the stator winding structure of high-power ac motor1 by a network analyzer.
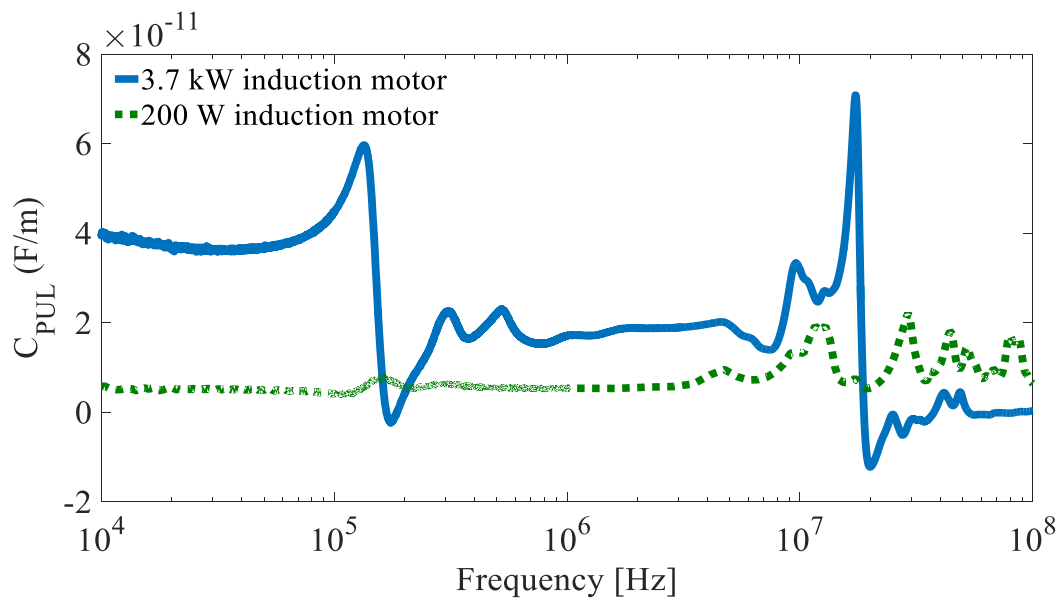
Fig. 2-16. The extracted characteristics of the PUL capacitances for 200 W and 3.7 kW induction motors.

To investigate the variation of stator-to-frame capacitance, measurement is implemented for low and high-power motor as shown in Fig. 2-15. The results of the extracted PUL capacitances for 200 W and 3.7 kW induction motors are compared in Fig. 2-16. In the result, the extracted PUL capacitance of 200 W motor has almost constant value throughout the measured frequency. However, the PUL capacitance has different stable states before and after the resonance frequencies in 3.7 kW motor. Therefore, the shunt admittance model of the PUL equivalent model in Fig. 2-8 cannot capture this phenomenon because it can consider only single stage stable value of PUL capacitance. Consequently, the stator-to-frame elements of the PUL equivalent model should be modified to include this phenomenon.

2.3.8. Winding-to-Frame Admittance Model by Debye Modeling Method

To consider the changes of the stator-to-frame capacitance in the high-power motor, the shunt admittance can be modeled by applying the Debye model [34]. The general admittance model is defined as follows:

$$Y = G + j\omega C \tag{2.18}$$

$$\frac{Y}{j\omega} = C - j\frac{G}{\omega} \tag{2.19}$$

By modifying the Debye model to the admittance expression, the change of capacitance can be expressed by following formula:

$$Y_{DEBYE} = C_\infty + \sum_{i=1}^{K} \frac{\Delta C_i}{1 + j\dfrac{\omega}{\omega_i}} \tag{2.20}$$

where, ΔC_i represents the difference between the stable capacitances before and after the resonance frequencies. ω_i is the angular frequency at the resonance. In the high frequencies, the real part of the Y_{DEBYE} approaches C_∞. The capacitance and conductance can be obtained by the relation between (2.19) and (2.20) as follows:

$$C = \Re(Y_{DEBYE}) \tag{2.21}$$

$$G = -\Im(Y_{DEBYE})\omega \tag{2.22}$$

To improve the admittance model of the equivalent circuit, the extracted PUL capacitance of the

tested 3.7 kW induction motor is analyzed as shown in Fig. 2-17. The admittance parameters can be calculated by applying (2.20) with the indicated parameters in the figure as follows:

$$C_3 + \frac{C_A}{1+j\omega\tau_a} + \frac{C_B}{1+j\omega\tau_b} \tag{2.23}$$
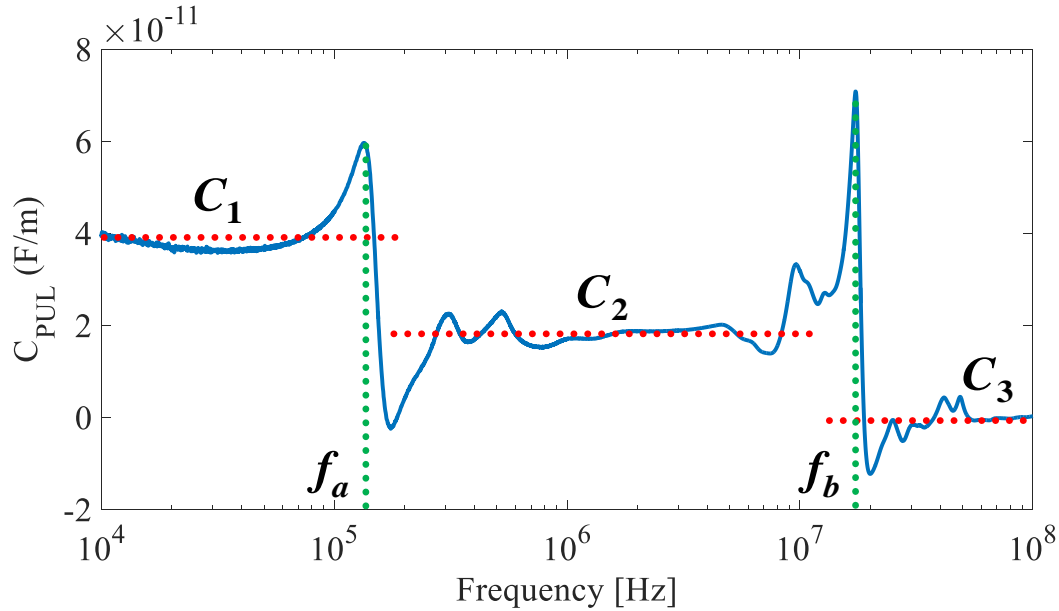
Fig. 2-17. The analysis of the PUL capacitance to define equivalent circuit parameters.

where, the values of C_A, C_B, τ_a and τ_b are defined as follows:

$$C_A = C_1 - C_2, \quad C_B = C_2 - C_3, \quad \tau_a = \frac{1}{2\pi f_a}, \quad \tau_b = \frac{1}{2\pi f_b} \tag{2.24}$$

An admittance model with the lumped elements can be constructed as shown in Fig. 2-18. Through the conversion of the admittance and impedance expression, the elements of equivalent model can be defined simply. For example, if we define that the second level of admittance model which consists of C_b and R_b is Y_b, then the impedance is,

$$Y_b = \frac{j\omega C_A}{1+j\omega\tau_a} \quad \Rightarrow \quad Z_b = \frac{1}{j\omega C_A} + \frac{\tau_a}{C_A} \tag{2.25}$$

Finally, from the observation of the impedance expression, the values of the lumped elements in the admittance model of Fig. 2-18 can be obtained as follows:

$$C_a = C_3, \quad C_b = C_A, \quad C_c = C_B, \quad R_b = \frac{\tau_a}{C_A}, \quad R_c = \frac{\tau_b}{C_B} \tag{2.26}$$
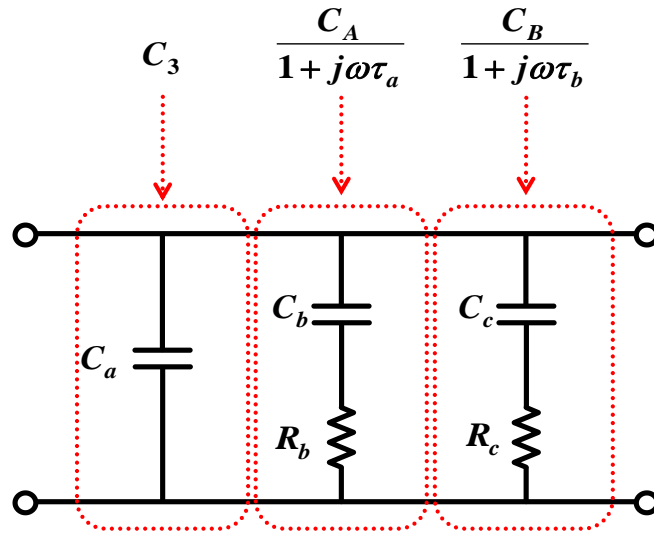
Fig. 2-18. The admittance model of the stator winding structure of the ac motor by using the modified Debye model.

The capacitance and conductance of the equivalent admittance model are compared with the extracted PUL parameters in Fig. 2-19. Even though the modeled capacitance does not capture the peaks at the resonances, it follows the trend of the change of PUL capacitance throughout the observed frequency region. In addition, the modeled conductance follows the increasing PUL conductance reasonably.
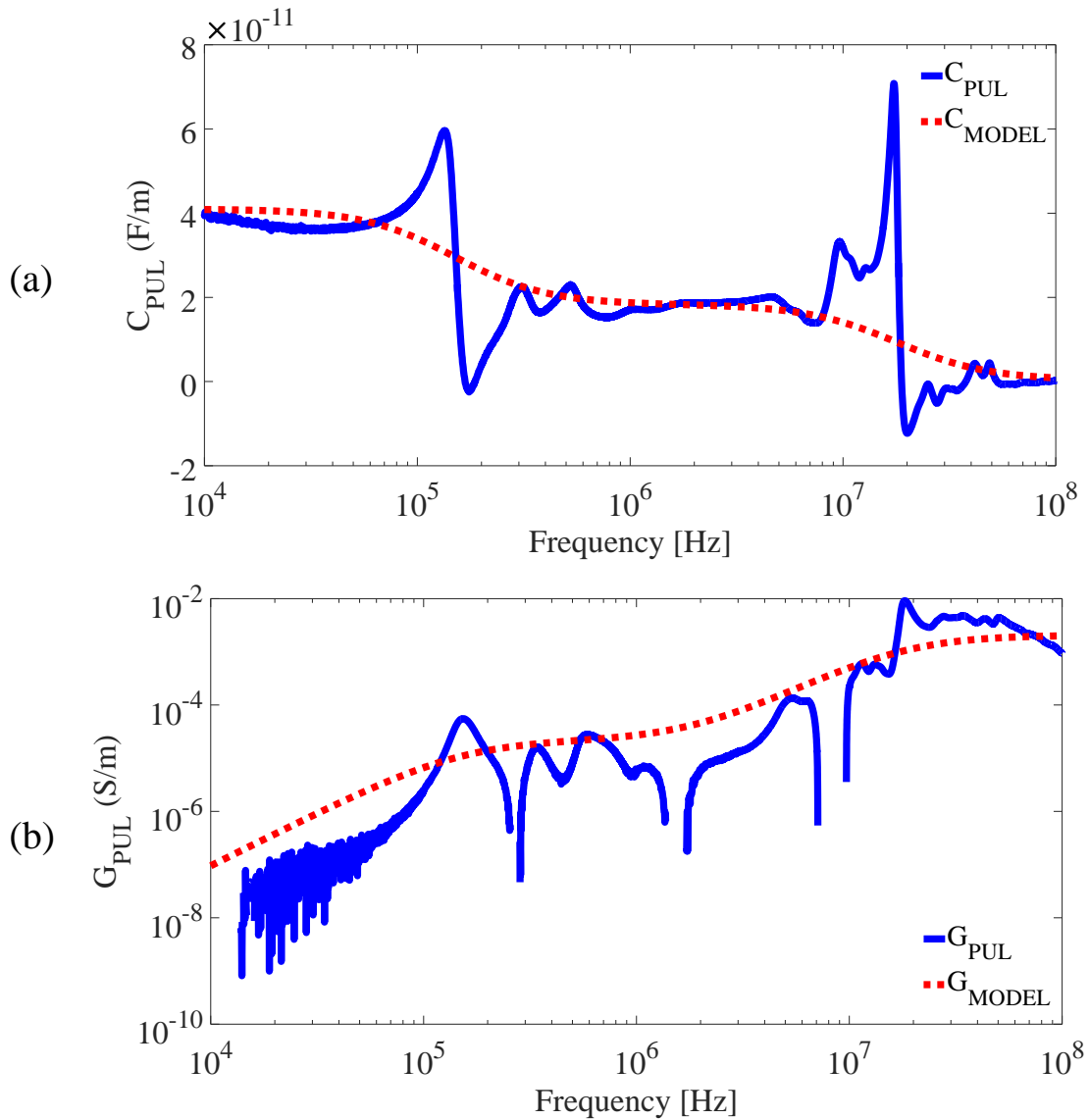
Fig. 2-19. Comparison of the extracted PUL parameter and the constructed admittance model. (a) The PUL capacitance. (b) The PUL conductance.

By including the shunt admittance model of Fig. 2-18, the improved PUL equivalent model is proposed in Fig. 2-20. $C_{wf\text{-}hf}$ represents the winding-to-frame PUL capacitance at the high-frequency region. The second and third level admittances are defined as the elements $C_{wf\text{-}n}$ and $R_{wf\text{-}n}$ in the model, where n is the order of the stable state of the PUL capacitance. If the extracted PUL capacitance has more different stages in the other motors, additional shunt admittance elements can be applied in the proposed model.
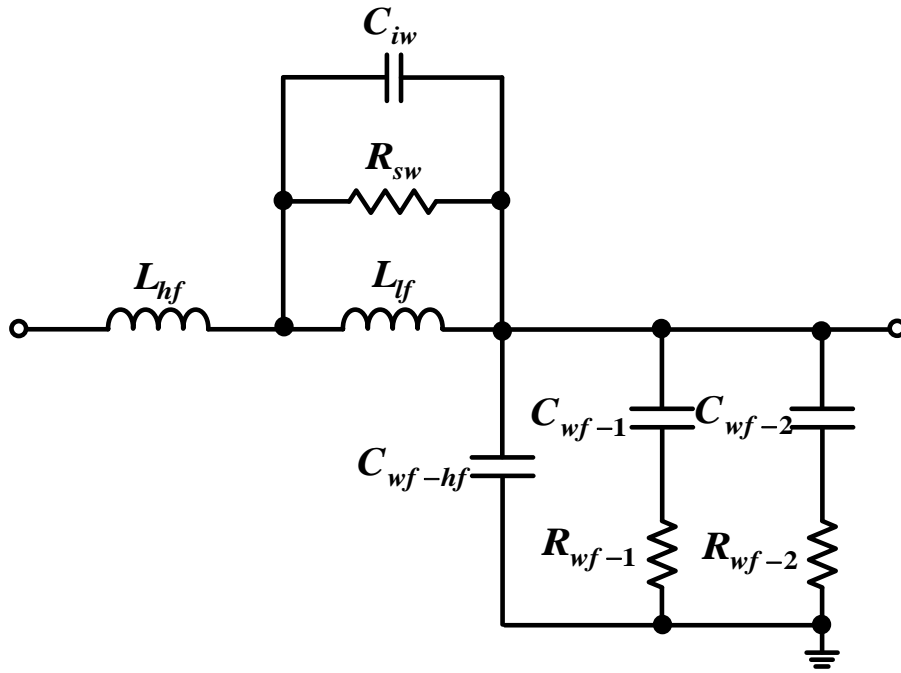
Fig. 2-20. The PUL equivalent circuit model considering the change of PUL capacitance.

By using the newly developed PUL equivalent model, the input and transfer impedances for the total length of a phase line can be obtained as following equations:

$$Z_{in} = \sqrt{\frac{Z_{series}}{Y_{shunt}}} \coth\left(l\sqrt{Z_{series}Y_{shunt}}\right), \quad Z_{tr} = \sqrt{\frac{Z_{series}}{Y_{shunt}}} \operatorname{csch}\left(l\sqrt{Z_{series}Y_{shunt}}\right) \tag{2.27}$$

The comparison of the measured and modeled impedances for the entire phase line is shown in Fig. 2-21. Differences between the model and the measurement around resonant frequencies occur because the over-damped Debye model cannot capture resonant peaks. However, the proposed equivalent model estimates reasonably the input and the transfer impedance characteristics of stator winding structure over a wide frequency range.
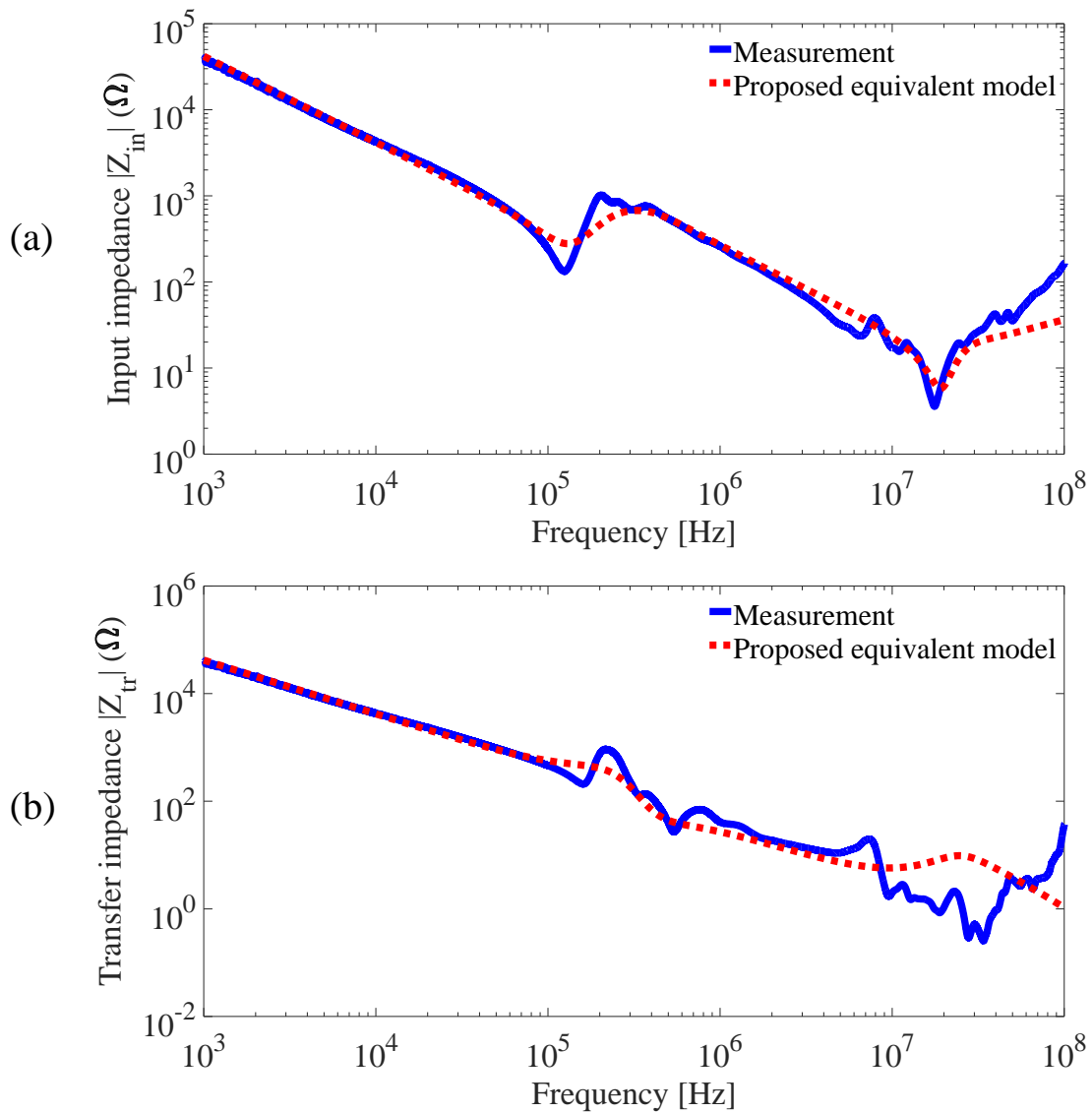
Fig. 2-21. Comparison of the impedances for the phase line between the measurement and the proposed equivalent model. (a) The input impedance. (b) The transfer impedance.

The developed PUL equivalent model including the modified stator-to-fame admittance model can be used for any power type of ac motor with improved accuracy to characterize the high-frequency parameters.

2.3.9. The Improved PUL Equivalent Circuit Model with Lorentz Modeling Method

In this section, the final improved PUL equivalent circuit model is proposed. To construct the PUL admittance model precisely, Lorentz model is applied [35-36], which develops previous Debye admittance model. Moreover, the resistance of the insulation sheet is modeled in the improved admittance model by analysis of the PUL conductance. In addition, the series PUL impedance model is enhanced by including the skin effect of the winding conductors.

Through investigation of the PUL parameters which are extracted from the measured network parameters of the ac motor in Fig. 2-15, the final improved PUL equivalent circuit model is constructed as shown in Fig. 2-22. The comparison of the PUL parameters between the transmission line extraction, the previous equivalent circuit model of Fig. 2-20 and the proposed equivalent circuit model of Fig. 2-22 is shown in Fig. 2-24. In addition, Fig. 2-23 shows which elements of the proposed equivalent circuit model are extracted from which PUL parameters respectively, and the found values of the elements in the equivalent circuit model are given in Table 2-1.
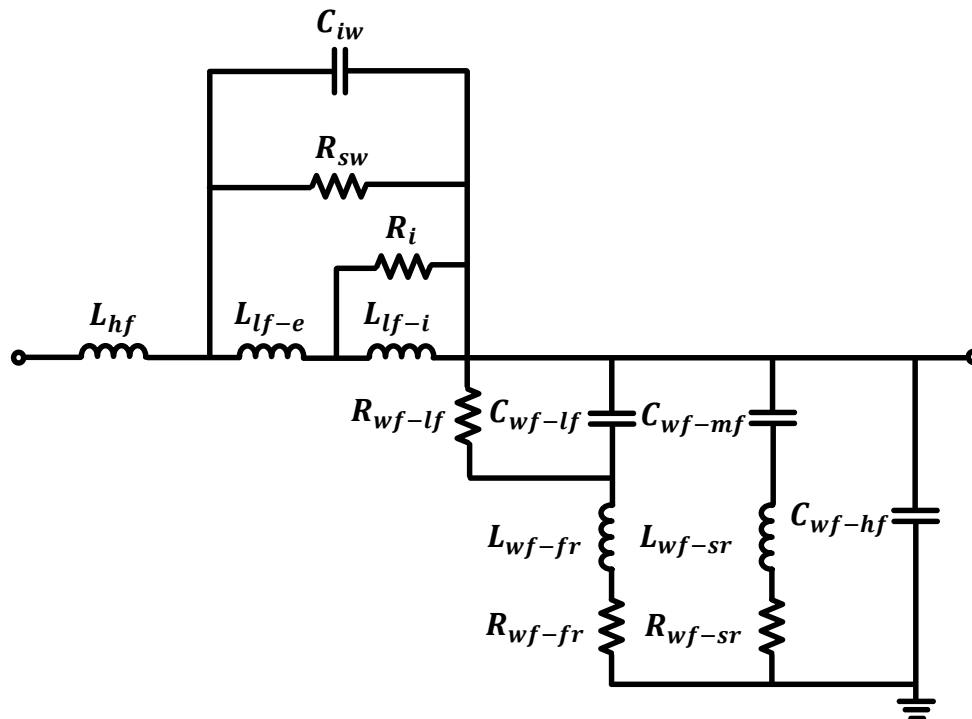
Fig. 2-22. The final Improved PUL equivalent circuit model for the ac motor.
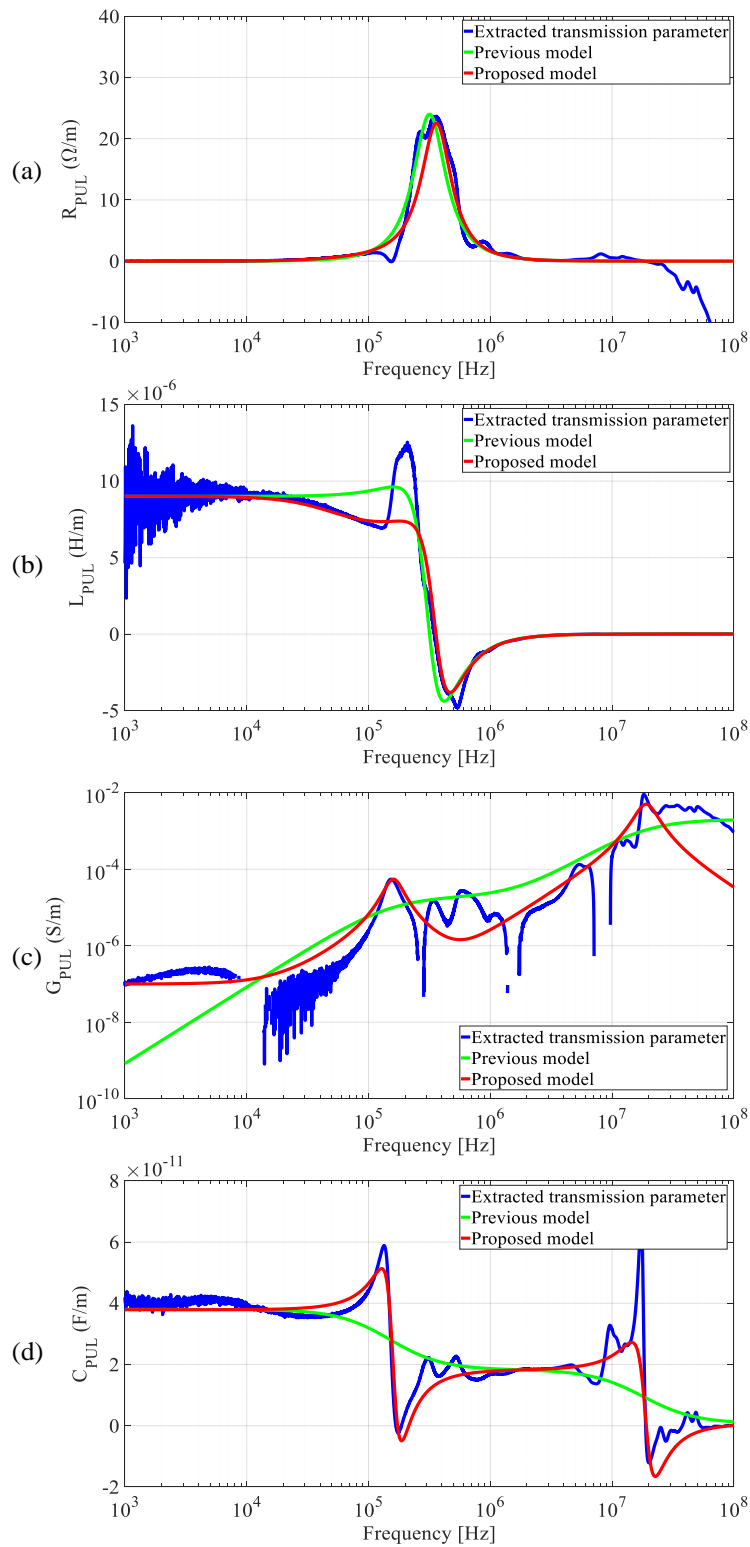
Fig. 2-23. Comparison of the PUL RLGC parameters between transmission line parameters, the previous equivalent circuit model of 2-20, and the final proposed equivalent circuit model of Fig. 2-22. (a) PUL resistance. (b) PUL inductance. (c) PUL conductance. (d) PUL capacitance.

Extracted PUL parameters

The elements of the proposed equivalent circuit model
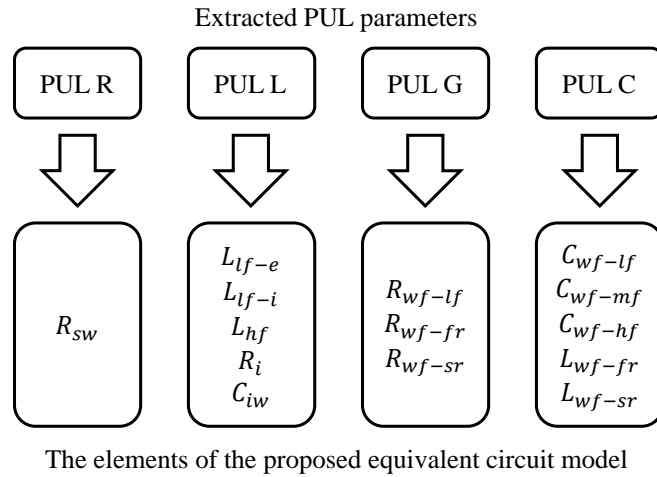
Fig. 2-24. The modeling process to define the elements of the final proposed equivalent circuit model from the extracted PUL *RLGC*.

Table 2-1. Values of the elements in the improved PUL equivalent circuit model

The elements of PUL equivalent circuit model	Values
R_{sw}: Stator-winding resistance	24 Ω/m
R_i: Internal resistance	0.7 Ω/m
$L_{lf\text{-}e}$: Low-frequency external inductance	7 μH/m
$L_{lf\text{-}i}$: Low-frequency internal inductance	2 μH/m
L_{hf}: High-frequency inductance	4 μH/m
C_{iw}: Inter-winding capacitance	28 nF/m
$R_{wf\text{-}lf}$: Low-frequency winding-to-frame resistance	10 MΩ/m
$R_{wf\text{-}fr}$: First-resonance winding-to-frame resistance	18 kΩ/m
$R_{wf\text{-}sr}$: Second-resonance winding-to-frame resistance	200 Ω/m
$L_{wf\text{-}fr}$: First-resonance winding-to-frame inductance	50 mH/m
$L_{wf\text{-}sr}$: Second-resonance winding-to-frame inductance	4 μH/m
$C_{wf\text{-}lf}$: Low-frequency winding-to-frame capacitance	20 pF/m
$C_{wf\text{-}mf}$: Mid-frequency winding-to-frame capacitance	17.5 pF/m
$C_{wf\text{-}hf}$: High-frauency winding-to-frame capacitance	0.75 pF/m

The detailed definitions of the elements in the final improved PUL equivalent circuit model are described by analysis of the frequency-response of the PUL parameters as follows. In the series impedance of the proposed equivalent circuit model, there are six elements. Since the stator-winding resistance (R_{sw}) is in the parallel RLC resonant tank, its value can be captured simply from the peak value of the extracted PUL resistance at the resonance in Fig. 2-23 (a).

The low-frequency internal inductance (L_{lf-i}), low-frequency external inductance (L_{lf-e}) and internal resistance (R_i) describe the changing PUL inductance characteristic of the winding conductors by the skin effect. In 1 kHz to 10 kHz frequency region of Fig. 2-23 (b), both of inductances, L_{lf-i} and L_{lf-e}, are effective. After 10 kHz, the skin effect occurs prominently in the winding conductors, and it is considered as a parallel circuit of L_{lf-i} and R_i in the equivalent circuit model. Around 100 kHz, the effect of L_{lf-i} is almost disappears, then only L_{lf-e} represents as an effective inductance of the stator windings.

The inter-winding capacitance (C_{iw}) can be defined by the steeply decreasing PUL inductance from 300 kHz to 10 MHz, where C_{iw} causes the PUL inductance to be negative. In the high-frequency region from around 10 MHz, C_{iw} becomes almost short circuit, and only small value of the high-frequency inductance (L_{hf}), which can be defined from the converged value of the PUL inductance, represents as the phase line inductance at the high-frequency region.

The parallel admittance of the proposed equivalent circuit model is constructed by applying Lorentz model. The difference of the first and the second stable values of the PUL capacitance in Fig. 2-23 (d) defines the low-frequency winding-to-frame capacitance (C_{wf-lf}). Similarly, the mid-frequency winding-to-frame capacitance (C_{wf-mf}) represents the difference between the second and the third stages. The high-frequency winding-to-frame capacitance (C_{wf-hf}) is defined from the stable value of the PUL capacitance of around 100 MHz.

By putting an inductance in each admittance brunch, the resonant peaks of the PUL capacitance, which could not be considered in the previous model of Fig. 2-20, are captured clearly as shown in Fig. 2-23 (d). The first resonant peak of the PUL capacitance is modeled by the first-resonance winding-to-frame inductance (L_{wf-fr}) component. The investigated L_{wf-fr} has large value, therefore it can represent the magnetizing inductance of the stator core. The second-resonance winding-to-frame inductance (L_{wf-sr}) captures the second resonant peak of the PUL capacitance, and it describes the eddy currents effects of the laminated sheets in the stator core [37].

The winding-to-frame resistances (R_{wf-fr} and R_{wf-sr}) represent the impedances which can be observed at the resonances, and their values are obtained simply from the peak values of the PUL conductance at the resonances as shown in Fig. 2-23 (c).

The low-frequency winding-to-frame resistance (R_{wf-lf}) in the equivalent circuit model is defined by the almost constant value of the PUL conductance from 1 kHz to 10 kHz, and its large value represents

the resistance of the insulation sheet material from dc to low-frequency region.

The summarized definition to obtain the values of the elements in the constructed PUL equivalent circuit model is shown in Table 2-2. Consequentially, the real and imaginary parts of the series impedance and the shunt admittance in the proposed equivalent circuit model shows close match with the extracted PUL *RLGC* parameters as shown in the overall results of Fig. 2-23.

Table 2-2. Summary of the value definitions of the elements in the equivalent circuit model

Element	Definition of the values
R_{sw}	The peak value of R_{PUL}
R_i	The damping factor of L_{PUL} in the low-frequency region
$L_{lf\text{-}e}$	The constant value of L_{PUL} in the low-frequency region
$L_{lf\text{-}i}$	The value of L_{PUL} before C_{iw} effect appears
L_{hf}	The converged value of L_{PUL} in the high-frequency region
C_{iw}	The series impedance equation after other element values are found
$R_{wf\text{-}lf}$	The reciprocal number of the constant value of G_{PUL} in the low-frequency region
$R_{wf\text{-}fr}$	The reciprocal number of the peak value of G_{PUL} at the low-frequency resonance
$R_{wf\text{-}sr}$	The reciprocal number of the peak value of G_{PUL} at the high-frequency resonance
$L_{wf\text{-}fr}$	The shunt admittance equiation at the low-frequency resonance
$L_{wf\text{-}sr}$	The shunt admittance equiation at the high-frequency resonance
$C_{wf\text{-}lf}$	The difference of C_{PUL} between first and second constant values
$C_{wf\text{-}mf}$	The difference of C_{PUL} between second and third constant values
$C_{wf\text{-}hf}$	The converged value of C_{PUL} in the high-frequency region

2.3.10. Verification of the Final Improved PUL equivalent circuit model for the AC Motor
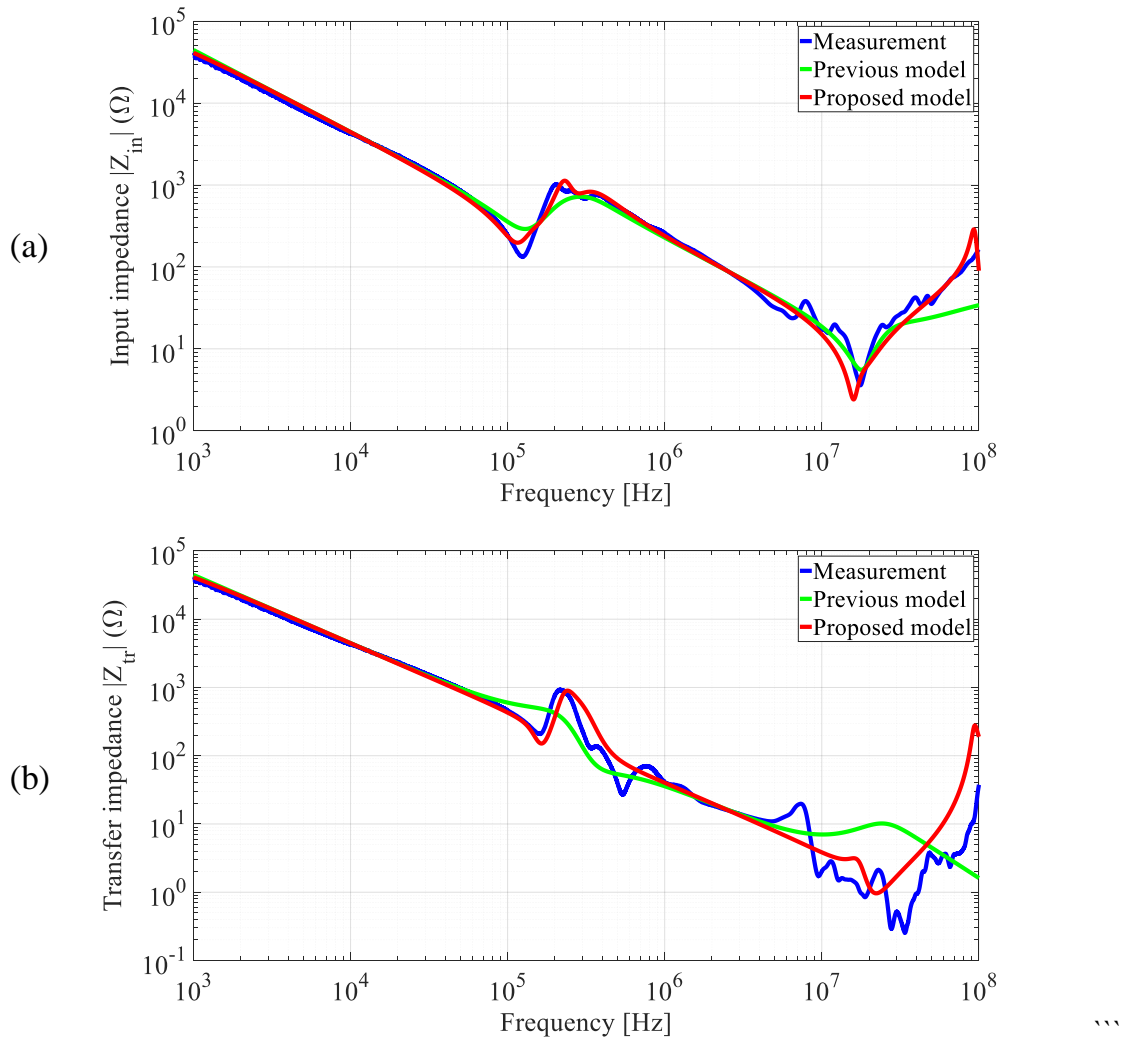
Fig. 2-25. (a) Comparison of the input impedances between the measurement and the equivalent circuit models for the total length of the phase line. (b) Comparison of the transfer impedances between the measurement and the equivalent circuit models for the total length of the phase line.

From the improved PUL equivalent circuit model, the input impedance and the transfer impedance for the entire length of the phase winding can be found by (27). The comparison of the input impedance and the transfer impedance between the measurement, the previous equivalent circuit model and the proposed final equivalent circuit model is shown in Fig 2-25. In the results, the developed equivalent

42

circuit model shows high accuracy with the measurement.

2.4. Summary

In this chapter, a PUL equivalent circuit modeling method for the ac motor was proposed to predict the high-frequency CE. The high-frequency elements in the PUL equivalent circuit model was extracted by using the transmission line model. Composed of the constant PUL elements, the proposed equivalent circuit model is simpler than the previous equivalent circuit models that include complex lumped components. Moreover, the PUL equivalent circuit model is improved to apply any type of the ac motor. The admittance model is developed to capture the frequency-dependent PUL capacitance by Debye and Lorentz model. Furthermore, the skin effect of the winding conductors, and the resistance of the insulation sheet are considered to include the wideband frequency behaviors. Consequently, using the proposed modeling method, the high-frequency characteristics of the ac motor winding structure can be estimated simply without any complicated calculations. In addition, the final improved equivalent circuit model shows high accuracy for the input and transfer impedances as compared with the previous model. Therefore, the proposed equivalent circuit modeling method and can be used to predict the wideband frequency characteristics for the universal ac motor in initial design stage.

Chapter III

Multi-Port Network Parameter Extraction of the Three-Phase Windings in the AC Motor using Mixed-Mode Network Matrix Conversion Method

3.1. Introduction

In this chapter, an extraction method of the multi-port network parameter for the three-phase windings structure of the ac motor is proposed. To estimate the EM couplings in the three-phase windings, the multi-port network parameter of the ac motor is extracted from the characterization of the mixed-mode network parameters. Under the assumption of the symmetry of the three-phase windings, the proposed method enables the creation of multi-port network parameter including the EM couplings, without a full six-port measurement setup. For verification, the calculated impedance is compared with the measured input impedance for the single-phase winding. In addition, the per-phase equivalent circuit model including the phase-to-phase coupling under the balanced excitation is proposed by the simple calculation with the extracted multi-port network parameters. The proposed equivalent model can distinguish the phase-to-phase coupling from the self-coupling in the phase winding. Therefore, the influence of the phase-to-phase coupling for the phase line can be investigated by comparing the input impedances of coupled and uncoupled models.

3.2. Investigation of the EM Coupling Effect in the Three-Phase Winding Structure

To observe the influence of all the EM parasitic couplings for the three-phase, the stator winding of a 3.7kW induction machine is measured with the different terminal conditions. The measured ac motor has a 2-pole, double layer winding in 24 slots, and each winding has 20 turns. The measurement setup was established to characterize each phase winding as a two-port network using the vector network analyzer. The measured S-parameters are converted to Z-parameters to obtain the input impedances, and they are extracted by 1GHz to capture the antiresonances clearly at the high-frequency region.

Two measured input impedances through for the phase line are compared in Fig. 3-1, where one is measured with the other terminals open and the other is measured with the other terminals connected to the reference impedance (50 ohm). The measurement with terminated reference impedance for other

terminals can extract the pure EM characteristic of the single phase line. On the other hand, the measurement result of the opened other terminals must include the EM coupling effect from the other phases even if it is small signal. As shown in Fig. 3-1, the input impedances of the single phase line are different up to mid-frequency region since the phase-to-phase coupling effect is altered by the terminal conditions. This result shows that the effect of phase-to-phase coupling should be considered for the accurate estimation of the frequency dependent behavior of the multi-phase structure of the ac machine.
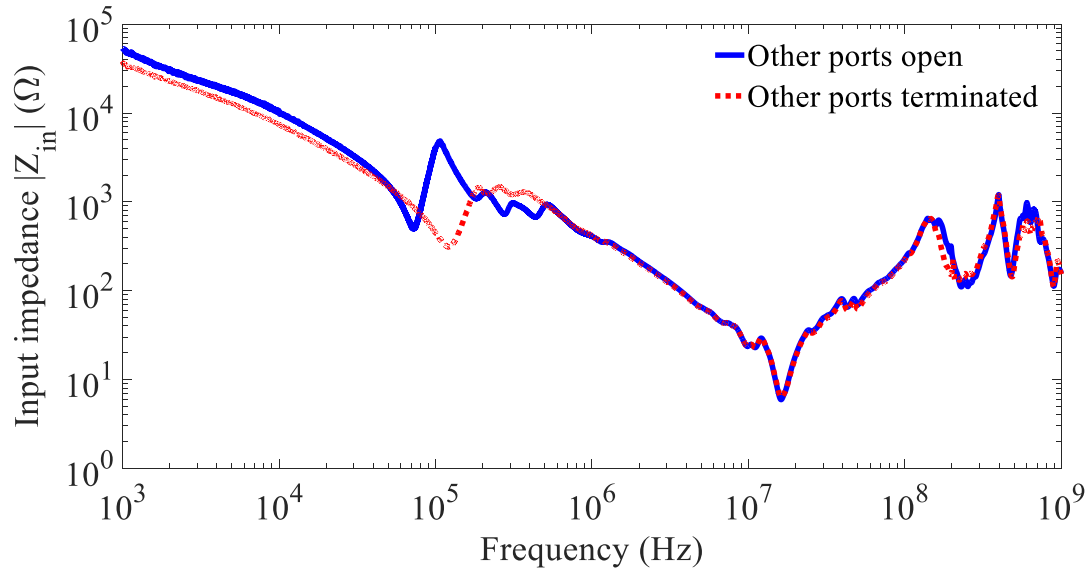
Fig. 3-1. Comparison of input impedances of the single phase line measured with open and terminated ports for other phase lines.

3.3. Network Parameter Extraction for the Three-Phase Phase Windings

3.3.1. Extraction of the Six-port Z-parameters for the Winding Structure

The relations of the voltages and currents for the six-port network of the three-phase windings are defined as shown in Fig. 3-2. The relations of the voltages and currents for the two-port network of the CM connection and DM connection of the three-phase windings are defined as shown in Fig. 3-3. The full six by six matrix of the impedance parameters for the multi-network of the three-phase winding structure can be defined as follow:

$$
\begin{bmatrix} v_1 \\ v_2 \\ v_3 \\ v_4 \\ v_5 \\ v_6 \end{bmatrix} = \begin{bmatrix} z_{11} & z_{12} & z_{13} & z_{14} & z_{15} & z_{16} \\ z_{21} & z_{22} & z_{23} & z_{24} & z_{25} & z_{26} \\ z_{31} & z_{32} & z_{33} & z_{34} & z_{35} & z_{36} \\ z_{41} & z_{42} & z_{43} & z_{44} & z_{45} & z_{46} \\ z_{51} & z_{52} & z_{53} & z_{54} & z_{55} & z_{56} \\ z_{61} & z_{62} & z_{63} & z_{64} & z_{65} & z_{66} \end{bmatrix} \begin{bmatrix} i_1 \\ i_2 \\ i_3 \\ i_4 \\ i_5 \\ i_6 \end{bmatrix}
\tag{3.1}
$$

where, each element in the impedance parameter matrix is defined as follow:

$$
z_{nm} = \left. \frac{v_n}{i_m} \right|_{i_k = 0(k \neq m)}
\tag{3.2}
$$

The ac machines having three-phase windings can be constructed by various methods according to the number of layers in a slot and coil pitch. However, (3.1) can be simplified for any type of windings as following equation because the three-phase winding structure is almost symmetric in the ac motor:

$$
\begin{bmatrix} v_1 \\ v_2 \\ v_3 \\ v_4 \\ v_5 \\ v_6 \end{bmatrix} = \begin{bmatrix} x & u & u & y & w & w \\ u & x & u & w & y & w \\ u & u & x & w & w & y \\ y & w & w & x & u & u \\ w & y & w & u & x & u \\ w & w & y & u & u & x \end{bmatrix} \begin{bmatrix} i_1 \\ i_2 \\ i_3 \\ i_4 \\ i_5 \\ i_6 \end{bmatrix}
\tag{3.3}
$$
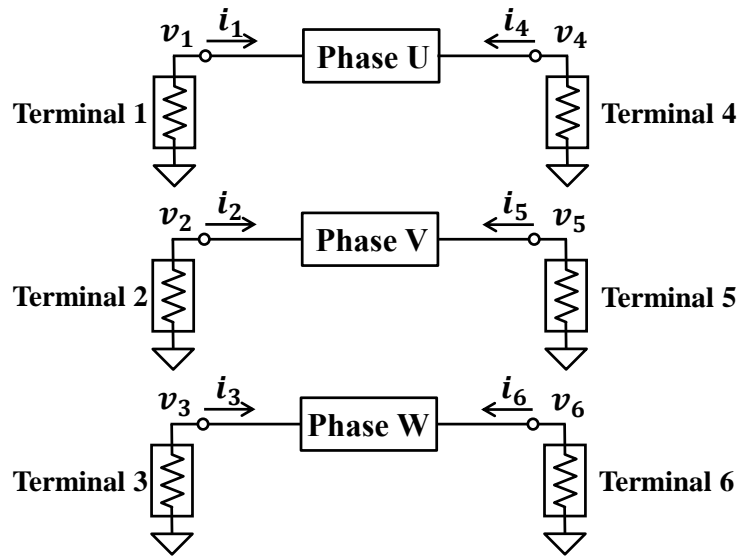
Fig. 3-2. Multi-port network model of a three-phase winding.
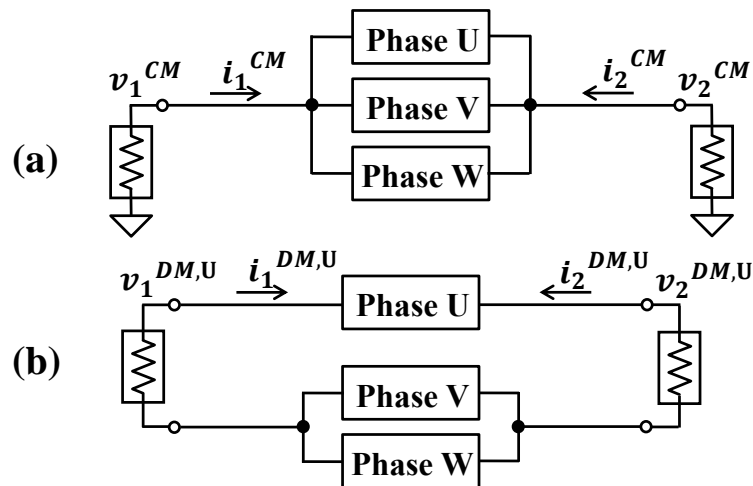
Fig. 3-3. (a) Two-port network for CM connection. (b) Two-port network for DM connection.

(3.3) can be redefined with several sub-matrices as follows:

$$\begin{bmatrix} \mathbf{V_L} \\ \mathbf{V_R} \end{bmatrix} = \begin{bmatrix} \mathbf{Z_X} & \mathbf{Z_Y} \\ \mathbf{Z_Y} & \mathbf{Z_X} \end{bmatrix} \begin{bmatrix} \mathbf{I_L} \\ \mathbf{I_R} \end{bmatrix} \tag{3.4}$$

where $\mathbf{V_L}$ is a three by one matrix of v_1, v_2 and v_3 that are indicated in Fig. 3-2. Similarly, $\mathbf{V_R}$ includes the terminal voltages which are at the right side in the figure. $\mathbf{Z_X}$ and $\mathbf{Z_Y}$ are the three by three sub-matrices of the impedance parameter matrix of (3.3) as follows:

$$\mathbf{V_L} = \begin{bmatrix} v_1 \\ v_2 \\ v_3 \end{bmatrix}, \quad \mathbf{V_R} = \begin{bmatrix} v_4 \\ v_5 \\ v_6 \end{bmatrix}, \quad \mathbf{I_L} = \begin{bmatrix} i_1 \\ i_2 \\ i_3 \end{bmatrix}, \quad \mathbf{I_R} = \begin{bmatrix} i_4 \\ i_5 \\ i_6 \end{bmatrix} \tag{3.5}$$

$$\mathbf{Z_X} = \begin{bmatrix} x & u & u \\ u & x & u \\ u & u & x \end{bmatrix}, \quad \mathbf{Z_Y} = \begin{bmatrix} y & w & w \\ w & y & w \\ w & w & y \end{bmatrix} \tag{3.6}$$

In order to find the values of the unknown x, y, u and w, the relations of the voltages and the currents of CM and DM, which are shown in Fig. 3-3, can be used. The definition of the impedance network of CM and DM is as follows:

$$\begin{bmatrix} v_1^{CM} \\ v_2^{CM} \end{bmatrix} = \begin{bmatrix} z_{11}^{CM} & z_{12}^{CM} \\ z_{21}^{CM} & z_{22}^{CM} \end{bmatrix} \begin{bmatrix} i_1^{CM} \\ i_2^{CM} \end{bmatrix}$$

$$\begin{bmatrix} v_1^{DM,\mathbf{U}} \\ v_2^{DM,\mathbf{U}} \end{bmatrix} = \begin{bmatrix} z_{11}^{DM,\mathbf{U}} & z_{12}^{DM,\mathbf{U}} \\ z_{21}^{DM,\mathbf{U}} & z_{22}^{DM,\mathbf{U}} \end{bmatrix} \begin{bmatrix} i_1^{DM,\mathbf{U}} \\ i_2^{DM,\mathbf{U}} \end{bmatrix} \tag{3.7}$$

$$\begin{bmatrix} v_1^{DM,\mathbf{V}} \\ v_2^{DM,\mathbf{V}} \end{bmatrix} = \begin{bmatrix} z_{11}^{DM,\mathbf{V}} & z_{12}^{DM,\mathbf{V}} \\ z_{21}^{DM,\mathbf{V}} & z_{22}^{DM,\mathbf{V}} \end{bmatrix} \begin{bmatrix} i_1^{DM,\mathbf{V}} \\ i_2^{DM,\mathbf{V}} \end{bmatrix}$$

By relating the voltage and currents between CM, DM, and single phase, the following conversion matrix formula can be obtained:

$$\begin{bmatrix} v_1^{CM} \\ v_1^{DM,\mathbf{U}} \\ v_1^{DM,\mathbf{V}} \end{bmatrix} = \begin{bmatrix} \dfrac{1}{3} & \dfrac{1}{3} & \dfrac{1}{3} \\ 1 & -\dfrac{1}{2} & -\dfrac{1}{2} \\ -\dfrac{1}{2} & 1 & -\dfrac{1}{2} \end{bmatrix} \begin{bmatrix} v_1 \\ v_2 \\ v_3 \end{bmatrix} \implies \mathbf{V_{M,L}} = \mathbf{M_V V_L} \tag{3.8}$$

$$\begin{bmatrix} i_1^{CM} \\ i_1^{DM,\mathbf{U}} \\ i_1^{DM,\mathbf{V}} \end{bmatrix} = \begin{bmatrix} 1 & 1 & 1 \\ \dfrac{1}{2} & -\dfrac{1}{4} & -\dfrac{1}{4} \\ -\dfrac{1}{4} & \dfrac{1}{2} & -\dfrac{1}{4} \end{bmatrix} \begin{bmatrix} i_1 \\ i_2 \\ i_3 \end{bmatrix} \implies \mathbf{I_{M,L}} = \mathbf{M_I I_L} \tag{3.9}$$

$$\begin{bmatrix} v_2^{CM} \\ v_2^{DM,U} \\ v_2^{DM,V} \end{bmatrix} = \begin{bmatrix} \dfrac{1}{3} & \dfrac{1}{3} & \dfrac{1}{3} \\ 1 & -\dfrac{1}{2} & -\dfrac{1}{2} \\ -\dfrac{1}{2} & 1 & -\dfrac{1}{2} \end{bmatrix} \begin{bmatrix} v_4 \\ v_5 \\ v_6 \end{bmatrix} \implies \mathbf{V_{M,R}} = \mathbf{M_V V_R} \tag{3.10}$$

$$\begin{bmatrix} i_2^{CM} \\ i_2^{DM,U} \\ i_2^{DM,V} \end{bmatrix} = \begin{bmatrix} 1 & 1 & 1 \\ \dfrac{1}{2} & -\dfrac{1}{4} & -\dfrac{1}{4} \\ -\dfrac{1}{4} & \dfrac{1}{2} & -\dfrac{1}{4} \end{bmatrix} \begin{bmatrix} i_4 \\ i_5 \\ i_6 \end{bmatrix} \implies \mathbf{I_{M,R}} = \mathbf{M_I I_R} \tag{3.11}$$

where $\mathbf{M_V}$ and $\mathbf{M_I}$ represent transfer matrices between modal and terminal (phase) variables. By using the relation between the matrices $\mathbf{M_V}$, $\mathbf{M_I}$, $\mathbf{Z_X}$ and $\mathbf{Z_Y}$, we can obtain the relation of voltages and currents for CM and DM as follows:

$$\begin{bmatrix} \mathbf{V_{M,L}} \\ \mathbf{V_{M,R}} \end{bmatrix} = \begin{bmatrix} \mathbf{M_V} & \mathbf{0} \\ \mathbf{0} & \mathbf{M_V} \end{bmatrix} \begin{bmatrix} \mathbf{V_L} \\ \mathbf{V_R} \end{bmatrix} \tag{3.12}$$

$$\begin{bmatrix} \mathbf{V_{M,L}} \\ \mathbf{V_{M,R}} \end{bmatrix} = \begin{bmatrix} \mathbf{M_V} & \mathbf{0} \\ \mathbf{0} & \mathbf{M_V} \end{bmatrix} \begin{bmatrix} \mathbf{V_L} \\ \mathbf{V_R} \end{bmatrix} \tag{3.13}$$

$$\begin{bmatrix} \mathbf{V_{M,L}} \\ \mathbf{V_{M,R}} \end{bmatrix} = \begin{bmatrix} \mathbf{M_V} & \mathbf{0} \\ \mathbf{0} & \mathbf{M_V} \end{bmatrix} \begin{bmatrix} \mathbf{Z_X} & \mathbf{Z_Y} \\ \mathbf{Z_Y} & \mathbf{Z_X} \end{bmatrix} \begin{bmatrix} \mathbf{M_I^{-1}} & \mathbf{0} \\ \mathbf{0} & \mathbf{M_I^{-1}} \end{bmatrix} \begin{bmatrix} \mathbf{I_{M,L}} \\ \mathbf{I_{M,R}} \end{bmatrix}$$
$$= \begin{bmatrix} \mathbf{M_V Z_X M_I^{-1}} & \mathbf{M_V Z_Y M_I^{-1}} \\ \mathbf{M_V Z_Y M_I^{-1}} & \mathbf{M_V Z_X M_I^{-1}} \end{bmatrix} \begin{bmatrix} \mathbf{I_{M,L}} \\ \mathbf{I_{M,R}} \end{bmatrix} = \mathbf{Z_{CM,DM}} \begin{bmatrix} \mathbf{I_{M,L}} \\ \mathbf{I_{M,R}} \end{bmatrix} \tag{3.14}$$

The calculated values of the off-diagonal terms of each sub-matrix of $\mathbf{Z_{CM,DM}}$ become zero and it can be matched with balanced condition. By calculating the matrix $\mathbf{Z_{CM,DM}}$ with the unknown parameters, we can extract the elements related to CM and DM from (3.14) as follows:

$$\begin{bmatrix} \mathbf{V_{M,L}} \\ \mathbf{V_{M,R}} \end{bmatrix} = \mathbf{Z_{CM,DM}} \begin{bmatrix} \mathbf{I_{M,L}} \\ \mathbf{I_{M,R}} \end{bmatrix} \qquad \left(\because \mathbf{Z_{CM,DM}} = \begin{bmatrix} \mathbf{M_V Z_X M_I^{-1}} & \mathbf{M_V Z_Y M_I^{-1}} \\ \mathbf{M_V Z_Y M_I^{-1}} & \mathbf{M_V Z_X M_I^{-1}} \end{bmatrix} \right)$$

$$\Rightarrow \begin{bmatrix} v_1^{CM} \\ v_1^{DM,U} \\ v_1^{DM,V} \\ v_2^{CM} \\ v_2^{DM,U} \\ v_2^{DM,V} \end{bmatrix} = \begin{bmatrix} \dfrac{x+2u}{3} & 0 & 0 & \dfrac{y+2w}{3} & 0 & 0 \\ 0 & 2x-2u & 0 & 0 & 2y-2w & 0 \\ 0 & 0 & 2x-2u & 0 & 0 & 2y-2w \\ \dfrac{y+2w}{3} & 0 & 0 & \dfrac{x+2u}{3} & 0 & 0 \\ 0 & 2y-2w & 0 & 0 & 2x-2u & 0 \\ 0 & 0 & 2y-2w & 0 & 0 & 2x-2u \end{bmatrix} \begin{bmatrix} i_1^{CM} \\ i_1^{DM,U} \\ i_1^{DM,V} \\ i_2^{CM} \\ i_2^{DM,U} \\ i_2^{DM,V} \end{bmatrix} \quad (3.15)$$

$$\begin{bmatrix} v_1^{CM} \\ v_2^{CM} \end{bmatrix} = \frac{1}{3} \begin{bmatrix} x+2u & y+2w \\ y+2w & x+2u \end{bmatrix} \begin{bmatrix} i_1^{CM} \\ i_2^{CM} \end{bmatrix}$$

$$\begin{bmatrix} v_1^{DM,U} \\ v_2^{DM,U} \end{bmatrix} = 2 \begin{bmatrix} x-u & y-w \\ y-w & x-u \end{bmatrix} \begin{bmatrix} i_1^{DM,U} \\ i_2^{DM,U} \end{bmatrix} \qquad (3.16)$$

Finally, we can obtain the unknown parameters for the impedance matrix as follows:

$$z_{11}^{CM} = z_{22}^{CM} = \frac{1}{3}(x+2u), \quad z_{12}^{CM} = z_{21}^{CM} = \frac{1}{3}(y+2w)$$

$$(3.17)$$

$$z_{11}^{DM} = z_{22}^{DM} = 2(x-u), \quad z_{12}^{DM} = z_{21}^{DM} = 2(y-w)$$

$$x = z_{11}^{CM} + \frac{1}{3} z_{11}^{DM}, \quad y = z_{12}^{CM} + \frac{1}{3} z_{12}^{DM}$$

$$(3.18)$$

$$u = z_{11}^{CM} - \frac{1}{6} z_{11}^{DM}, \quad w = z_{12}^{CM} - \frac{1}{6} z_{12}^{DM}$$

Note that the parameter x is the self-impedance and y is the transfer-impedance for the single phase line. Meanwhile, u and w represent the near-end and far-end (phase-to-phase) transfer-impedances, respectively.

To verify the calculated results, the input impedance of the self-coupling term for the open-ended single phase line is compared with the measurement result as shown in Fig. 3-4. As can be seen in the results, even though there is a little difference caused by the assumption of symmetric structure, the calculated input impedance shows a close match with the measured one.

(a)

(b)
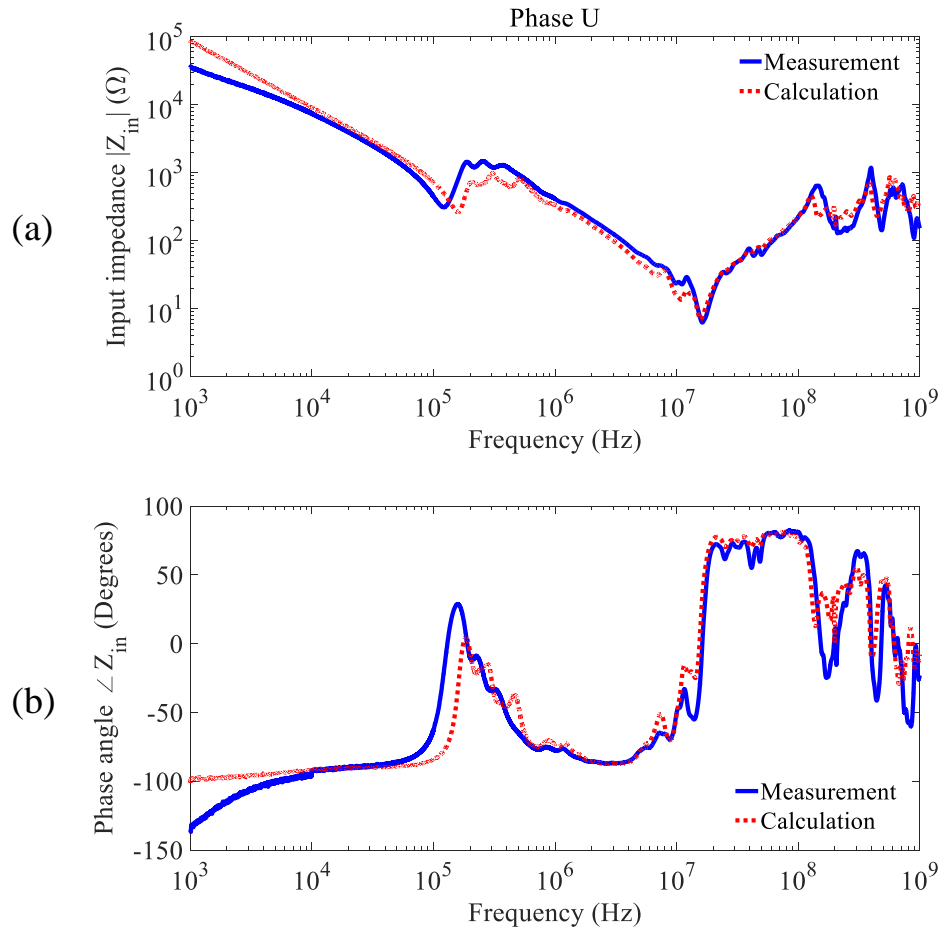
Fig. 3-4. Comparison between measured and calculated input impedance. (a) Magnitude of input impedance. (b) Phase angle of input impedance.

3.3.2.Equivalent Circuit Model under Balanced Excitation Condition

By using the parameters in (3.18), a T-equivalent circuit model including the phase-to-phase coupling can be considered as shown in Fig. 3-5 (a). The sub-circuit in the middle of the equivalent circuit model, which constructed by x and y parameters, represents the single phase line model without phase-to-phase coupling factors. Then, the phase-to-phase coupling effects can be added to the left and the right sides of the uncoupled T-equivalent circuit model by using the parameters u and w. The constructed T-equivalent circuit can be applied to any winding connection and terminal excitation for the three-phase structure.
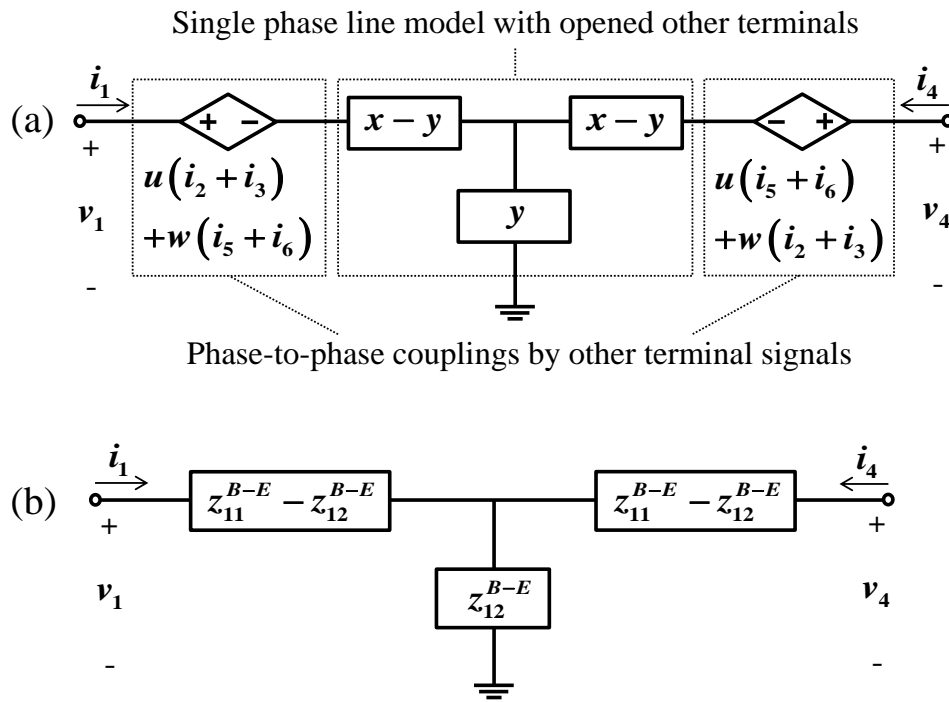
Fig. 3-5. The T-equivalent circuit models of the single-phase line with considering the phase-to-phase coupling: (a) T-equivalent circuit model that separates phase-to-phase coupling from uncoupled model. (b) Simplified T-equivalent circuit model under the balanced excitation condition.

Assuming the balanced three-phase excitation on the left-side terminals (1 to 3) and the right-side terminals (4 to 6) as shown below,

$$i_1 + i_2 + i_3 = 0, \quad i_4 + i_5 + i_6 = 0 \qquad (3.19)$$

the expression of the dependence sources of the equivalent model can be simplified as shown in Fig. 3-5 (b). By the definition of the Z-parameter, the elements of the T-equivalent circuit for the balanced excitation can be calculated as follows:

$$\mathbf{Z}_{Balanced-Excitation} = \begin{bmatrix} z_{11}^{B-E} & z_{12}^{B-E} \\ z_{21}^{B-E} & z_{22}^{B-E} \end{bmatrix} = \begin{bmatrix} x-u & y-w \\ y-w & x-u \end{bmatrix} \tag{3.20}$$

(a)

(b)
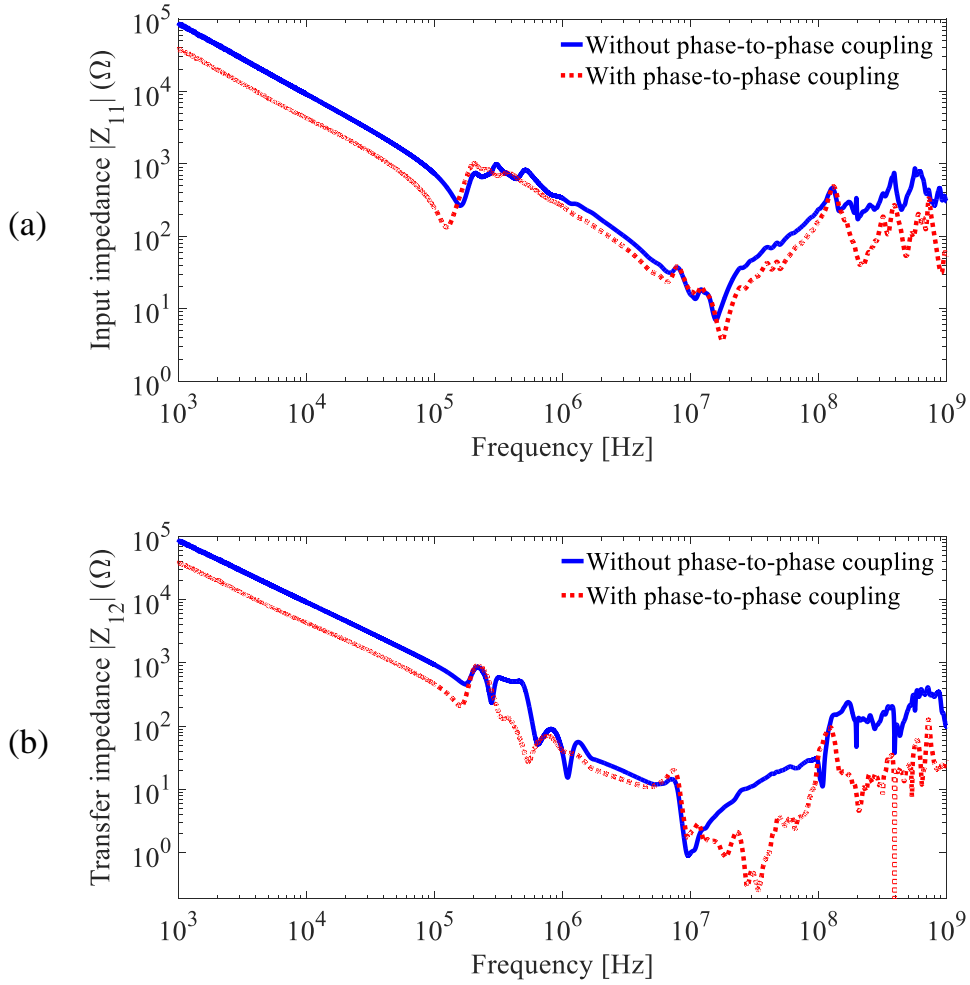
Fig. 3-6. Input impedances and transfer impedances for the single phase line with and without considering phase-to-phase coupling effect.

Since the proposed T-equivalent circuit model includes the phase-to-phase coupling parameters, we can observe how the phase-to-phase coupling affects the single-phase line by comparing with the input and the transfer impedances of the uncoupled model. As shown in Fig. 3-6, the impedances including the phase-to-phase coupling decrease throughout the observed frequency region.

3.4. Network Parameter Extraction for the Winding-to-Shaft Coupling Elements

3.4.1. The Generation of the Shaft Voltage

The proposed multi-port network parameter extraction method can be extended and applied to investigate the shaft voltage effect in the motor structure. Since the PWM inverter has been used widely in the motor drive system, the shaft voltage has become a momentous problem due to the high-frequency switching noise. The phenomenon of the generation of the shaft voltage and bearing currents by the high-speed switching of the ASD were studied in 1990s [38-39]. Moreover, the study of the shaft voltage by end-winding structures was presented [40].

The summary of the previous studies on the generated shaft voltage in the ac motor is shown in Fig. 3-7, which describe the EM couplings in cross-section of a three-phase ac motor. Because of the circulating EM noise current, and asymmetric structure, different voltages are induced at the end-sides of the shaft, as $V_{shaf\text{-}1}$ and $V_{shaft\text{-}2}$ in the figure. Therefore, the non-zero shaft voltage along its axis becomes as a noise source, and EM noise current propagates to the other devices by the mechanical connection.
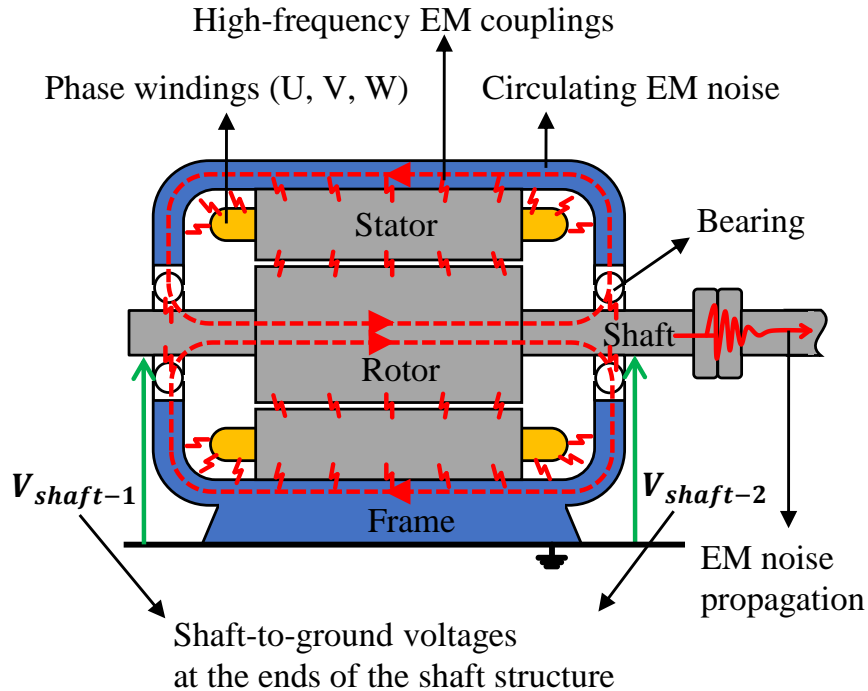
Fig. 3-7. The circulating CM current loop and the induced shaft voltage by EM coupling effects in the ac motor structure.
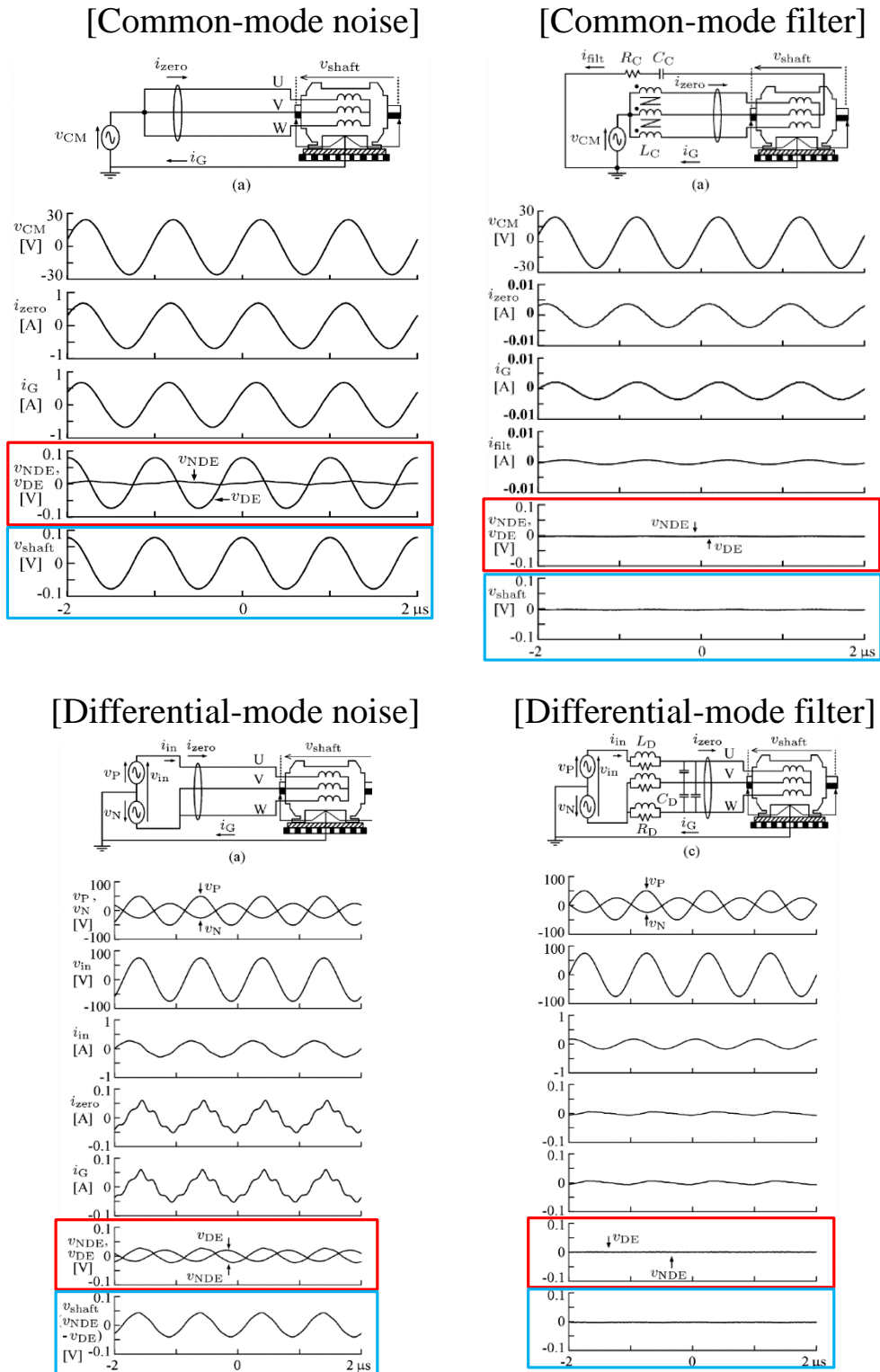
Fig. 3-8. The experimental test of the shaft voltage generation when CM and DM voltage are applied to the ac motor [41-42].

Fig. 3-8 show the induced voltages at the shaft end-sides when CM and DM noise voltages are induced in the motor. As shown in the measured results, the shaft end-sides have different level of voltages respectively, and it induces the shaft voltage along its axis. The induced voltages at the shaft end-sides are almost disappeared when the CM and DM noise filters are used in the system. From this study, we can know that one of the main reasons of the shaft voltages is the CM and DM EM noise which are generated by the phase windings.

The general solution to reduce the shaft voltage is shown in Fig. 3-9 [43-44]. To divert the induced shaft current away from bearings, shaft grounding brush is used typically. However, the problems, such as mechanical wear, brush sparks, can be occurred because of mechanical contact. Moreover, it is not the fundamental solution to reduce the EM noise and couplings. Therefore, the coupling mechanism analysis for the generated shaft voltage is essential, and the method to extract the coupling parameters between CM, DM noise and induced shaft voltage should be established.
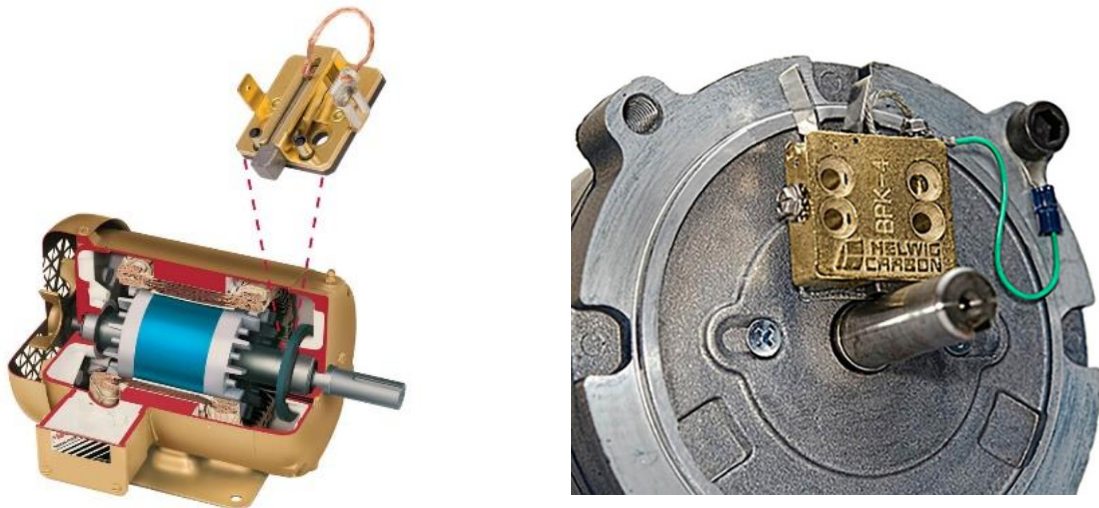
Fig. 3-9. The typical solutions to reduce the shaft voltage in the ac motor. (Electrical short circuit between shaft and frame by mechanical brush) [43-44]

To understand the transmission effects from the CM noise and the DM noise to the shaft, a method to extract the network parameters considering their interaction is proposed in this section. The five-port impedance parameter matrix including the ports as the terminals of three-phase windings and shaft end-sides is constructed by two-port network analysis. The five-port network is converted to the mixed-mode parameters by the transfer matrices. The extracted mixed-mode matrix includes the transfer impedance parameters between CM, DM and shaft end-sides.

3.4.2.Five-Port Network Parameter Extraction by Two-Port Network Measurement

The five-port network parameters to extract the impedances between three-phase windings and shaft end sides can be constructed by the data of several two-port measurements. The concept of the five-ports including the shaft structure are set as shown in Fig. 3-10 (a). The terminals of the three-phase windings have each port, and the five-port network is composed by including left and right sides of the shaft structure. The experiment setup with the connected five-ports in the testing ac motor is shown in Fig. 3-10 (b). The measurement is implemented by a two-port vector network analyzer as shown in Fig. 3-10 (c). During measurement, 50 ohms are terminated for the other ports except measuring two ports, and the motor frame is set as the reference ground.

The Table 3-1 shows the two-port measurements to construct the full five-port network parameter matrix which include the terminals of three phase windings and shaft end sides as the ports. Each measurement data of Table 3-1 has two by two network parameter matrix. The five-port impedance parameter matrix including the elements for U, V, W shaft-left and shaft-right can be constructed by selecting the measured data in the two-port network matrices. The constructed five-port network parameter matrix is as follow:

$$
\begin{array}{c}

\begin{matrix} Shaft-left & Shaft-right & Phase\ U & Phase\ V & Phase\ W \end{matrix} \\
\begin{matrix} Shaft-left \\ Shaft-right \\ Phase\ U \\ Phase\ V \\ Phase\ W \end{matrix}
\begin{bmatrix}
Z_{11} & Z_{12} & Z_{13} & Z_{14} & Z_{15} \\
Z_{21} & Z_{22} & Z_{23} & Z_{24} & Z_{25} \\
Z_{31} & Z_{32} & Z_{33} & Z_{34} & Z_{35} \\
Z_{41} & Z_{42} & Z_{43} & Z_{44} & Z_{45} \\
Z_{51} & Z_{52} & Z_{53} & Z_{54} & Z_{55}
\end{bmatrix}
\end{array}
\tag{3.21}
$$

Fig. 3-11 shows the results of the constructed five-port network parameters of (3.21). The left-upper 2 by 2 data represents the characteristics of the shaft itself. The right-upper 2 by 3 data and left-bottom 3 by 2 data represent the coupling parameters between phase windings and shaft end-sides. The right-bottom 3 by 3 data represent the characteristics of the three-phase windings. The constructed five-port network parameters can be used as the raw-data to extract the mixed-mode network parameters.
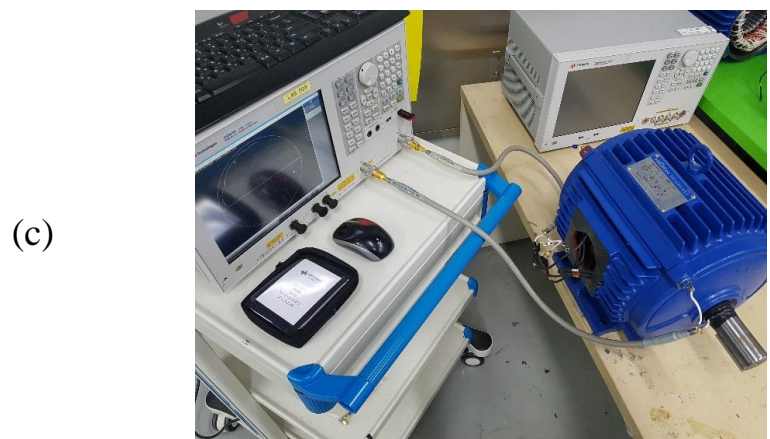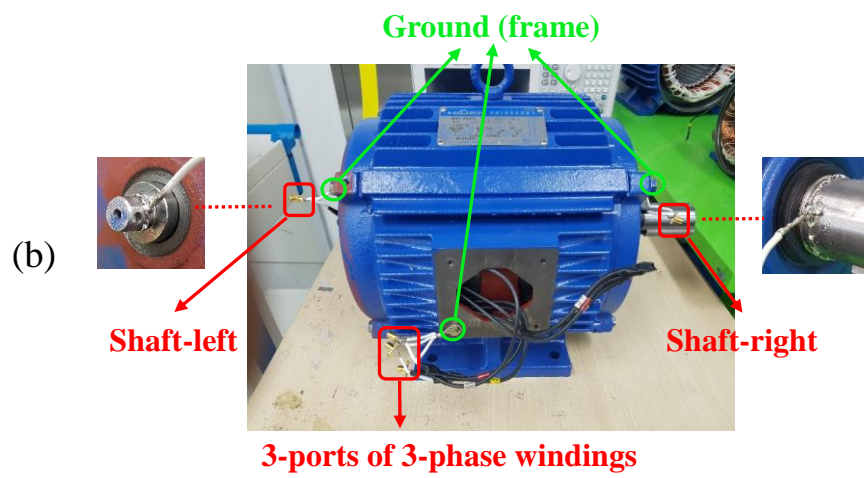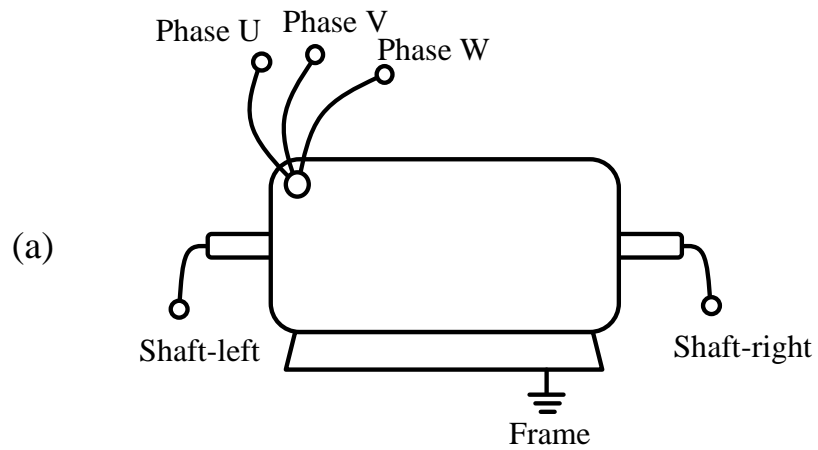
Fig. 3-10. (a) The concept of the five-port network to extract the impedance parameters. (b) Experiment setup of the five-port network for an ac motor. (b) Measurement by two-port vector network analyzer.

Table 3-1. The two-port measurement to construct the full five-port network parameters including three-phase and shaft end sides

Measurement order	Port 1	Port 2
Measurement 1	Shaft-left	Shaft-right
Measurement 2	Shaft-left	Phase U
Measurement 3	Shaft-left	Phase V
Measurement 4	Shaft-left	Phase W
Measurement 5	Shaft-right	Phase U
Measurement 6	Shaft-right	Phase V
Measurement 7	Shaft-right	Phase W
Measurement 8	Phase U	Phase V
Measurement 9	Phase U	Phase W
Measurement 10	Phase V	Phase W
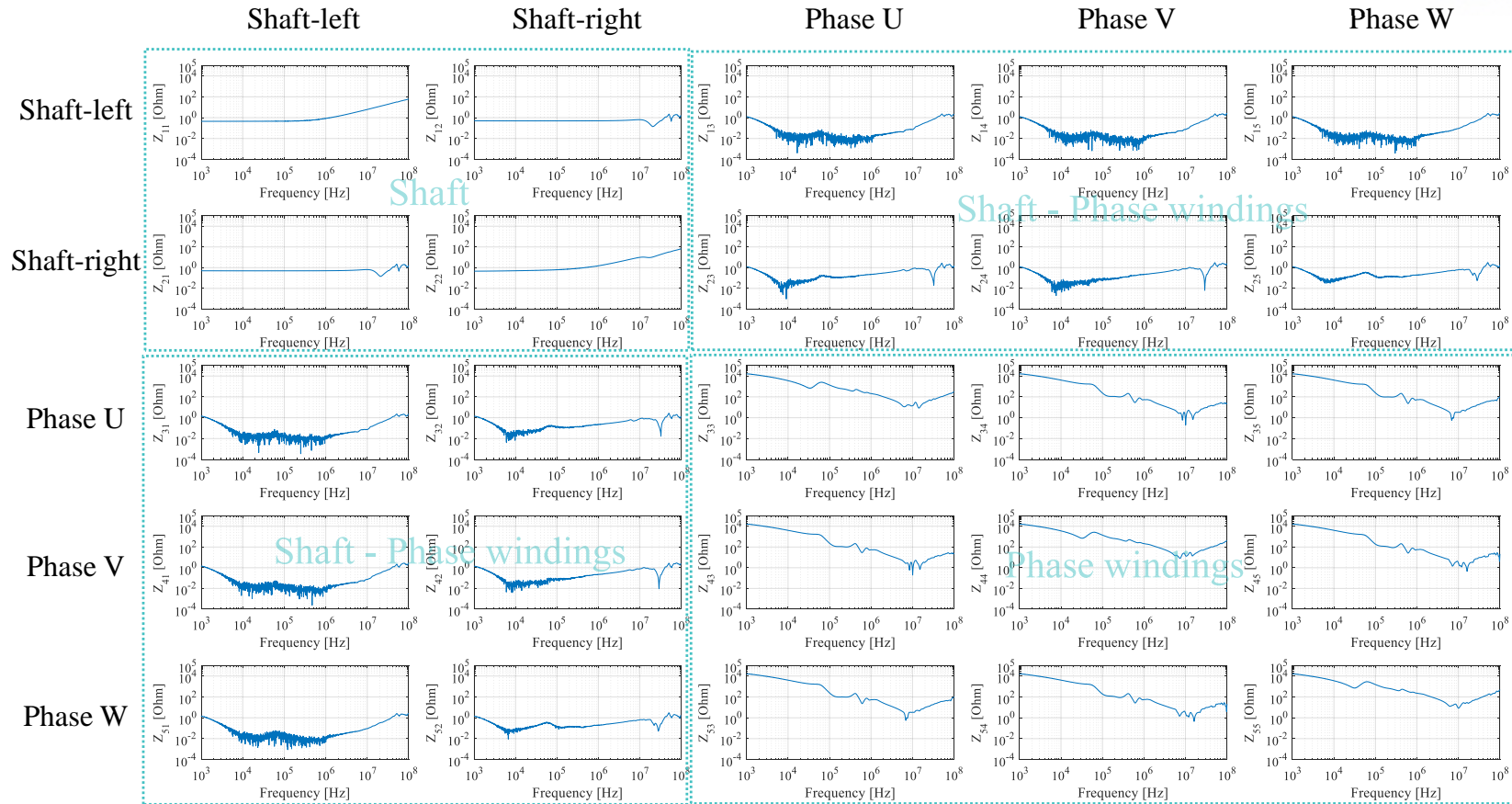
Fig. 3-11. The constructed five-port impedance parameters for the three-phase terminals and shaft end sides.

3.4.3. Measurement of the Common-Mode Current in the Motor Drive System

In this section, the conversion method from the constructed five-port network parameters to the mixed-mode network parameters is described. The definition of the constructed five-port network parameter matrix in the previous section is shown. The matrices are named as port voltages **V**, port currents **I** and port impedance parameters **Z** respectively as follows:

$$
\begin{bmatrix} V_{shaft-right} \\ V_{shaft-left} \\ V_U \\ V_V \\ V_W \end{bmatrix} = \begin{bmatrix} Z_{11} & Z_{12} & Z_{13} & Z_{14} & Z_{15} \\ Z_{21} & Z_{22} & Z_{23} & Z_{24} & Z_{25} \\ Z_{31} & Z_{32} & Z_{33} & Z_{34} & Z_{35} \\ Z_{41} & Z_{42} & Z_{43} & Z_{44} & Z_{45} \\ Z_{51} & Z_{52} & Z_{53} & Z_{54} & Z_{55} \end{bmatrix} \begin{bmatrix} I_{shaft-right} \\ I_{shaft-left} \\ I_U \\ I_V \\ I_W \end{bmatrix}
$$
$$\Rightarrow \quad \mathbf{V} = \mathbf{ZI}$$
(3.22)

To extract the EM coupling effect from CM and DM noise to the shaft end sides, the proposed extraction method of network parameters in the previous section can be used. The port voltages matrix **V** can be converted to the mixed-mode voltages matrix, **V$_M$** which has the components as shaft left voltage, shaft right voltage, common-mode voltage, differential-mode voltage for the phase U, and differential-mode voltage for the phase V, through the defined voltage conversion matrix, **M$_V$**. The voltage conversion matrix is defined from the relations between CM, DM and port voltages under the consideration of the mixed-mode connections. Similarly, the mixed-mode currents matrix, **I$_M$**, can be converted from the port currents matrix through the constructed current conversion matrix, **M$_I$**, as follows:

$$
\begin{bmatrix} V_{shaft-right} \\ V_{shaft-left} \\ V_{CM} \\ V_{DM,U} \\ V_{DM,V} \end{bmatrix} = \begin{bmatrix} 1 & 0 & 0 & 0 & 0 \\ 0 & 1 & 0 & 0 & 0 \\ 0 & 0 & \dfrac{1}{3} & \dfrac{1}{3} & \dfrac{1}{3} \\ 0 & 0 & 1 & -\dfrac{1}{2} & -\dfrac{1}{2} \\ 0 & 0 & -\dfrac{1}{2} & 1 & -\dfrac{1}{2} \end{bmatrix} \begin{bmatrix} V_{shaft-right} \\ V_{shaft-left} \\ V_U \\ V_V \\ V_W \end{bmatrix}
$$
$$\Rightarrow \quad \mathbf{V_M} = \mathbf{M_V V}$$
(3.23)

61

$$\begin{bmatrix} I_{shaft-right} \\ I_{shaft-left} \\ I_{CM} \\ I_{DM,U} \\ I_{DM,V} \end{bmatrix} = \begin{bmatrix} 1 & 0 & 0 & 0 & 0 \\ 0 & 1 & 0 & 0 & 0 \\ 0 & 0 & 1 & 1 & 1 \\ 0 & 0 & \dfrac{1}{2} & -\dfrac{1}{4} & -\dfrac{1}{4} \\ 0 & 0 & -\dfrac{1}{4} & \dfrac{1}{2} & -\dfrac{1}{4} \end{bmatrix} \begin{bmatrix} I_{shaft-right} \\ I_{shaft-left} \\ I_{U} \\ I_{V} \\ I_{W} \end{bmatrix} \qquad (3.24)$$

$$\Rightarrow \quad \mathbf{I_M = M_I I}$$

By using these three matrix relations of (3.22), (3.23), and (3.24), finally, the mixed-mode impedance parameter matrix, $\mathbf{Z_M}$, can be obtained through the below derivation.

$$\begin{aligned} \mathbf{V} &= \mathbf{M_V^{-1} V_M} \\ \mathbf{I} &= \mathbf{M_I^{-1} I_M} \\ \mathbf{V} &= \mathbf{ZI} \quad \rightarrow \quad \mathbf{M_V^{-1} V_M = Z M_I^{-1} I_M} \\ \mathbf{Z_M} &= \mathbf{M_V Z M_I^{-1}} \end{aligned} \qquad (3.25)$$

The mixed-mode impedance, $\mathbf{Z_M}$, includes the EM coupling effect between CM, DM, and shaft end sides as follow:

$$\begin{array}{c} \begin{array}{ccccc} Shaft-left & Shaft-right & CM & DM_U & DM_V \end{array} \\ \begin{array}{c} Shaft-left \\ Shaft-right \\ CM \\ DM_U \\ DM_V \end{array} \begin{bmatrix} Z_{shaft-left,shaft-left} & Z_{shaft-left,shaft-right} & Z_{shaft-left,CM} & Z_{shaft-left,DM_U} & Z_{shaft-left,DM_V} \\ Z_{shaft-right,shaft-left} & Z_{shaft-right,shaft-right} & Z_{shaft-right,CM} & Z_{shaft-right,DM_U} & Z_{shaft-right,DM_V} \\ Z_{CM,shaft-left} & Z_{CM,shaft-right} & Z_{CM,CM} & Z_{CM,DM_U} & Z_{CM,DM_V} \\ Z_{DM_U,shaft-left} & Z_{DM_U,shaft-right} & Z_{DM_U,CM} & Z_{DM_U,DM_U} & Z_{DM_U,DM_V} \\ Z_{DM_V,shaft-left} & Z_{DM_V,shaft-right} & Z_{DM_V,CM} & Z_{DM_V,DM_U} & Z_{DM_V,DM_V} \end{bmatrix} \end{array} \qquad (3.26)$$

The elements of the two-by-two sub-matrix in left-upper side of $\mathbf{Z_M}$ represent the impedances of shaft structure itself. The elements of the three-by-three sub-matrix in right-bottom side of $\mathbf{Z_M}$ represent the relations between CM and DM. The elements of the two-by-three sub-matrix in right-upper side of $\mathbf{Z_M}$, the elements of the three-by-two sub-matrix in left-bottom side of $\mathbf{Z_M}$ represent the. The converted results of $\mathbf{Z_M}$ is shown in Fig. 3-12. As shown in the result, the EM coupling effect that CM and DM noise affect the shaft end sides can be estimated by using the proposed extraction method.
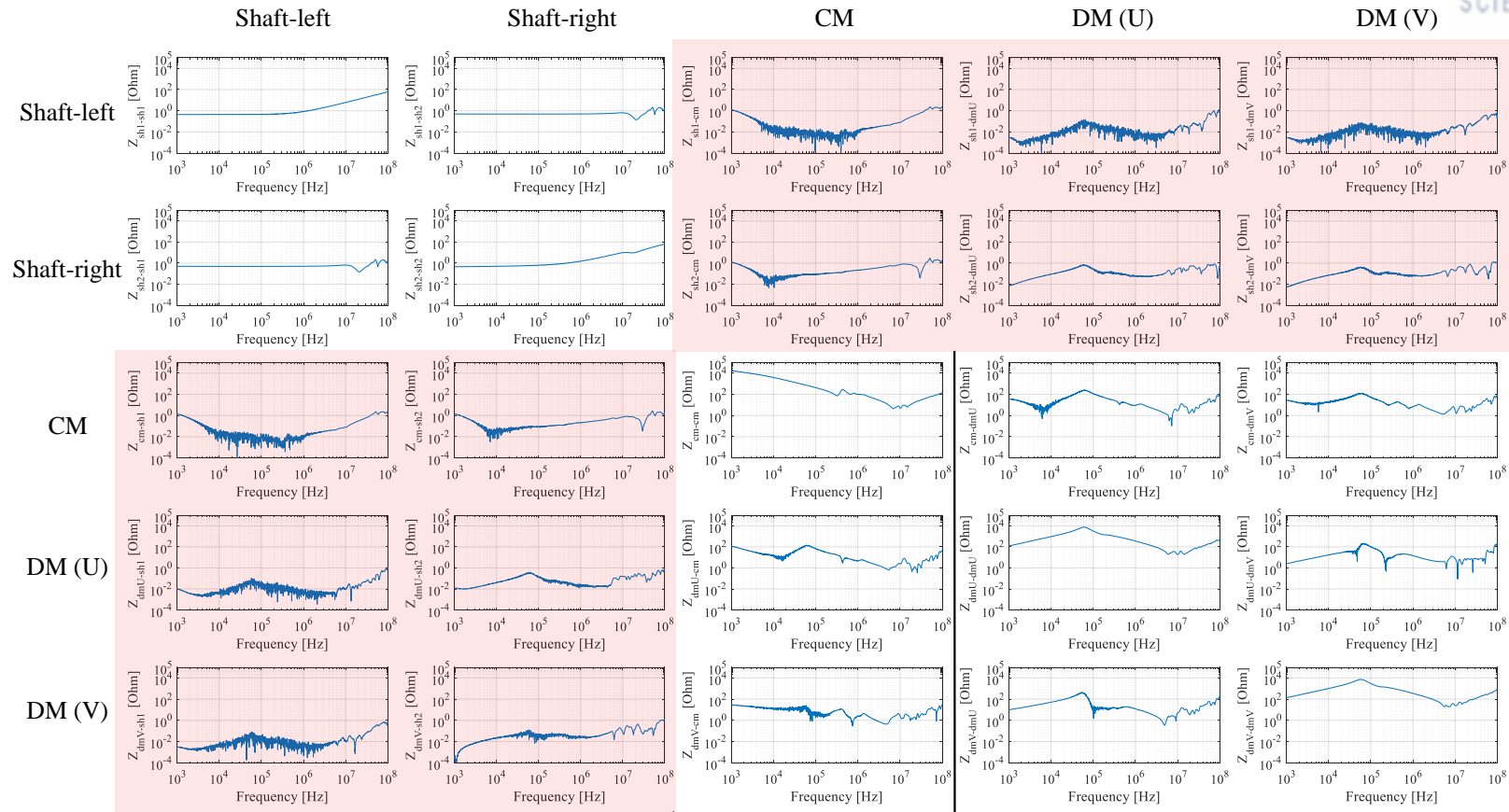
The EM coupling effect that CM or DM affect to the shaft end sides

Fig. 3-12. The extracted results of the converted impedance matrix $\mathbf{Z_M}$.

3.4.4.EM Coupling Parameters in the Symmetrical Motor Structure

To investigate the change of the final extracted mixed-mode impedance parameters $\mathbf{Z_M}$ when the motor has completely symmetrical winding structure, the measured five-port raw-data $\mathbf{Z}$ is reconstituted as shown in Fig. 3-13. The parameters between the phase winding to the shaft-left are set by same parameter, Z_{13} as shown in the purple box, and the parameters between the phase winding to the shaft-right are set by same parameter, Z_{23} as shown in the yellow box. Similarly, the parameters of the phase windings are set as Z_{33}, and the parameters between the phase windings are set as Z_{34}. Then, the reconstituted impedance parameter matrix is used to extract the mixed-mode network parameters $\mathbf{Z_M}$ for the completely symmetric winding structure.
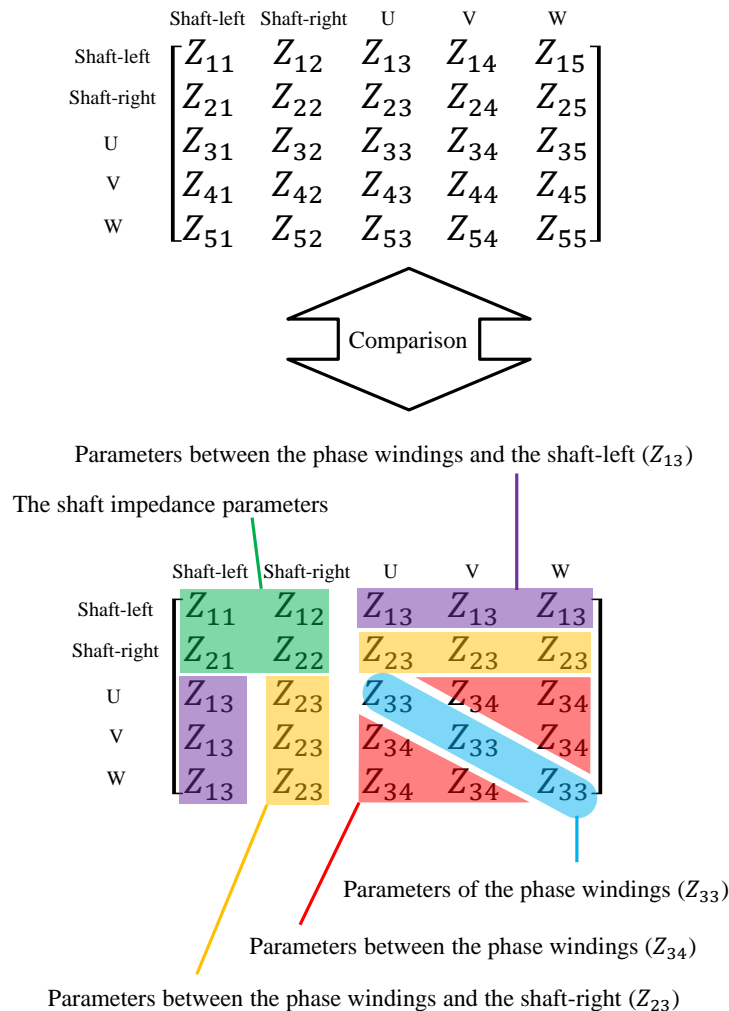
Fig. 3-13. The reconstructed impedance parameter matrix $\mathbf{Z}$ for complete symmetric structure of the ac motor.
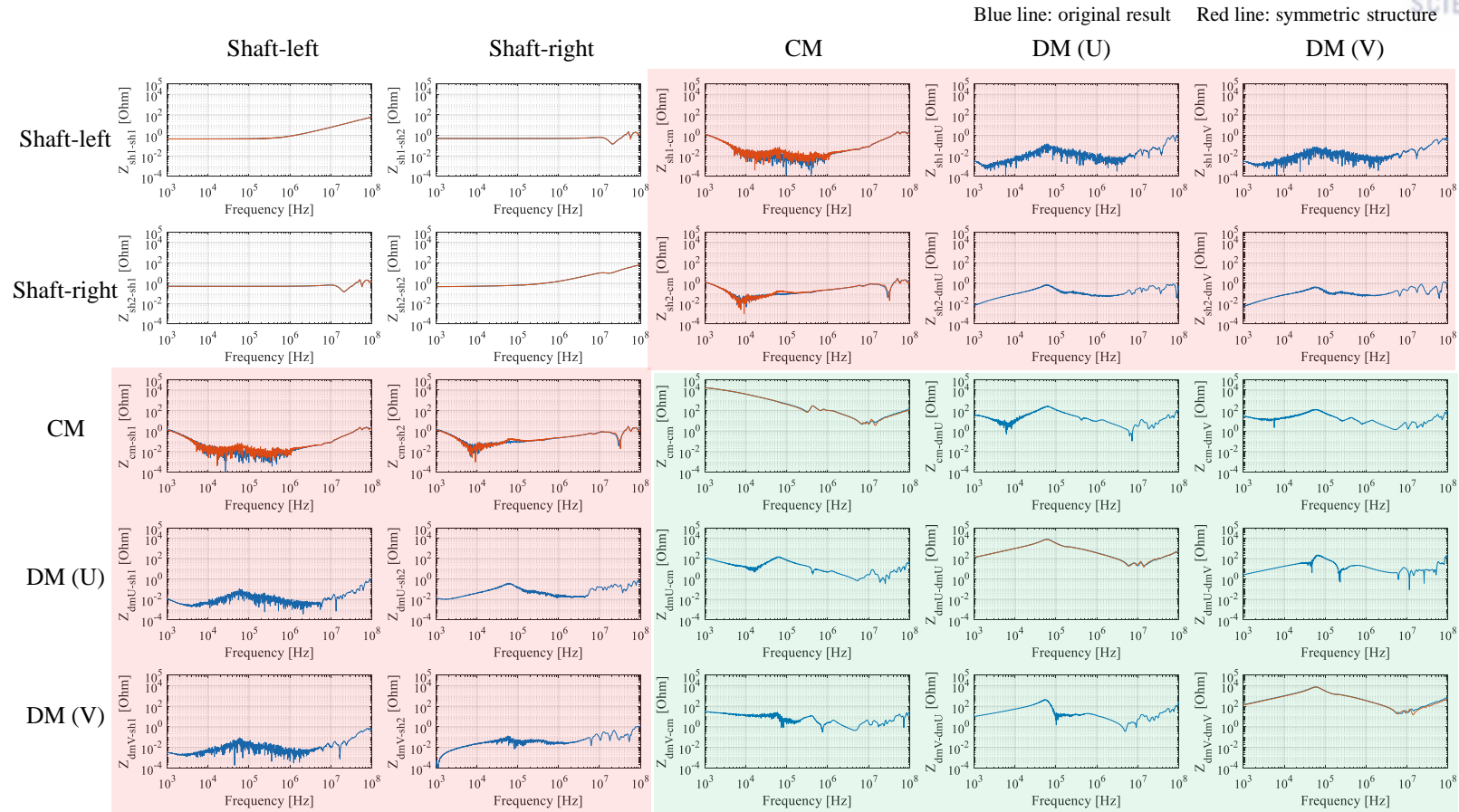
Fig. 3-14. The comparison of the converted mixed-mode impedance parameters between the original result and assumed symmetric structure

The converted result of $\mathbf{Z_M}$ when the ac motor has symmetrical structure is compared with the original result of Fig. 3-12 as shown in Fig. 3-14. From the results, we can know that the DM noise does not propagate to the shaft end sides if the ac motor has completely symmetrical winding structure. In addition, the CM noise and DM noise do not have any interaction in the symmetric structure

3.5. Summary

In this chapter, the method to extract the multi-network parameters for the three-phase windings in the ac motor was proposed. The full six-port network parameters of the three-phase winding structure could be extracted by the two-port mixed-mode (CM and DM) network systems. The proposed method can extract all the self- and mutual-impedances of the three-phase windings by simple matrix conversion. Moreover, using the extracted parameters, an equivalent circuit model containing the phase-to-phase coupling can be constructed. While the proposed equivalent circuit model simplifies the complicated high-frequency response of the stator winding obtained from measurement or electromagnetic-field simulation data, it can capture the high-frequency behavior accurately and enables the prediction of the phase-to-phase coupling effects. The wide-band model of ac machines with the improved accuracy is expected to be used for the EMC-aware design and the optimization of ac motors. The simplified model can be used for the motor drive system simulation, including inverter and cables.

In addition, extraction method for the EM coupling parameters between mixed-mode and shaft end-sides was proposed. To investigate the shaft voltages, five-port network which is consist of phase U, phase V, phase W, shaft-left and shaft-right is constructed by two-port measurements. The five-port network is converted to the mixed-mode network which includes the EM coupling parameters between CM, DM and shaft end-sides. In addition, we confirmed that the differential-mode noise does not propagate to the shaft structure if the motor has symmetrical winding structure. By the proposed method, the amount of CM and DM noise, which is transferred to shaft end sides, can be extracted as the form of impedance parameter. Therefore, we can eliminate the shaft voltage through impedance matching using the extracted parameter information by the proposed method.

Chapter IV

EMC-Aware Design of an AC Motor

4.1. Introduction

In this chapter, a design method for the EMC-aware ac motor is proposed by characterizing the input impedances. To defined the design parameter that is effective to change the characteristic of input impedance, the analysis for the elements of the PUL equivalent circuit model which is proposed in Chapter II is performed.

Moreover, a method to calculate the EM field for the realistic full winding structure is proposed. The calculation method for the multi-port network including all the conductors is presented to extract the characteristic of the phase line from the simulated *RLGC* matrix data. To verify the proposed prediction method of the EM characteristic for the ac motor, the input impedances of the calculated motor model are compared with the measurement.

In addition, various motor models are designed to investigate the variation of the input impedance by an automated design code. The main design parameters to be changed are determined by the structural parameters corresponding to the elements that have a large effect on the PUL equivalent circuit model. Through the investigation of the changing input impedance by the design parameters, an EMC-aware design method of the ac motor is defined. To validate the EMI characteristics of the modeled ac motors by the proposed method, several prototype ac motors are redesigned for the experiment. The CM currents are measured when the redesigned motors are operating by the inverter drive, and the reduction of the CM current by the design parameter is observed.

4.2. Input Impedance Analysis of the AC Motor over Wide Frequency Range

Characterizing the CM input impedance is important to understand the frequency-dependent behavior of the EM noise for electrical devices. In systems driven by voltage sources, high input impedance can reduce the CM current and be durable for the EM noise or the surge voltage. To investigate the characteristics of the input impedance for the ac motor, several induction motors are measured by a vector network analyzer as shown in Fig. 4-1. In the ac motors, both induction and synchronous machines have the same stator winding method, therefore we tested the induction motors which is relatively easy to approach. Both of the fully assembled motors and the stator winding structures without rotors are measured to examine the CM input impedance of the windings.
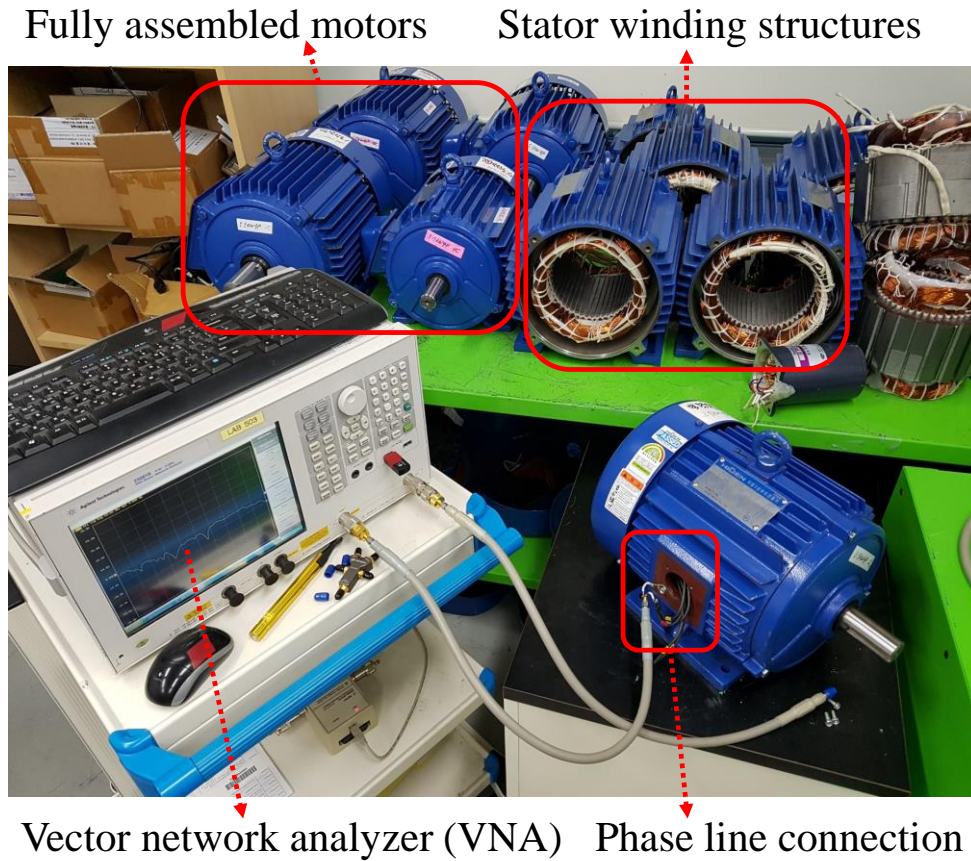
Fig. 4-1. The measurement setup to extract the characteristics of the input impedance for the ac motors by vector network analyzer.

Table 4-1. Specifications of the measured induction motors

	3.7KW (KMH-05HK1)	5.5KW (KMH-08HK1)	7.5KW (KMH-10HK1)
Poles	4	4	4
Slots	48	48	48
Turns per winding	22	35	26
Parallel conductors	3	2	2
Parallel circuits	1	2	2
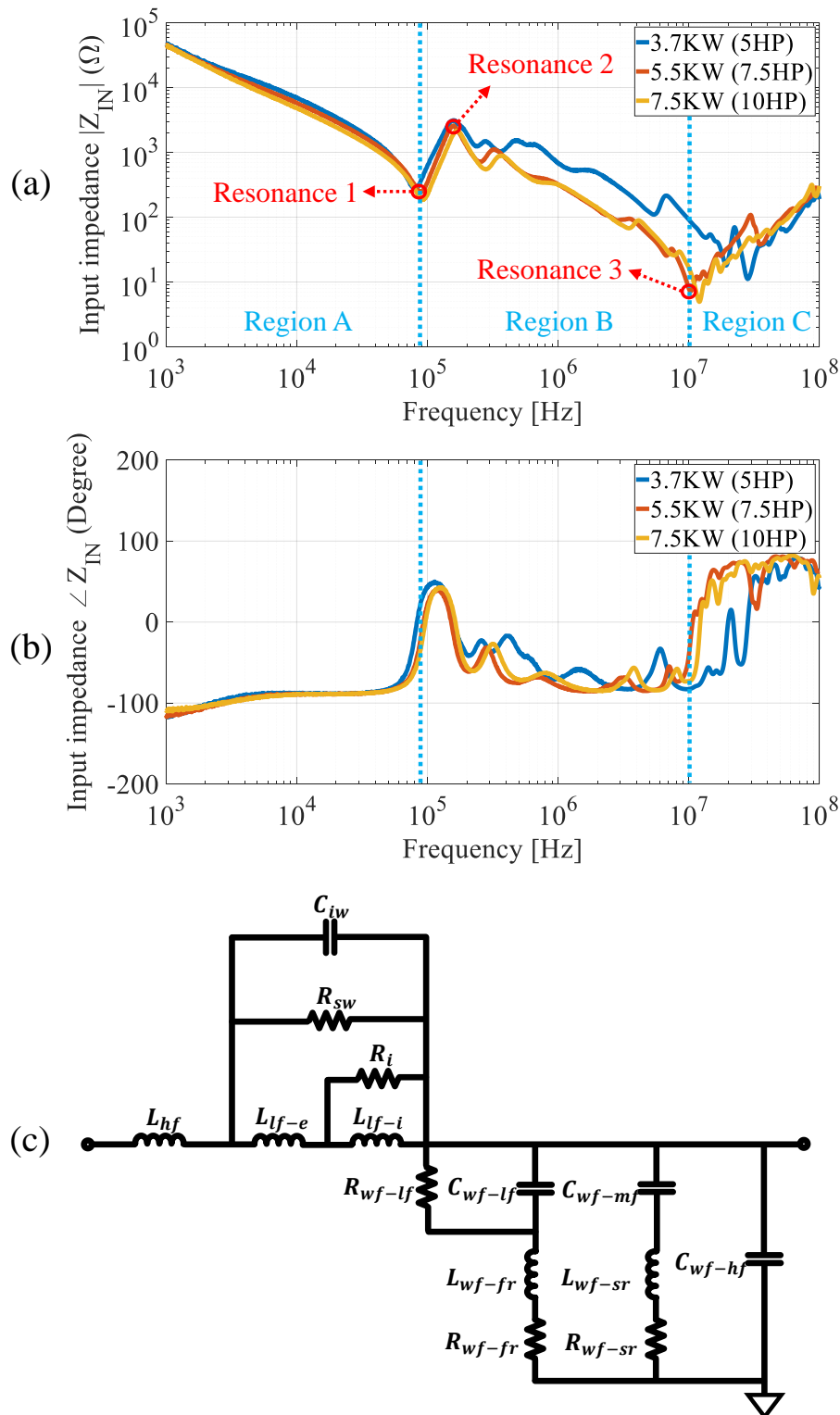
Fig. 4-2.   (a) The measured magnitudes of the input impedances for 3.7KW, 5.5KW and 7.5KW induction motors. (a) The measured phases of the input impedances for 3.7KW, 5.5KW and 7.5KW induction motors. (c) The equivalent circuit model for the stator winding structure in Chapter II.

The measurement results of the input impedances are shown in Fig. 4-2, and the specification of each tested motor is shown in Table 4-1. The characteristic of the input impedance can be investigated through the per-unit-length (PUL) equivalent model, which is shown in Fig. 4-2 (c). The input impedance can be divided into three frequency ranges with consideration of the indicated resonances in Fig. 4-2. The frequency regions and resonances are defined for the measurement result of 5.5kW motor. Corresponding to the equivalent circuit model, the most dominant element of the input impedance in the frequency region 1 is the winding-to-frame capacitances (C_{wf-lf}, C_{wf-mf} and C_{wf-hf}). After resonance 2, the interwinding capacitance (C_{iw}) and the mid-frequency winding-to-frame capacitance (C_{wf-mf}) become the effective parameters of the input impedance. In the region C after resonance 3, only the influence of the high-frequency inductance (L_{hf}) is observed at the input impedance.

At the high-frequency resonance 3 having the lowest value of the input impedance, the CM current can be maximized. Resonance 3 is determined by the capacitively decreasing impedance of the region B and the inductively increasing impedance of the region C, and it means that C_{iw}, C_{wf-mf}, and L_{hf} are the most effective elements for the resonance 3. To investigate L_{hf} element, an experiment is performed as shown in Fig. 4-3. A winding structure with sufficient number of turns is constructed and measured by two ports network as shown in the Fig. 4-3 (a), where the external line is the conductor wire that does not affect to consist of the winding turns. From the experimental results shown in Fig. 4-3 (b), the longer the external line shows more the inductance effect at the high-frequencies. Therefore, L_{hf} for the input impedance of the ac motor can be defined by the influence of the external line. The external line in the ac motor is defined not only as a cable connecting the motor and other devices, but also as the additional winding line above the end-winding for the neutral point connection and phase line terminals, which are not involved to compose the winding turns, as shown in Fig. 4-3 (c).

The comparison of the results with and without the rotor is shown in Fig. 4-4. The impedance characteristics are almost same regardless of the presence or absence of the rotor in the entire frequency range. Only the magnitude of the impedance at the resonances is slightly different around 100 KHz. From these results, we can know that most dominant factor affecting the input impedance of the ac motor is the winding structures in the stator. In addition, the high-frequency characteristic of the input impedance is not affected by the operating state. In the high-frequency, the eddy currents are induced in the stator and rotor structure. Since the eddy currents confine the rotor flux to the air gap, the flux cannot be transferred to the stator winding structure [23, 45]. Therefore, to change the input impedance of the ac motor, the winding structure should be designed effectively.
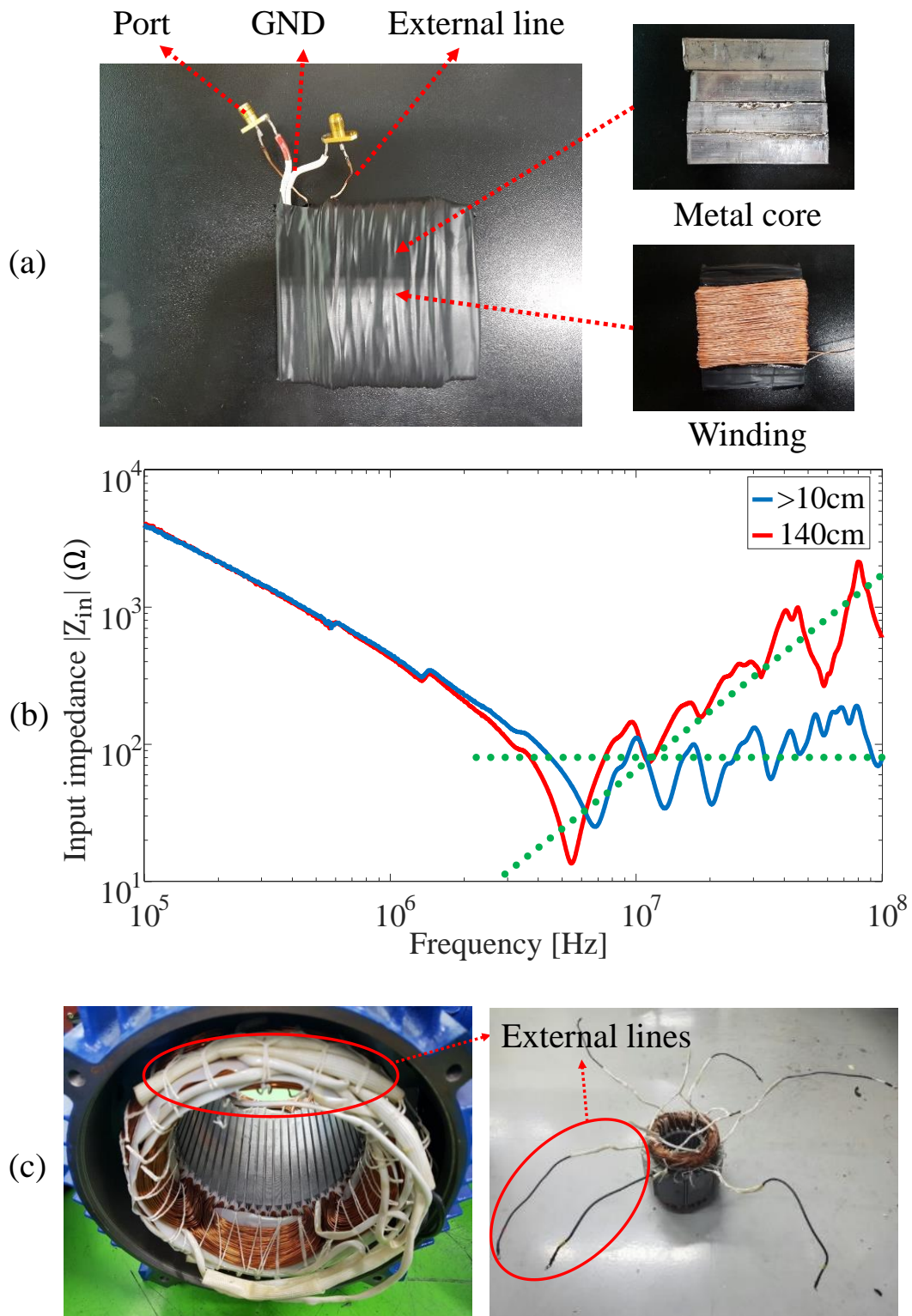
Fig. 4-3. (a) Experimental setup to determine the effect of external windings. (b) Measurement results of the input impedances for the winding structure. (c) The external lines to connect the phase lines in ac motor.

3.7KW motor

5.5KW motor
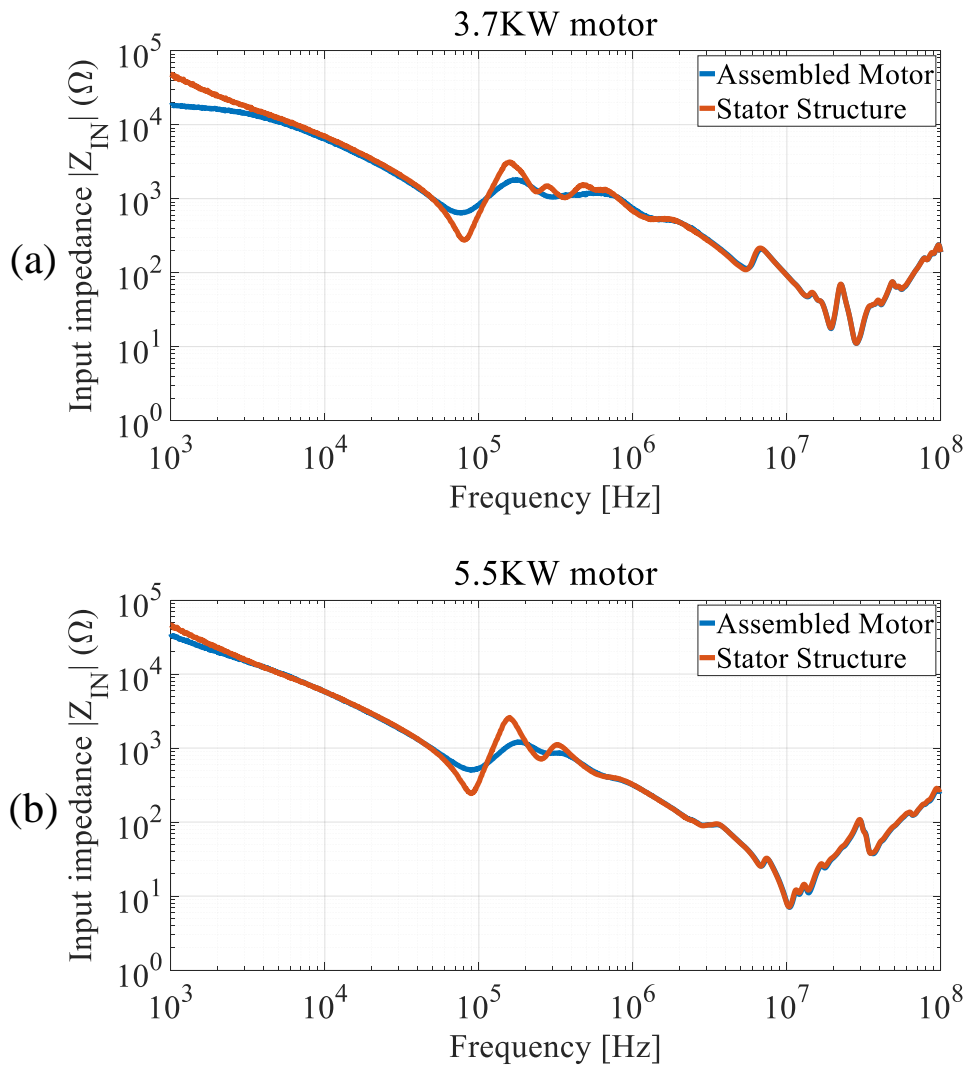
Fig. 4-4.   The measured result of the input impedances with and without the rotor in the ac motor.

In summary, the most important parameters of the winding structure to change the input impedance are C_{wf}, C_{iw} and L_{hf}. The low value of C_{wf} can increase the input impedance in the region A. Low C_{wf} and C_{iw} can produce the high impedance for the region B. The resonance 3 can be moved to higher frequency by lower values of C_{iw} and L_{hf}. In addition, to predict characteristics of these coupling parameters, the EM field analysis for the winding structure is required.

4.3. Prediction Method of the Input Impedance Characteristic

4.3.1. Electromagnetic Field Simulation for the Stator Winding Structure

In this section, an extraction method of the input impedance of the winding structure is introduced based on the network parameter analysis. To construct the network of the whole winding structure, an EM field calculation including all the conductors should be performed. However, modeling of the full-winding structure in the 3-dimension is difficult because the windings usually have tens or hundreds of turns. Moreover, the EM simulation requires huge computational cost due to the complicated motor winding structure and a lot of excitation conditions for the conductors.

To enable the EM field simulation for the complicated motor winding structure, the tested induction motor structure in the previous section is divided into several parts in 2-dimensional model instead of calculating 3-dimensional full structure model in Ansys 2D Extractor. The cross sections of single slot-winding structure and single end-winding structure are modeled as shown in Fig. 4-5 (a) and (b). The external line for the phase terminals and neutral point is modeled as shown in Fig. 4-5 (c). The EM field calculation for RL matrices and GC matrices are carried out separately for each model due to the different EM ground conditions. For the CG calculation, the electrical ground is set including core and frame structure to retain the electrical continuity for the conductivity. Whereas the EM ground is set for only the frame structure to consider the high-permeability material of the core structure for the RL calculation.

In addition, the EM field simulations are implemented by dividing into several frequency areas to analyze the EM field correctly over the wide frequency (1KHz~100MHz), because different mesh methods depending on the frequencies should be applied as shown in Fig. 4-6. Otherwise, if same mashes are used for the entire frequency region, the EM field is not calculated sufficiently for certain frequency ranges and the calculation shows incorrect results.

The matrices of $RLGC$ for all the conductors of winding structure can be extracted as the result of the EM field simulation. Then, the multi-port network parameter matrix for each model part can be obtained by converting the extracted $RLGC$ matrices with considering their lengths through transmission line method.
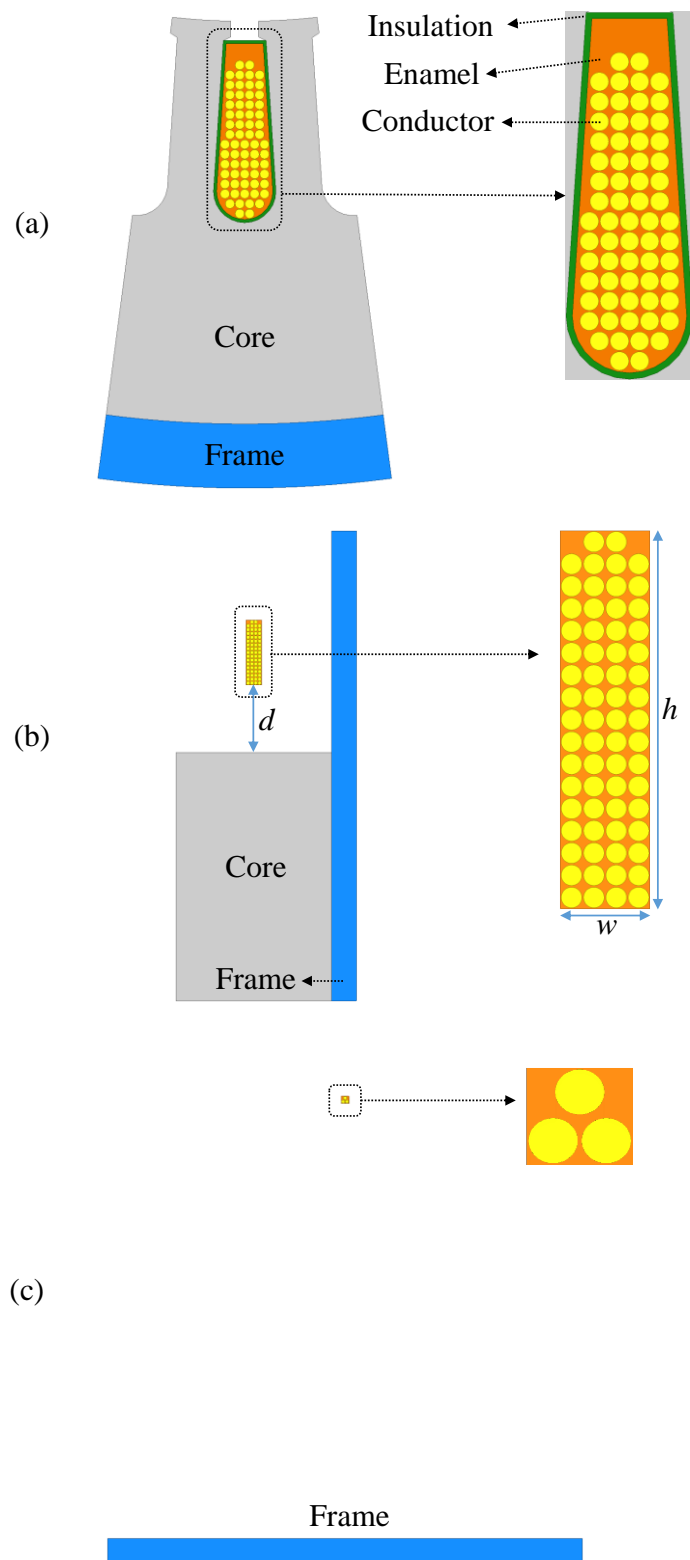
Fig. 4-5. The two-dimensional models for EM field calculation. (a) Single slot-winding structure. (b) Single end-winding structure. (c) External line structure.

(a)

(b)
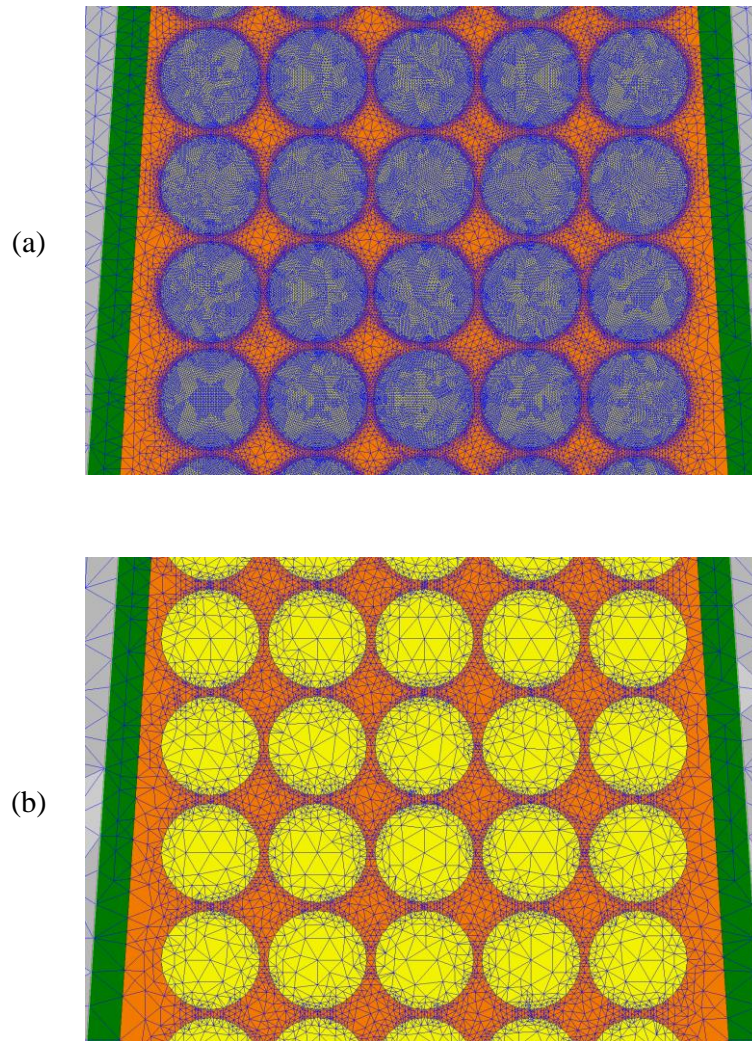
Fig. 4-6. The meshes to calculate the EM field of two-dimensional structure models. (a) The meshes with the 10kHz solution frequency. (b) The meshes with the 100MHz solution frequency.

4.3.2. Extraction of the Multi-Port Network Parameters for the Entire Phase Winding Structure

The network parameters of the slot-winding structure for 3.7KW motor is composed of 132 ports as shown in Fig. 4-7. The converted transmission (ABCD) matrix ($\mathbf{A_s}$) of the slot-winding network parameter ($\mathbf{NET_s}$) can be extracted as follow:

$$
\mathbf{NET_s} = \mathbf{A_s}
= \begin{bmatrix}
A_{1,1} & \cdots & A_{1,n} & A_{1,n+1} & \cdots & A_{1,2n} \\
\vdots & \ddots & \vdots & \vdots & \ddots & \vdots \\
A_{n,1} & \cdots & A_{n,n} & A_{n,n+1} & \cdots & A_{n,2n} \\
A_{n+1,1} & \cdots & A_{n+1,n} & A_{n+1,1+1} & \cdots & A_{n+1,2n} \\
\vdots & \ddots & \vdots & \vdots & \ddots & \vdots \\
A_{2n,1} & \cdots & A_{2n,n} & A_{2n,n+1} & \cdots & A_{2n,2n}
\end{bmatrix}
= \begin{bmatrix} \mathbf{M_{11}} & \mathbf{M_{12}} \\ \mathbf{M_{21}} & \mathbf{M_{22}} \end{bmatrix}_s
\tag{4.1}
$$

where n is the number of conductors in the slot, and s means slot-winding structure. $\mathbf{M_{11}}$, $\mathbf{M_{12}}$, $\mathbf{M_{21}}$ and $\mathbf{M_{22}}$ are sub-matrices of $\mathbf{A_s}$. Similarly, the transmission matrix of the end-winding structure ($\mathbf{A_e}$), which has same number of ports with the slot-winding structure, is obtained. The network of the single-winding can be constructed as shown in Fig. 4-8. The single-winding network parameters without return paths for the turn connection ($\mathbf{NET_{sw'}}$), which is marked part in the red dot box of Fig. 4-8, is extracted by product of the single-winding and end-winding network matrices as follow:

$$
\mathbf{NET_{sw'}} = \begin{bmatrix} \mathbf{M_{11}} & \mathbf{M_{12}} \\ \mathbf{M_{21}} & \mathbf{M_{22}} \end{bmatrix}_s \cdot \begin{bmatrix} \mathbf{M_{11}} & \mathbf{M_{12}} \\ \mathbf{M_{21}} & \mathbf{M_{22}} \end{bmatrix}_e \cdot \begin{bmatrix} \mathbf{M_{22}} & \mathbf{M_{21}} \\ \mathbf{M_{12}} & \mathbf{M_{11}} \end{bmatrix}_s \cdot \begin{bmatrix} \mathbf{M_{22}} & \mathbf{M_{21}} \\ \mathbf{M_{12}} & \mathbf{M_{11}} \end{bmatrix}_e
\tag{4.2}
$$

For return paths of the turns, the ports (P) are connected as follow:

$$
\begin{bmatrix} P_{n+1} \\ \vdots \\ P_{2n+N_{pcd}} \end{bmatrix}_{sw'} = \begin{bmatrix} P_{N_{pcd}+1} \\ \vdots \\ P_n \end{bmatrix}_{sw'}
\tag{4.3}
$$

where N_{pcd} is the number of parallel conductors of the motor. The ports that are not involved in the turn configuration can be defined the terminal ports of the single-winding as follow:

$$\begin{bmatrix} P_1 \\ \vdots \\ P_N \end{bmatrix}_{\mathbf{sw}} = \begin{bmatrix} P_{n+1} \\ \vdots \\ P_{N_{pcd}} \\ P_{2n-N_{pcd}+1} \\ \vdots \\ P_{2n} \end{bmatrix}_{\mathbf{sw}}. \tag{4.4}$$

In the case of 3.7KW motor, the calculated network parameter of the single-winding structure has six-ports because the winding consists of three parallel conductors.

Finally, the input impedance characteristics of the entire phase line can be obtained by the connection of the networks as shown in Fig. 4-9. The transmission matrix of the winding-line can be calculated by product of the single-winding and external-line networks as follow:

$$\mathbf{A}_{\mathbf{winding-line}} = \mathbf{A}_{\mathbf{el}} \times \mathbf{A}_{\mathbf{sw}} \times \cdots \times \mathbf{A}_{\mathbf{sw}} \times \mathbf{A}_{\mathbf{el}} \tag{4.5}$$

where the number of the products of $\mathbf{A_{sw}}$ is determined from the value dividing the winding number of the motor by the number of parallel circuits. The network parameters for the entire phase line can be extracted as following calculation of the admittance parameter matrices:

$$\mathbf{NET}_{\mathbf{phase}} \rightarrow \mathbf{Y}_{\mathbf{phase}} = \mathbf{Y}_{\mathbf{winding-line}} + \cdots + \mathbf{Y}_{\mathbf{winding-line}} \tag{4.6}$$

where the number of adding $\mathbf{Y_{winding-line}}$ is defined by the number of parallel circuits in the motor.

The calculated input impedances of the phase line for the tested ac motors are shown in Fig. 4-10 as compared with the measured ones. As shown in the results, the calculated input impedances of all three motors show close matches with the measurement results over the wide-frequency. Moreover, the calculated results follow the trends of the variation behaviors in 100KHz~1MHz region reasonably. The high-frequency antiresonance is also captured properly. Therefore, the comparison result verifies that the proposed method can be used to predict the wideband motor characteristics from user's design parameters during motor design stage.
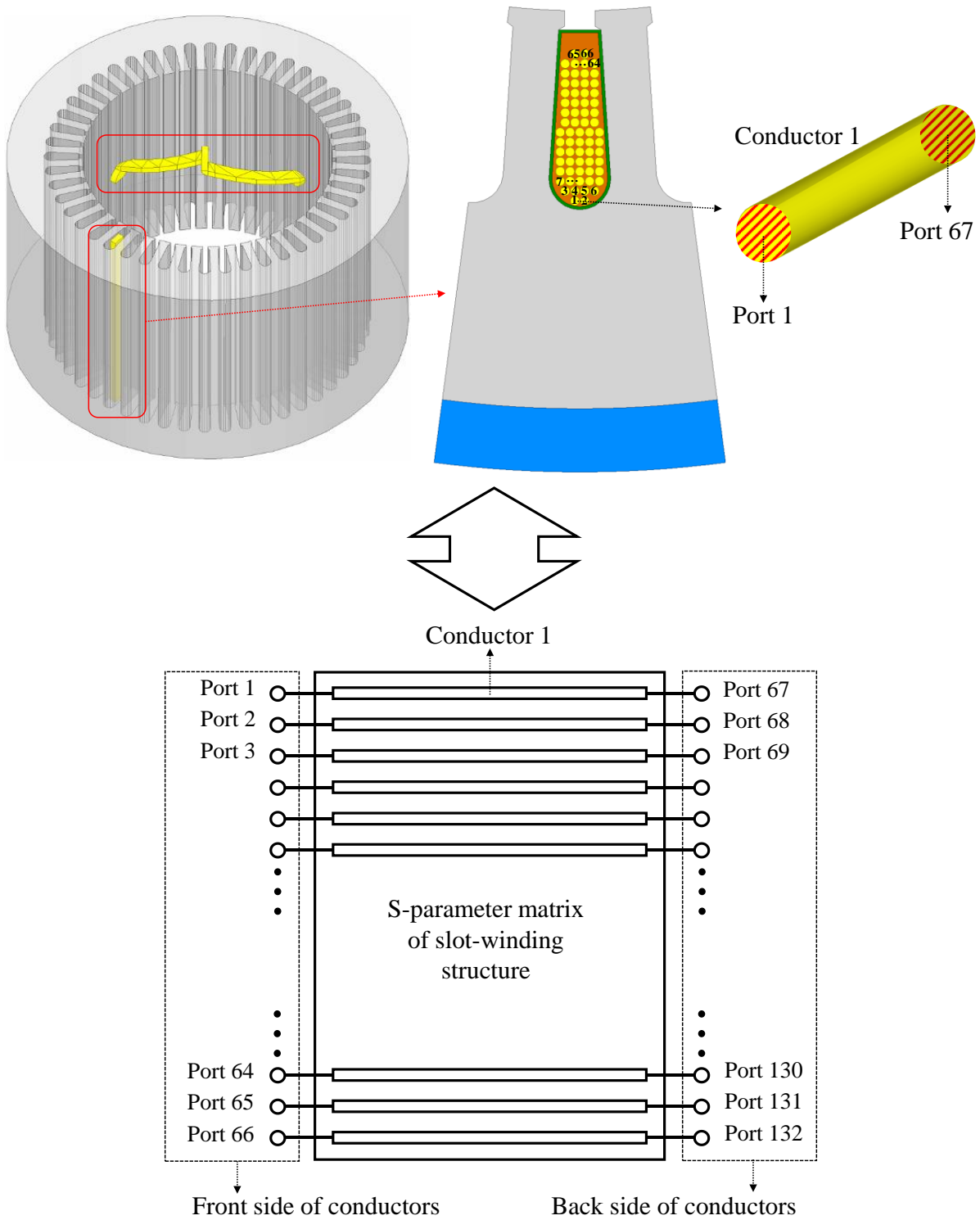
Fig. 4-7.   The multi-port network corresponding to the simulated single slot-winding structure.
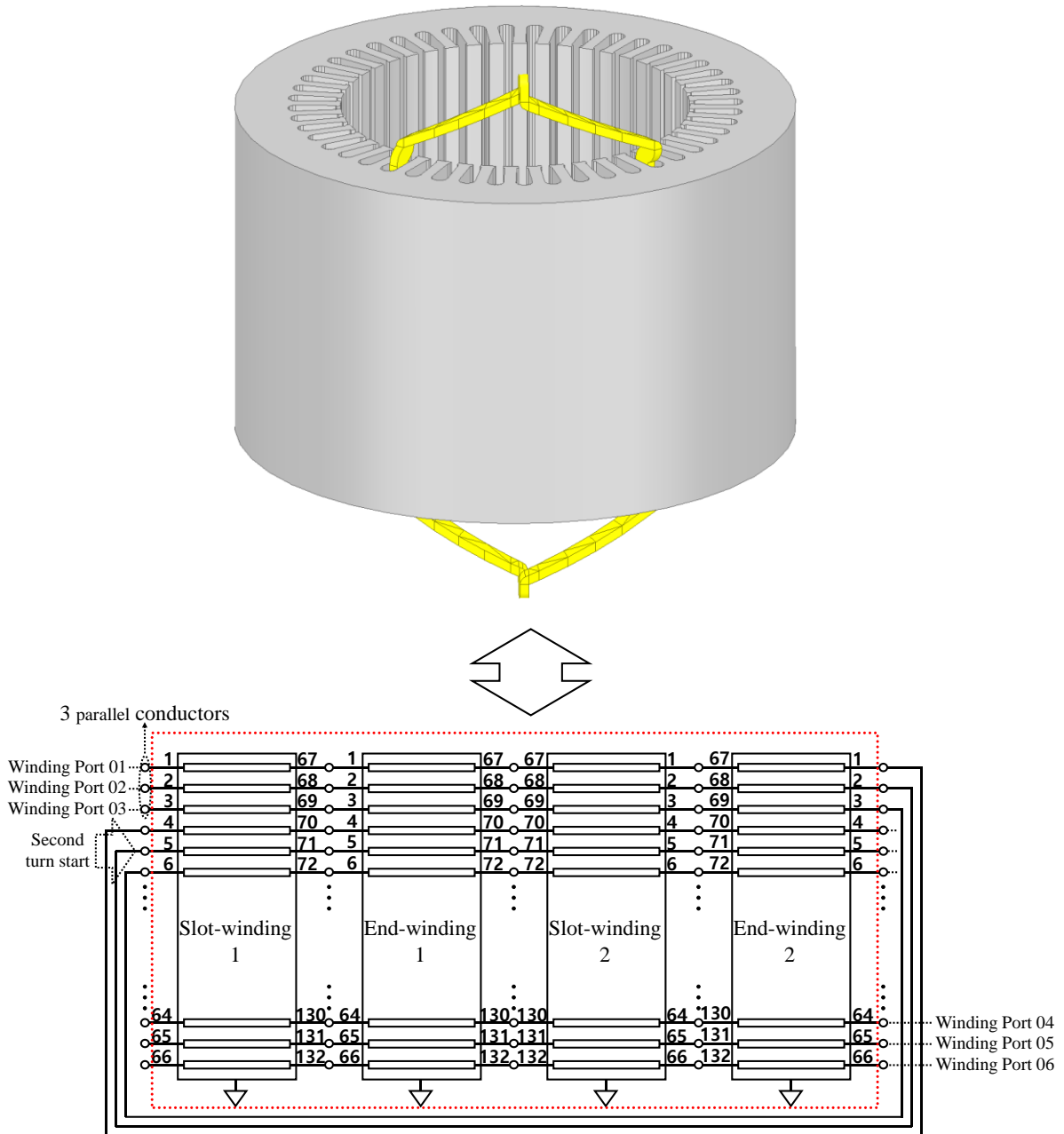
Fig. 4-8. Configuration of the multi-port network for the single-winding structure.
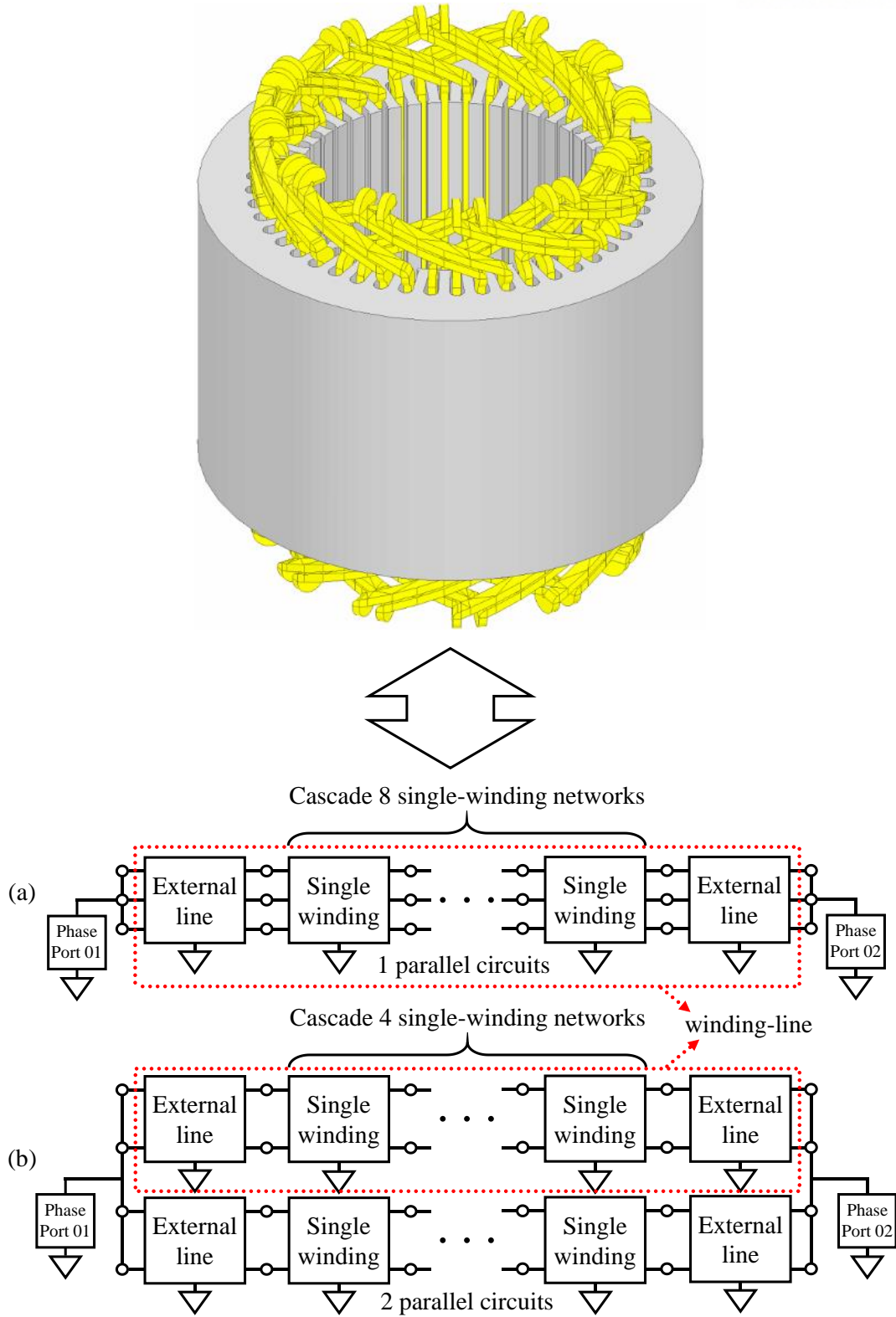
Fig. 4-9. Configuration of two-port network for the entire phase line of the ac motor. (a) 3.7kW induction motor. (b) 5.5kW induction motor.
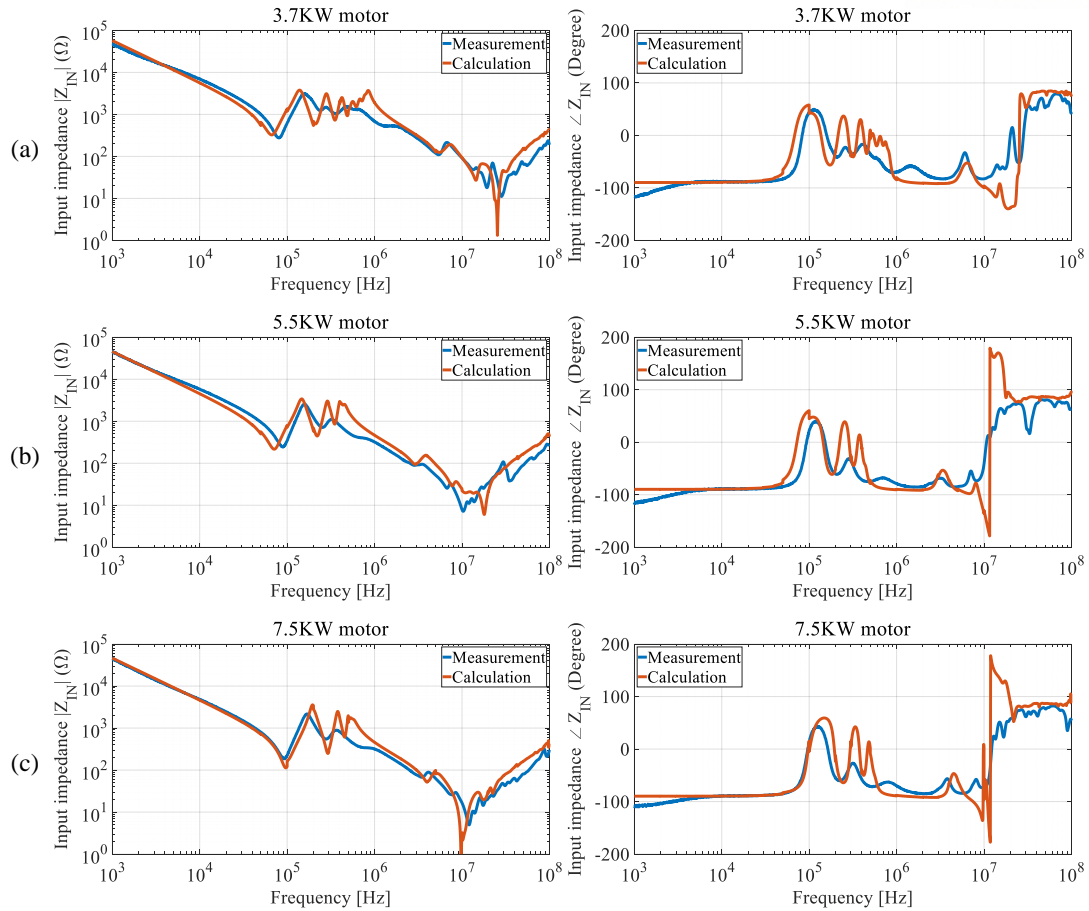
Fig. 4-10.   Comparison of the input impedances between measurement and calculation for the tested ac motors. (a) 3.7KW ac motor. (b) 5.5KW ac motor. (c) 7.5KW ac motor.

4.4.   EMC-Aware Motor Design Method by Parametric Analysis

4.4.1. Input Impedance Extraction for the different Motor Models by Automated Design Code

In this section, an EMC-aware motor design method is proposed. The ac motors are modeled for the different design parameters, and the characteristics of the input impedances of all the designed motors are investigated by applying the presented input impedance extraction method in the previous section. To estimate the wideband characteristics for the various design cases, an automated design code is developed. The flow chart of the automated design code is shown in Fig. 4-11.
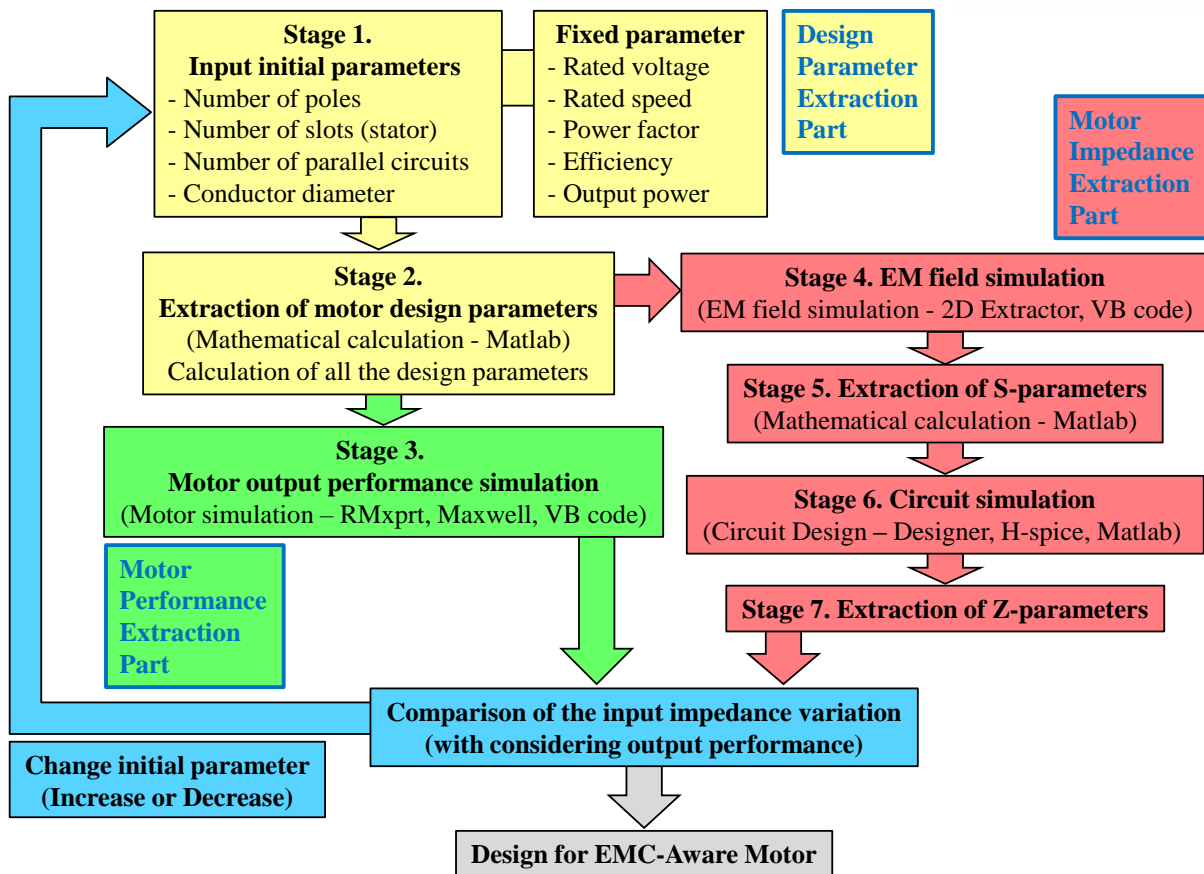
Fig. 4-11. The flowchart of the automated design code to design an EMC-aware ac motor by changes of the design parameters.

The automated design conde has three parts. In the design parameter part, all the design parameters are treated as variables to be calculated automatically with considering the geometric, structural, and electromagnetic parameters. In the motor performance extraction part, the general motor output performances are calculated automatically in the motor simulation. In the motor impedance extraction part, the EM field calculation for the designed motor models is conducted to extract the input impedance characteristics of phase windings. The design code performs the calculation with several return path to compare the input impedance and output performance between the designed models.

In Stage 1, the initial input parameters that user should consider in the first stage of motor design are decided. They are set as number of poles, number of slots, number of parallel circuits, and conductor diameter for number of parallel conductors in this research. The fixed parameters are defined to compare the characteristics of the input impedances when the designed motors have same output performances. They are set as rated power, rated speed, rated voltage, efficiency, power factor.

End-winding arc length (l_{ea})

(a)

Radius to slot center (r_{sc})

End-winding arc angle (θ_{ea})

(b)

h_2 h_1

h_2

h_1

l_{side}

EAL

$P(0,0,0)$
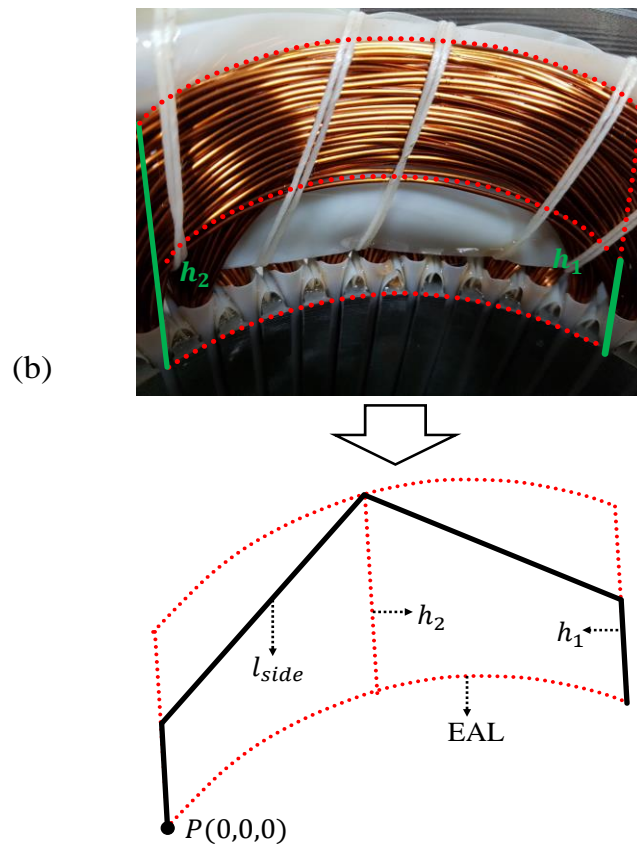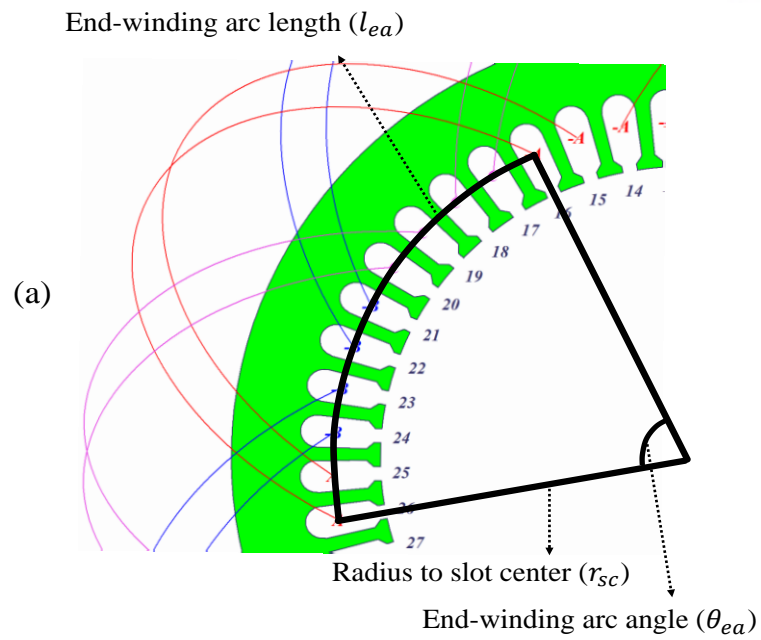
Fig. 4-12. Calculation of the generalized end-winding length to apply any design parameter changes. (a) Definition of the end-winding arc length and angle. (b) The model of the end-winding to calculate its length.

From the defined input initial parameters, the specific motor design parameters, such as the dimensions of the core, number of turns, are calculated in Stage 2 [46]. All design parameters are treated as variables to accommodate any motor design type. To calculate the network parameters as transmission line, the length of the end-winding should be defined as a design parameter as shown in Fig. 4-12. The generalized calculation for the average length of the end-winding is as follows:

$$l_{side} = \sqrt{\left(-r_{sc}sin(\theta_{ea})\right)^2 + \left(r_{sc}\left(1 - cos(\theta_{ea})\right)\right)^2 + (h_2 - h_1)^2} \tag{4.7}$$

$$l_{end-winding} = 2(l_{side} + h_1) \tag{4.8}$$
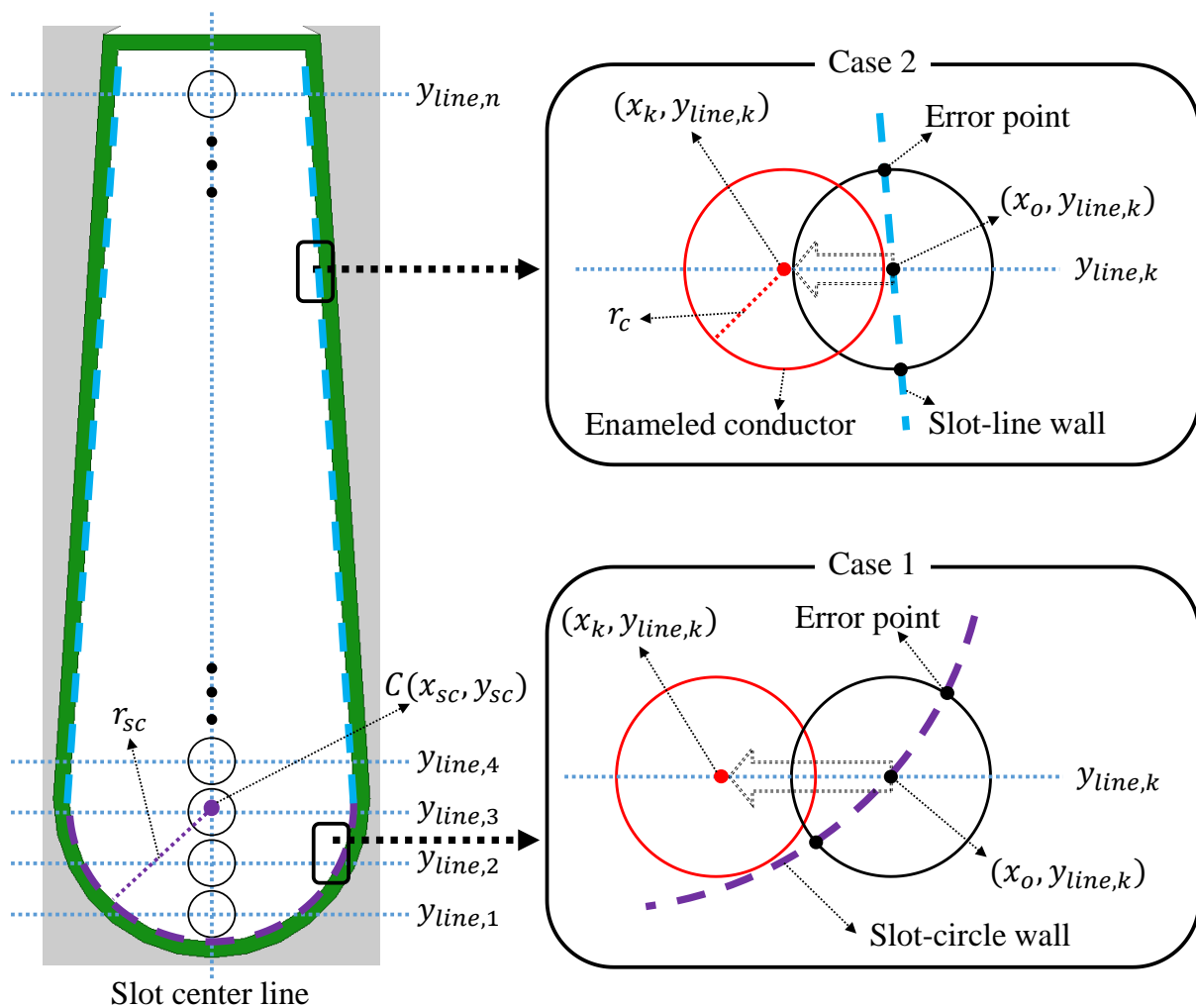
Fig. 4-13. The modeling of the slot-winding structure for automated calculation to apply any design parameter changes.

where the end-winding height h_1 and h_2 should be decided by user with considering the size of motor. All the unknown parameters should be estimated from the other design parameters in Stage 2 to be possible the automated calculation.

In Stage 3, the general motor output performances of the designed motors are calculated by the motor simulation tools (Ansys RMxprt and Ansys Maxwell) using the extracted the design parameters in the previous stages. The general important characteristic of the motor output performance, such as core loss and torque ripple, are calculated to consider together with the EMC motor design.

The EM field simulations for the modeled motor structures are conducted to extract the input impedance in Stage 4. To be applicable to any motor design, the automation of the conductor arrangement for each model is required. The arrangement method of the conductors for the slot-winding structure is shown in Fig. 4-13. The circles represent the enameled conductors, and $y_{line,k}$ is the possible y-axis coordinates of the center of the conductors to be stacked conductors. The locations of the conductors are defined by the following relations of the line and circle functions:

$$\text{Case 1:} \quad f_{sc}(x_{sc},\ y_{sc},\ r_{sc}) = f_c(x_0 - \alpha,\ y_{line,k},\ r_c) \tag{4.9}$$

$$\text{Case 2:} \quad f_{sl}(x_{sl},\ y_{sl}) = f_c(x_0 - \alpha,\ y_{line,k},\ r_c) \tag{4.10}$$

where the subscript sc, sl and c indicate slot-circle wall, slot-line wall and conductor, respectively. Therefore, (4.9) is an equation of intersections for two circles, and (4.10) is an equation of intersections for a circle and a straight line. α is defined to be much smaller value than the diameter of conductor. By increasing the value of α, the conductor is moved gradually to the slot inner direction on the line $y_{line,k}$ until the function (4.9) and (4.10) does not have solution. The number of conductors that can be on line $y_{line,k}$ are calculated, where the distance between the leftmost and rightmost conductor centers should be less than $2x_k$. The conductors of the end-winding structure is also automatically modeled by defining the boundaries which is determined from the variables d, h and w in Fig. 4-5 (b).

In Stage 5, The calculated large $RLGC$ data from the EM field simulation is converted to s-parameter data. Then, the s-parameter data are used to extract the winding and the phase networks by the circuit simulation in Stage 6. Since the extracted S-parameters have a lot of ports, connecting the ports to construct the entire winding network is difficult. Therefore, all the ports are connected by netlist and node naming without wiring by following function:

$$P_n = f(N_w,\ N_{pcc},\ N_{pcd}) \tag{4.11}$$

where, P_n, N_w, N_{pcc} and N_{pcd} mean the netlist of port, number of windings, number of parallel circuits and number of parallel conductors for the designed motor respectively. The calculation of the winding

network is implemented in the circuit simulation automatically based on H-spice code.

The extracted input impedances of the designed 5.5KW motors for the various design parameters is shown in Fig. 4-14, and important design parameters for the designed motors are shown in Table 4-2. The parameters in the gray box of Table 4-2 are the main design parameters to investigate the impedance characteristic changes, and the other design parameters are used to obtain same output performance or are extracted as the resultant parameters from calculation. The parameter, total slot wall area, is calculated to estimate the effect of C_{wf}.

When the number of poles is increased, the terminal input impedance is decreased in the region A as shown in Fig. 4-14 (a) because C_{wf} is increased as the slot wall area increased. In the frequency region B where the effect of C_{iw} is involved, the input impedance is almost same regardless of the change of number of poles. As the number of poles increases, the number of conductors in a slot is decrease, so C_{iw} can be expected to decrease. However, the lengths of entire phase line including end-winding length in a series are increased to about 137, 180 and 222 in meter, respectively, therefore C_{iw} is not changed much. As the number of slots increases, C_{wf} is increased, therefore the input impedance decreases in the region A as shown in Fig. 4-14 (b). On the other hand, the input impedance increases in the region B because C_{iw} becomes smaller as the number of conductors becomes smaller. As shown in Fig. 4-14 (c), C_{iw} increases as the number of conductors increases, therefore the input impedance decreases only in the region B over the entire frequency range. The input impedance decreases significantly in the region B when the parallel circuit increases as shown in the result of Fig. 4-14 (d). Interestingly, even though the number of conductors and total slot wall area are exactly same by reducing the number of parallel conductors 2 to 1 when the number of parallel circuits doubles from 2 to 4, the results of the input impedance show a large difference. This means that even if the stator structure and the amount of used conductor are the same in the motor design, the input impedance can vary due to the circuit connection of the windings.

The calculated results of the core loss and torque ripple in the motor performance simulation of Stage 3 are shown in Fig. 4-15. The characteristic relations of input impedance, core loss and torque ripple by the variations of the design parameter are summarized in shown in Table 4-3. As the number of slots is increased, the output performance of the ac motor is improved, and the input impedance of region B is also slightly increased, which may improve the EMC characteristic. However, it is difficult to assure that the EMC characteristic can be improved because the input impedance in region A is significantly reduced.
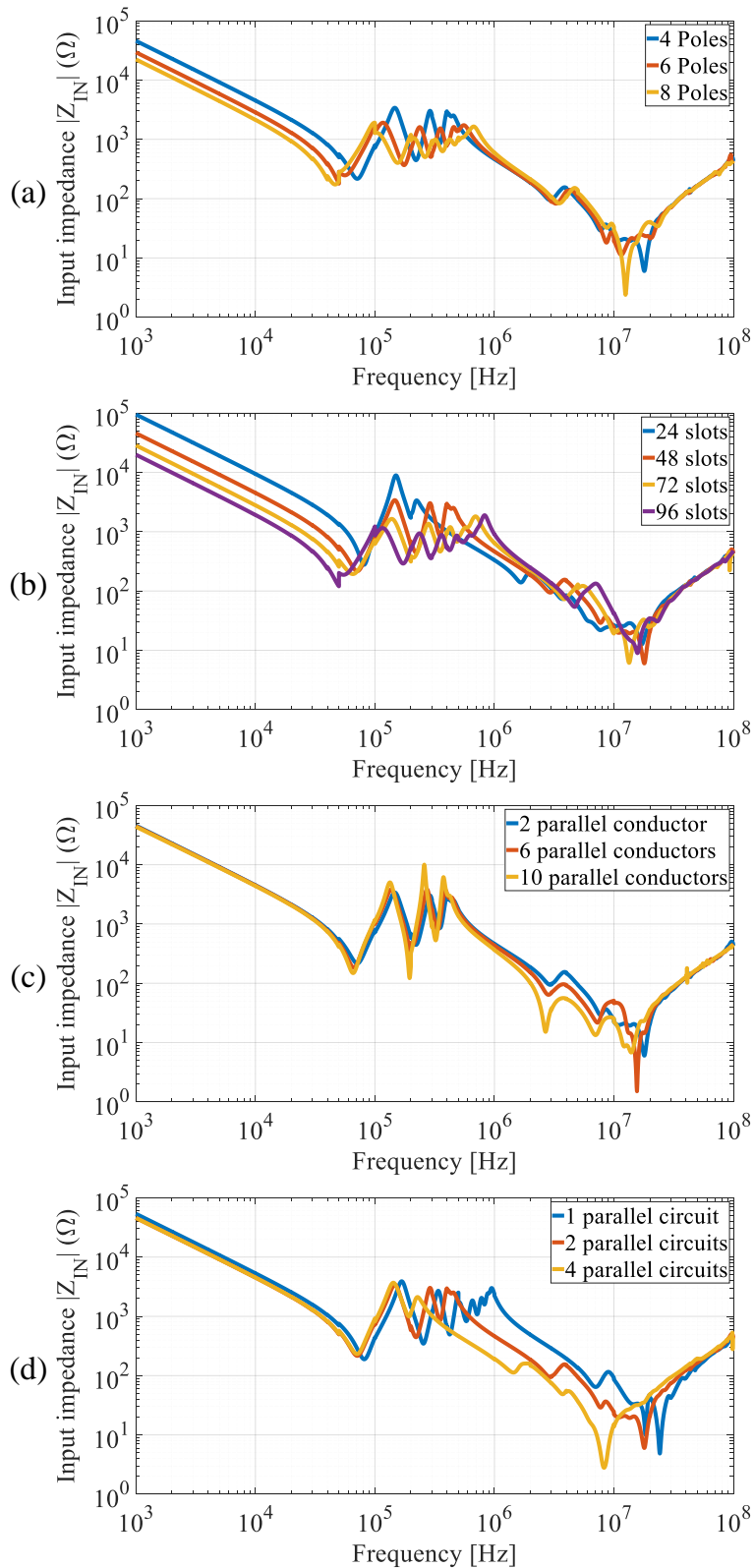
Fig. 4-14. Comparison of the results of the input impedances extracted by the variation of the design parameters. (a) Poles. (b) Slots. (c) Parallel conductors. (d) Parallel circuits.

87
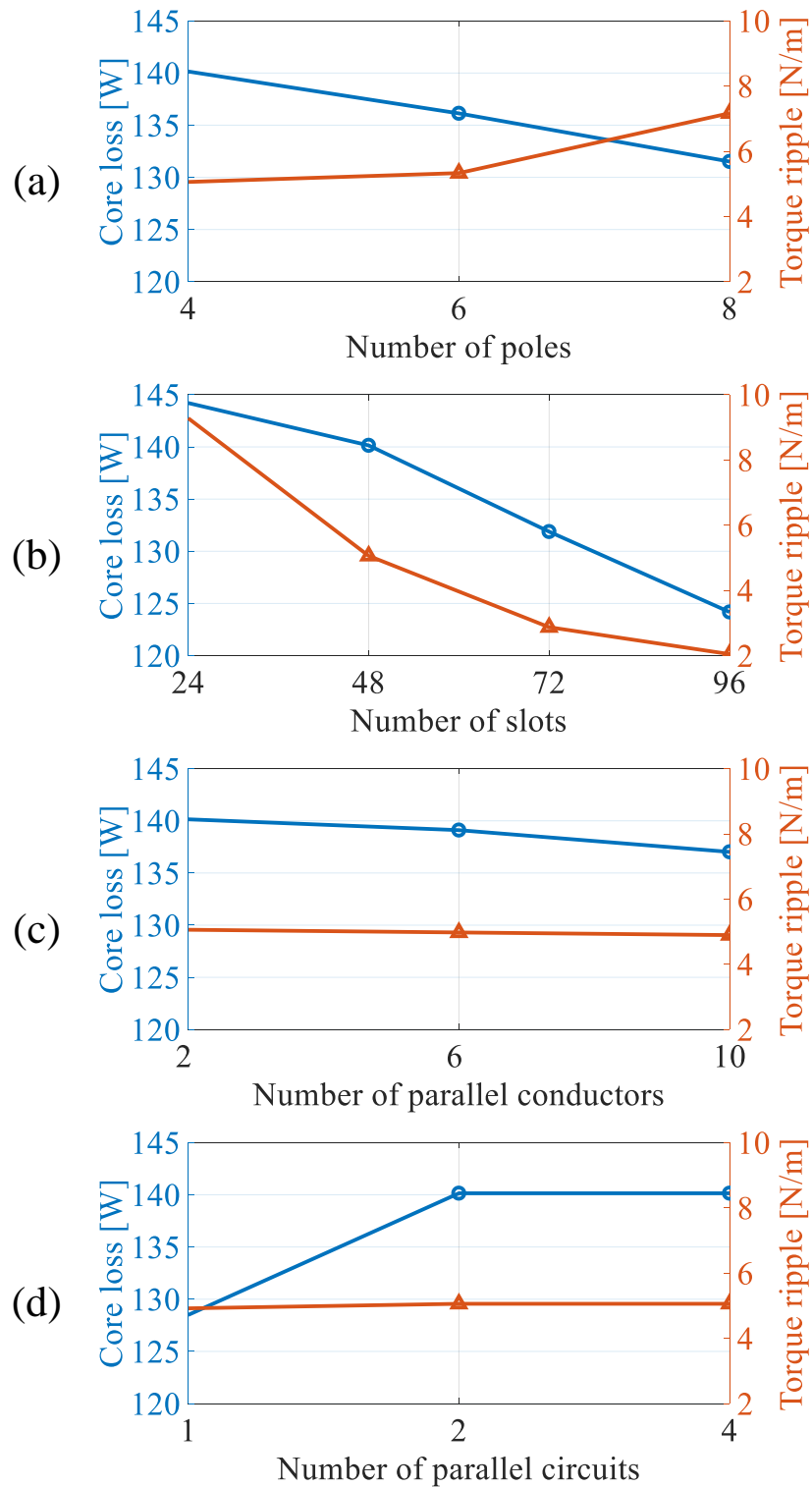
Fig. 4-15. The changes of the calculated core losses and torque ripples by variation of the design parameters. (a) Poles. (b) Slots. (c) Parallel conductors. (d) Parallel circuits.

Table 4-2. Design parameters of the redesigned 5.5kw ac motors

Pole (Num.)	Slot (Num.)	Parallel conductor (Num.)	Parallel circuit (Num.)	Conductor per slot (Num.)	Conductor diameter (mm)	Total slot wall area (mm²)
4	48	2	2	70	0.85	211164
6	72	2	2	56	0.85	311410
8	96	2	2	48	0.85	410639
4	**24**	2	2	138	0.85	110486
4	**48**	2	2	70	0.85	211164
4	**72**	2	2	46	0.85	322584
4	**96**	2	2	36	0.85	480680
4	48	**2**	2	70	0.85	211164
4	48	**6**	2	210	0.43	190327
4	48	**10**	2	350	0.32	190662
4	48	3	**1**	51	0.85	169739
4	48	2	**2**	70	0.85	211164
4	48	1	**4**	70	0.85	211164

The design parameters that can be considered clearly for the EMC motor design are number of parallel conductors and number of parallel circuits. When the number of parallel conductors is changed, all other results are almost stable, and only the input impedance in the region B is affected. Therefore, the smaller number of parallel conductors is better for the EMC motor design without any changes of motor output performance. The smaller number of parallel circuits shows the strongly higher input impedance in region B, and less of core loss. Therefore, this design parameter can be an important parameter to design an EMC-aware ac motor.

Table 4-3. Change of the input impedance by the design parameters

Increasing parameter	Impedance region A	Impedance region B	Impedance region C	Core loss	Torque ripple
Poles	Decrease	Almost same	Almost same	Decrease	Increase
Slots	Strongly decrease	Increase	Almost same	Decrease	Decrease
Parallel conductors	Almost same	Decrease	Almost same	Almost same	Almost same
Parallel circuits	Almost same	Strongly decrease	Almost same	Increase	Almost same

4.4.2. Measurement of the Common-Mode Current in the Motor Drive System

To verify the motor EMC design method according to the motor parameters, several motors with different number of parallel circuits, which is one of dominant design parameter showing the change of the input impedance characteristic, are made as shown in Fig 4-16. The motors are rewound to change the number of parallel circuits, and they are made to have one, two and four parallel circuits for the 3.3KW and 5.5KW induction motors respectively. The measured results of the input impedances for the rewound motors through the VNA is shown in Fig. 4-17. Although the rewound motors do not have exactly same structure conditions with the designed motors in the previous section due to the used same stator cores in the experiment, the decreasing trend of the input impedance characteristic is well matched over the entire frequency range.
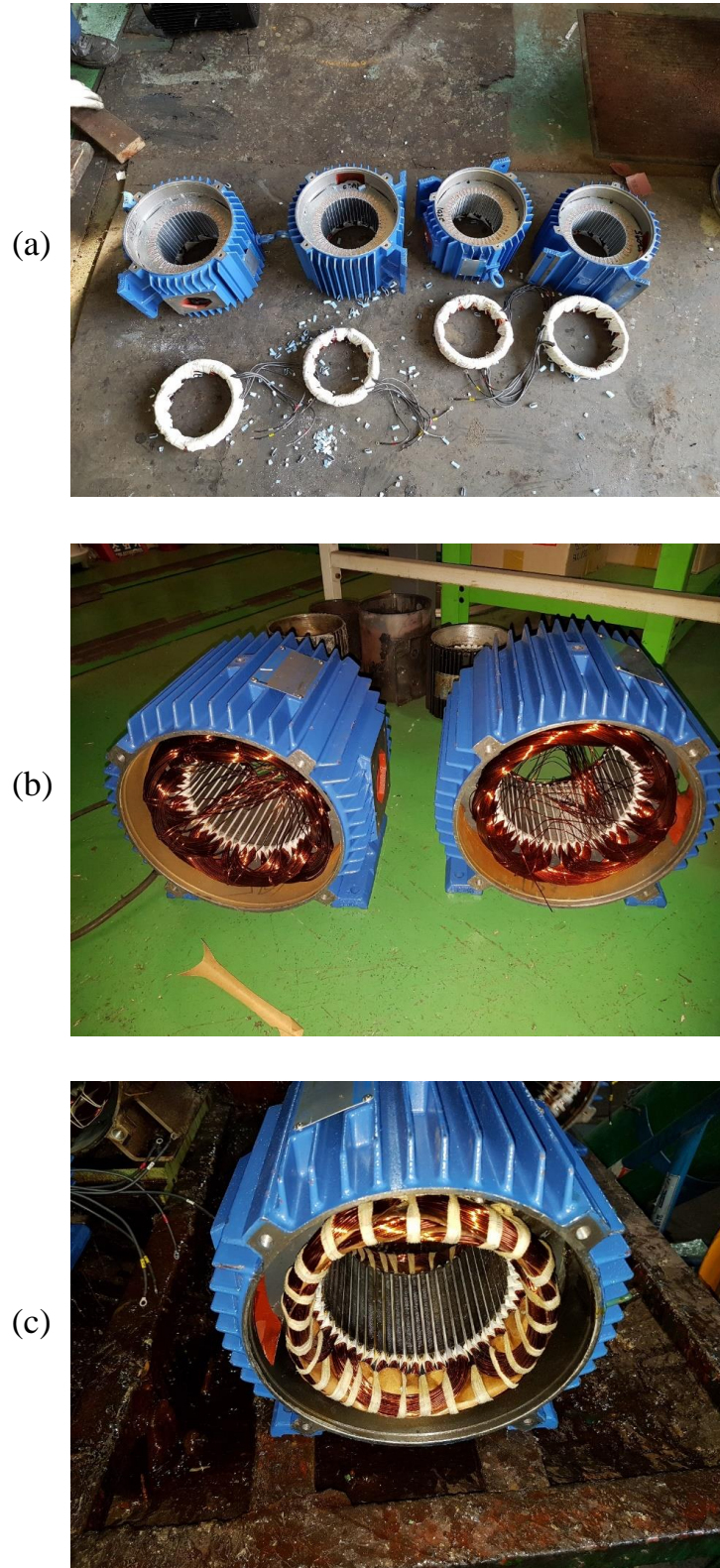
Fig. 4-16. Manufacture of the induction motors to change the number of parallel circuits. (a) removal of the original winding. (b) Rewinding by design parameter. (c) Enamelling and fixing.
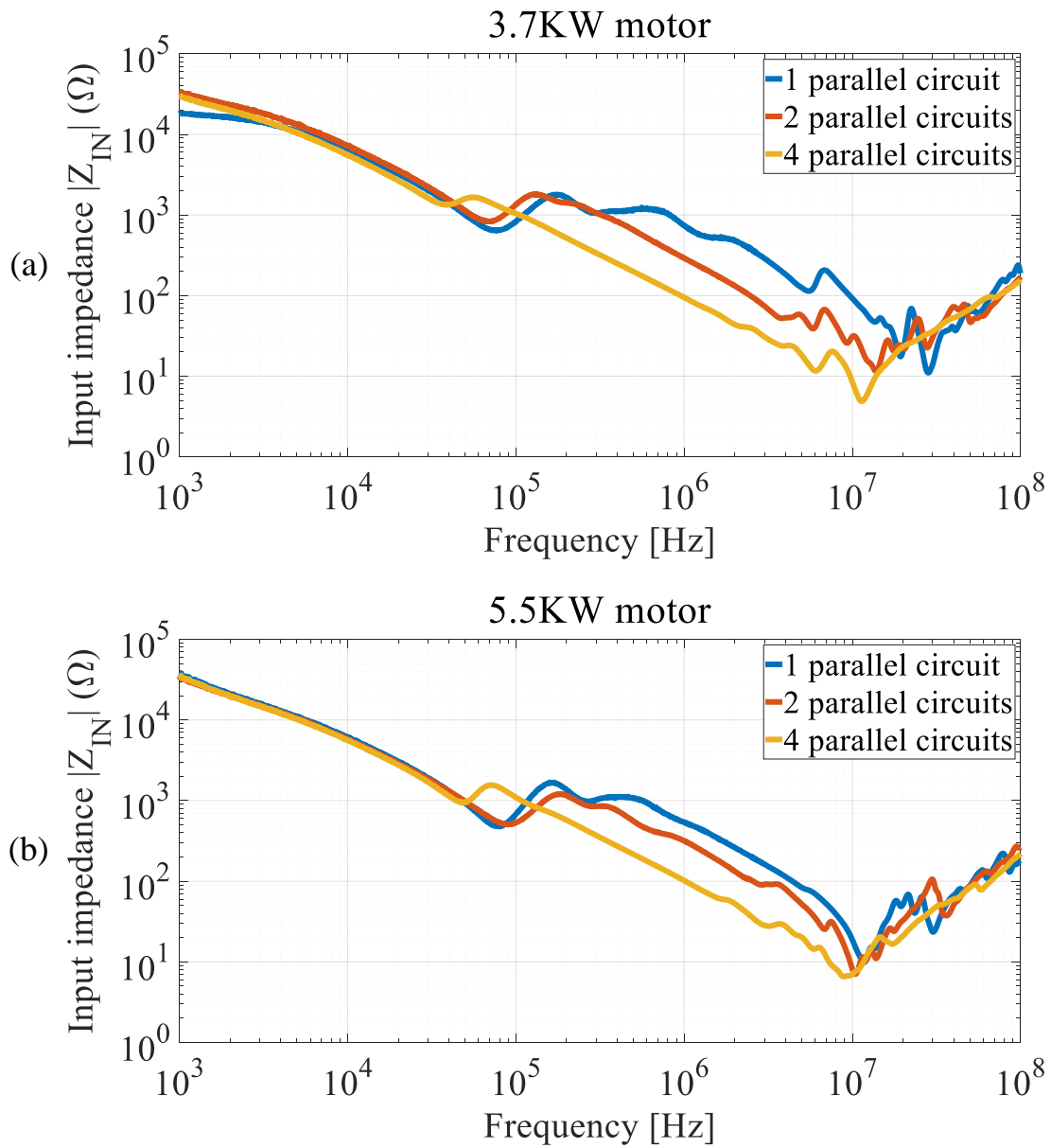
Fig. 4-17. Input impedance measurement results of the induction motors produced by different number of parallel circuits.
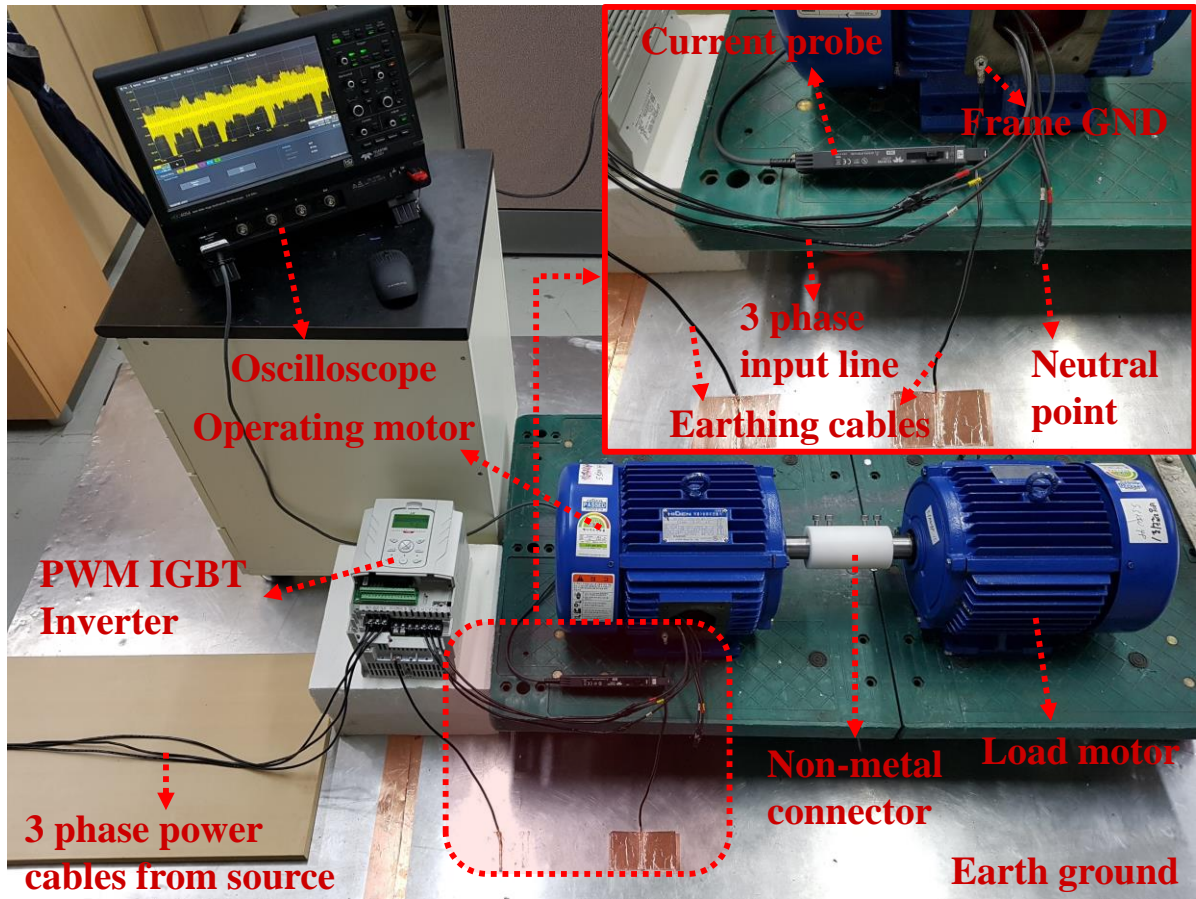
Fig. 4-18. Measurement setup to observe the CM current in the motor drive system.

In order to investigate the circulating CM current generated in the system during the motor operation, the experiment is conducted as shown in Fig. 4-18. Three-phase voltages of 380V from the power source is applied to the inverter (LSLV0075H100-4COFN) via the cables. The switching frequency of the inverter is set as 3kHz. The modulated three phase voltages are supplied from the inverter to the input terminals of the redesigned induction motor through the cables. Other motor is connected to the operating motor for the mechanical load with an insulated connector. Large and flat metal plate is installed on the floor for common earth ground. The frame of the motor and the enclosure of the inverter are grounded through the earthing cables to the metal plate ground. The CM current which is circulating in the motor drive system is measured by connecting a current probe (CP030) to the earthing cable of the motor frame when the motor is driving. The waveform of the CM current is observed by an oscilloscope (HDO4054A).
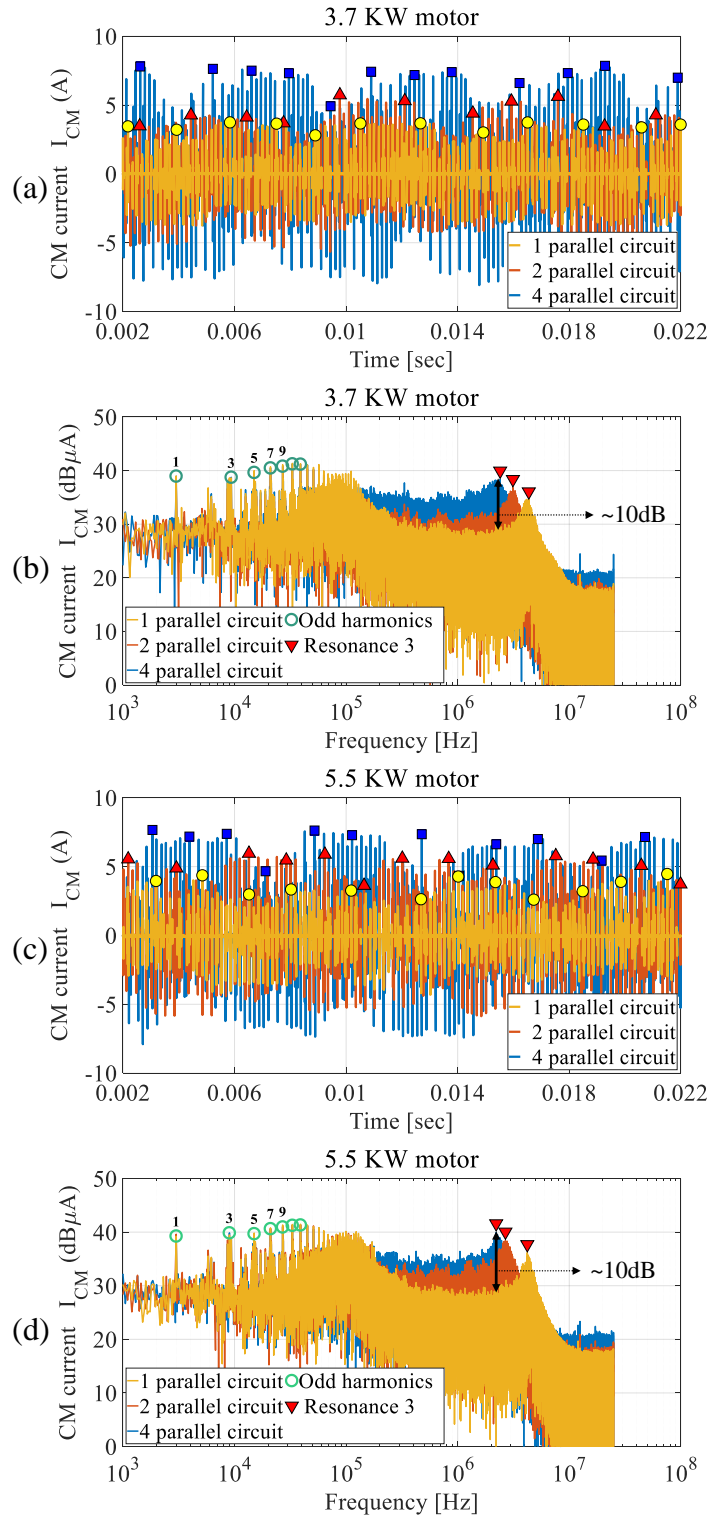
Fig. 4-19. The measurement results of the CM currents in the motor drive system by change of the number of the parallel circuits in the ac motors. (a) Measured result of the CM currents for 3.7KW ac motors. (b) Spectrum of the CM currents for 3.7KW ac motors. (c) Measured result of the CM currents for 5.5KW ac motors. (d) Spectrum of the CM currents for 5.5KW ac motors.

The measured results of the CM currents in the motor drive system are shown in Fig. 4-19. As the number of the parallel circuits decreases, the average CM current peaks of time domain decrease to 7 ~ 8A, 4 ~ 6A, and 3 ~ 4A, respectively, resulting in lower EMC performance. The results confirm that the higher the input impedance of the motor, the higher the EMC performance, in relation to the measured results of the impedance characteristics shown in Fig. 18. Moreover, the results of the CM current spectrum describe well the impedance characteristics of the motor. In the frequency region A, regardless of the number of the parallel circuits, the spectrum of the CM current appears largely at the odd harmonics of 3kHz. However, in the frequency region B, as the input impedance increases by decrease of the number of the parallel, the magnitude of the CM current spectrum becomes much smaller. The motor with 1 parallel circuit reduces the CM current up to about 10 dB in the region B, compared to the motor with 4 parallel circuits. Furthermore, the phenomenon, that the CM current becomes the largest at the resonance 3 where the input impedance is the smallest, also coincides. Comparing the results of Fig. 15 and Fig. 20, the frequencies at resonance 3 are slightly lower when the motor is driven, because the inductance component increases as long cables are connected in the system. Therefore, the high-frequency impedance slope in region C shifts to lower frequency. In summary, the results show that the lower number of parallel circuits in the motor can be strong against EMI due to the lower level of the CM current and the higher frequency of the resonance 3. In addition, the measurement results validate the EMC-aware motor design method using the design parameters.

4.5. Summary

In this chapter, an EMC design method for an ac motor by estimation of the input impedance of the phase winding was presented. The advantage of the proposed extraction method for the input impedance is that the accuracy is high, and it can be applied to any type of the winding structure including all the conductors. Moreover, without any complex modeling or computation, the input impedance characteristics can be extracted easily by general commercial EM field and circuit simulation tools. In addition, although the EMC design method for the ac motor was analyzed by the four design parameters (number of slots, poles, parallel conductors and parallel circuits), the characteristics of the input impedance for the other design parameters can be extracted through the generalized design procedure. Consequentially, the proposed methods can be used to design an EMC-aware ac motor for the wide frequency area with high accuracy.

Chapter V
Conclusion

5.1. Conclusion

In this thesis, the design method of the EMC aware ac motor is proposed by characterizing the input impedance of the winding structure. To predict the input impedance characteristic in the motor design stage, the EM field calculation method of the phase winding structure is developed by applying the multi-port network analysis. The wide frequency characteristics of the ac motor are investigated through the constructed equivalent circuit model.

The PUL equivalent circuit model for the phase winding structure is constructed by applying the transmission line theory. The characteristics of the lumped-elements in the PUL equivalent circuit model can be defined clearly by analysis of the extracted *RLGC* parameters. The input impedance of the equivalent circuit model shows close match with the measurement result. The proposed lumped-element PUL equivalent circuit model can be constructed much easier than the previous complicated distributed-parameter models. Moreover, the proposed equivalent circuit model describes accurately the physical meanings of the elements which was unclear in the previous measurement-based models through the analysis of *RLGC* parameters. Therefore, the proposed PUL equivalent circuit modeling method can easily and accurately extract the wide frequency characteristics of the ac motor winding structure.

To investigate all the impedance characteristics in the three-phase windings structure for the high-frequencies, the extraction method of the multi-port network parameters is developed by using the relation of the mixed-mode (CM and DM). The six-by-six network parameters of three-phase are extracted simply by using the two-port network data of mixed-mode under the symmetric structure assumption. Moreover, the simple T-equivalent circuit model which can distinguish the effect of phase-to-phase coupling is constructed by the extracted parameters from the mixed-mode conversion. In addition, the multi-network parameter extraction method is applied to investigate the effect of CM and DM on both end sides of the shaft structure. Since the structure of the ac motor is almost symmetric, the proposed method can be used to extract the impedance parameters for any part of the ac motor.

By applying the proposed equivalent circuit modeling method and the multi-port network parameter extraction method for the ac motor, the EMC-aware motor design method is studied. Through the analysis of the equivalent circuit elements, the structural elements that affect the input impedance of the ac motor are determined. Moreover, the EM field calculation method for the full winding structure including all the conductors is presented to predict the input impedance characteristics of the designed motor models.

By using the multi-port network parameters of the conductors of winding structure, the input impedance of the phase winding of the modeled ac motor is extracted. To investigate the variation of the input impedance by the changed design parameters, automated design and calculation code is developed. From the extracted input impedances of the designed motor models, the EMC-aware ac motor design method is presented with considering the output performance of the ac motor. Moreover, the prototype ac motors are made, and the CM currents are measured when the motors are operating in the drive system. The result shows the ac motor structure which have high input impedance can reduce the CM current about 10dB. Even though the considered design parameters are number of poles, number of slots, number of parallel conductors, and number of parallel circuits in this study, many other design parameters can also be considered to design EMC ac motor by using the proposed design method.

5.2. Future Work

The future work concerns the improvement and extension of the proposed methods which are proposed in this thesis. It can be divided into three parts as methodology, simulation, and measurement.

The methodology part includes the improvement of the equivalent circuit model and multi-port network parameter extraction method. As discussed in section 4.2, the windings are hardly affected by the rotor structure in the high-frequencies whether the motor is stationary or operating. Therefore, the elements of the proposed equivalent circuit model are independent of the rotor. However, to investigate the EMI characteristic of full ac motor structure, the circuit model of the rotor structure need to be added. For that, the modeling method for the rotor structure should be established and applied to the proposed stator winding model. In addition, the impedance parameters between the three-phase winding and shaft end sides need to be extracted when the motor is operating because the bearing impedance characteristic can be different with the stationary state by the capacitance of the oil barrier. By using the five-port data of the operating state, the multi-port network parameter extraction method, which is proposed in section 3.4, can be applied to study the shaft voltage for the next step.

The EM field calculation method for the realistic stator and winding structure was proposed to predict the input impedance characteristic of the ac motor. The network parameters for the phase windings can be extracted from the proposed method, and it can be used in the circuit simulation with the other circuit component, such as source, inverter, or line impedance stabilization network (LISN) to predict the EMI characteristic of the motor drive system. From the circuit simulation of the motor drive system, not only the input impedance of the ac motor, but also the CM voltage or current in the system can be predicted.

The proposed EMC-aware motor design method was verified by measuring the CM current in the motor drive system. In the future work, the other EMI characteristics, such as CM or DM voltages also

need to be measured to assure the EMC design for the ac motor by using LISN. Moreover, the variation of the EMI characteristics should be observed through the change of the switching frequency with control circuit of inverter drive. In addition, the core loss and torque for the designed motor models were verified by simulation in this thesis. To enhance the proposed design method, the motor output performances of the designed ac motors should be validated by measurement.

REFERENCES

[1] G. L. Skibinski, R. J. Kerkman and D. Schlegel, "EMI emissions of modern PWM AC drives," in *IEEE Industry Applications Magazine*, vol. 5, no. 6, pp. 47-80, Nov.-Dec. 1999.

[2] M. C. Di Piazza, A. Ragusa and G. Vitale, "Common mode EMI propagation in high voltage DC supplied induction motor drives for electric vehicles application" in *Proceeding of 2009 IEEE International Electric Machines and Drives Conference*, Miami, FL, 2009, pp. 647-652.

[3] B. Mirafzal, G. L. Skibinski and R. M. Tallam, "A Failure Mode for PWM Inverter-Fed AC Motors Due to the Antiresonance Phenomenon," in *IEEE Transactions on Industry Ap plications*, vol. 45, no. 5, pp. 1697-1705, Sep.-Oct. 2009.

[4] (Picture) http://www.easa.com/resources/booklet/typical-failures-three-phase-stator-windings

[5] J, L. Guardado, V. Carrillo, and K. J. Cornick, "Calculation of interturn voltages in machi ne windings during switching transients measured on terminals," in *IEEE Transactions on Energy Conversion*, vol. 10 no. 1, pp. 87-94, Mar. 1995.

[6] E. Zhong, T. A. Lipo and S. Rossiter, "Transient modeling and analysis of motor terminal voltage on PWM inverter-fed AC motor drives," *Conference Record of 1998 IEEE Indust ry Applications Conference*, vol. 1, pp. 773-780, USA, 1998.

[7] G. Suresh, H. A. Toliyat, D. A. Rendusara, and P. N. Enjeti, "Predicting the transient effe cts of PWM voltage waveform on the stator windings of random wound induction motors," in *IEEE Transactions on Power Electronics*, vol. 14, no. 1, pp. 23-30, Jan. 1999.

[8] N. Mutoh, M. Ogata, K. Gulez and F. Harashima, "New methods to suppress EMI noises in motor drive systems," in *IEEE Transactions on Industrial Electronics*, vol. 49, no. 2, pp. 474-485, Apr. 2002.

[9] A. Videt, P. Le Moigne, N. Idir, P. Baudesson and X. Cimetiere, "A New Carrier-Based PWM Providing Common-Mode-Current Reduction and DC-Bus Balancing for Three-Level Inverters," in *IEEE Transactions on Industrial Electronics*, vol. 54, no. 6, pp. 3001-3011, Dec. 2007.

[10] D. Han, C. T. Morris and B. Sarlioglu, "Common-Mode Voltage Cancellation in PWM Motor Drives with Balanced Inverter Topology," in *IEEE Transactions on Industrial Electr onics*, vol. 64, no. 4, pp. 2683-2688, Apr. 2017.

[11] G. Ala, G. C. Giaconia, G. Giglia, M. C. Di Piazza and G. Vitale, "Design and Perform ance Evaluation of a High Power-Density EMI Filter for PWM Inverter-Fed Induction-Mot or Drives," in *IEEE Transactions on Industry Applications*, vol. 52, no. 3, pp. 2397-2404, May-Jun. 2016.

[12] J. Huang and H. Shi, "A Hybrid Filter for the Suppression of Common-Mode Voltage and Differential-Mode Harmonics in Three-Phase Inverters with CPPM," in *IEEE Transactions on Industrial Electronics*, vol. 62, no. 7, pp. 3991-4000, Jul. 2015.

[13] D. K. Sharma, G. G. Rhudy, and E. L. Owen, "Voltage distribution among the coils and turns of a form wound ac rotating machine exposed to impulse voltage," in *IEEE Transaction on Energy Conversion*, vol. EC-1, no. 2, pp. 50-60, June 1986.

[14] O. A. Mohammed, S. Ganu, N. Abed, S. Liu, and Z. Liu, "High frequency PM synchronous motor model determined by FE analysis," in *IEEE Transactions on Magnetics*, vol. 42, no. 4, pp. 1291-1294, Apr. 2006.

[15] K. Maki, H. Funato, and L. Shao, "Motor modeling for EMC simulation by 3-D electromagnetic field analysis," in *Proceeding of IEEE Electric Machines Drives Conference*, pp. 103-108, May, 2009.

[16] O. A. Mohammed, and S. Ganu, "FE-circuit coupled model of electric machines for simulation and evaluation of EMI issues in motor drives," in *IEEE Transactions on Magnetics*, vol. 46, no. 8, pp. 3389-3392, Aug. 2010.

[17] J. Sun, and L. Xing, "Parameterization of three-phase electric machine models for EMI simulation," in *IEEE Transactions on Power Electronics*, vol. 29, no. 1, pp. 36-41, Jan. 2014.

[18] A. F. Moreira, T. A. Lipo, G. Venkaratamanan, and S. Bernet, "High frequency modeling for cable and induction motor overvoltage studies in long cable drives," in *IEEE transactions on Industry Applications*, vol. 38, no. 5, pp. 1297-1306, Sep. 2002.

[19] A. Boglietti, A. Cavagnino, and M. Lazari, "Experimental high-frequency parameter identification of ac electrical motors," in *IEEE transactions on Industry Applications*, vol. 45, no. 1, pp. 23-29, Jan. 2007.

[20] M. Schinkel, S. Weber, S. Guttowski, W. John, and H. Reichl, "Efficient HF modeling and model parameterization of induction machines for time and frequency domain simulations," in *Proceeding of IEEE Applied Power Electronics Conference*, pp.1181-1186, Mar. 2006.

[21] N. Idir, Y. Weens, M. Moreau, and J. J. Franchaud, "High-frequency behavior models of ac motors," in *IEEE Transactions on Magnetics*, vol. 45, no. 1, pp. 113-138, Jan 2009.

[22] B. Mirafzal, G. Skibinski, R. Tallam, D. Schlegel, and R. Lukaszewski, "Universal induction motor model with low-to-high frequency-response characteristics," in *IEEE transactions on Industry Applications*, vol. 43, no. 5, pp. 1223-1246, Sep. 2007.

[23] B. Mirafzal, G. Skibinski, and R. Tallam, "Determination of parameters in the universal induction motor model," in *IEEE transactions on Industry Applications*, vol. 45, no. 1, pp. 142-151, Jan. 2009.

[24] Liwei W. C. N.-M. Ho, F. Canales, J. Jatskevich, "High-frequency modeling of the long-cable-fed induction motor drive system using TLM approach for predicting overvoltage transients," in *IEEE Transaction on Power Electronics*, vol. 25, no, 10, pp. 2653-2664, Oct. 2010.

[25] G. Suresh, H. A. Toliyat, D. A. Rendusara and P. N. Enjeti, "Predicting the transient effects of PWM voltage waveform on the stator windings of random wound induction motors," in *IEEE Transactions on Power Electronics*, vol. 14, no. 1, pp. 23-30, Jan. 1999.

[26] O. A. Mohammed, S. Ganu, N. Abed, S. Liu and Z. Liu, "High frequency PM synchronous motor model determined by FE analysis," in *IEEE Transactions on Magnetics*, vol. 42, no. 4, pp. 1291-1294, Apr. 2006.

[27] V. Mihaila, S. Duchesne and D. Roger, "A simulation method to predict the turn-to-turn voltage spikes in a PWM fed motor winding," in *IEEE Transactions on Dielectrics and Electrical Insulation*, vol. 18, no. 5, pp. 1609-1615, Oct. 2011.

[28] O. Magdun, S. Blatt and A. Binder, "Calculation of stator winding parameters to predict the voltage distributions in inverter fed AC machines," in proceeding of *2013 9th IEEE International Symposium on Diagnostics for Electric Machines, Power Electronics and Drives (SDEMPED)*, Valencia, 2013, pp. 447-453.

[29] N. Boucenna, F. Costa, S. Hlioui and B. Revol, "Strategy for Predictive Modeling of the Common-Mode Impedance of the Stator Coils in AC Machines," in *IEEE Transactions on Industrial Electronics*, vol. 63, no. 12, pp. 7360-7371, Dec. 2016.

[30] T. R. Kuphaldt, *Lessons In Electric Circuits, Volume II – AC*, 6th ed., Design Science L icense, 2007, pp. 418, 444.

[31] D. M. Pozar, *Microwave Engineering*, 4th ed., United States of America: John Wiley & Sons, 2011. pp. 48-51.

[32] W. R. Eisenstadt and Y. Eo, "S-parameter-based IC interconnect transmission line charact erization," in *IEEE Transactions on Components*, Hybrids, and Manufacturing Technology, vol. 15, no. 4, pp. 483-490, Aug. 1992.

[33] B. Revol, J. Roudet, J.-L. Schanen, and P. Loizelet, "EMI study of three-phase inverter-f ed motor drives," in *IEEE Transactions on Industrial Applications*, vol. 47, no. 1, pp. 223 -231, Jan.-Feb., 2011.

[34] A. E. Engin, W. Mathis, W. John, G. Sommer, and H. Reichl, "Closed-form network rep resentations of frequency-dependent RLGC parameters," *International Journal of Circuit Th eory and Applications*, vol. 33, pp. 463-485, Nov.-Dec., 2005.

[35] M. A. Gries, and B. Mirafzal, "Permanent magnet motor-drive frequency response charact erization for transient phenomena and conducted EMI analysis," in Proceeding of *2008 IE

EE Applied Power Electronics Conference and Exposition, pp. 1767-1775, Feb. 2008.

[36] B. Revol, J. Roudet, J.-L. Schanen, and P. Loizelet, "EMI study of three-phase inverter-fed motor drives," in *IEEE Transactions on Industrial Applications*, vol. 47, no. 1, pp. 223-231, Jan.-Feb. 2011.

[37] O. Magdun and A. Binder, "An iron core impedance model for calculating high frequency common mode currents and shaft voltages in inverter-fed AC machines," in proceeding of *International Symposium on Power Electronics, Electrical Drives*, Automation and Motion, pp. 135-140, Jun. 2012.

[38] D. Busse, J. Erdman, R. Kerkman, D. Schlegel, and G. Skibinski, "Characteristics of shaft voltage and bearing currents," in *IEEE Industry Applications Magazine*, vol. 3, no. 6, pp. 21-32, Nov/Dec 1997.

[39] M. J. Costello, "Shaft voltages and rotating machinery," in *IEEE Transactions on Industry Applications*, vol. 29, no. 2, pp. 419-426, Mar/Apr 1993.

[40] J. Adabi, F. Zare and A. Ghosh, "End-winding effect on shaft voltage in AC generators," in *proceeding of 2009 13th European Conference on Power Electronics and Applications*, Barcelona, 2009, pp. 1-10.

[41] U. T. Shami and H. Akagi, "Experimental Discussions on a Shaft End-to-End Voltage Appearing in an Inverter-Driven Motor," in *IEEE Transactions on Power Electronics*, vol. 24, no. 6, pp. 1532-1540, June 2009.

[42] U. T. Shami and H. Akagi, "Identification and Discussion of the Origin of a Shaft End-to-End Voltage in an Inverter-Driven Motor," in *IEEE Transactions on Power Electronics*, vol. 25, no. 6, pp. 1615-1625, June 2010

[43] (Picture) http://www.helwigcarbon.com/

[44] (Picture) http://www.baldor.com/

[45] G. Suresh, H. A. Toliyat, D. A. Rendusara and P. N. Enjeti, "Predicting the transient effects of PWM voltage waveform on the stator windings of random wound induction motors," in *IEEE Transactions on Power Electronics*, vol. 14, no. 1, pp. 23-30, Jan 1999.

[46] J. Pyrhonen, T. Jokinen and V. Hrabovcova, *Design of Rotating Electrical Machines*, 2nd ed., United Kingdom: John Wiley & Sons, 2014, pp. 293-330.

Acknowledgement

CURRICULUM VITAE

EDUCATION

2012.03 ~ 2018.08 Combined M.S-Ph.D in Department of Electronic Engineering,

Ulsan National Institute of Science and Technology (UNIST), Ulsan, Korea

Major: AC Motor EMC Design

Thesis Title: Impedance Characterization and Synthesis for the EMC-Aware Design of AC Motors

Advisor: Prof. Jingook Kim

1999.03 ~ 2008.02 B.S in Department of Electrical Engineering

University of Ulsan, Ulsan, Korea

PUBLICATIONS

[1] **Y. Ryu**, B.-R. Park, K. J. Han, "Estimation of high-frequency parameters of AC machine from transmission line model," in *IEEE Transactions on Magnetics*, vol. 51, no. 3, 8101404, Mar. 2015.

[2] **Y. Ryu**, S. Kim, G. Jeong, J. Park, D. Kim, J. Park, J. Kim, K. J. Han, "Common mode noise reduction for an LLC resonant converter by using passive noise cancellation," in *Journal of Electromagnetic Engineering and Science*, vol. 15, no. 2, pp. 89-96, Apr. 2015.

[3] **Y. Ryu**, K. J. Han, "Extraction of high-frequency phase-to-phase coupling in AC machine using mixed-mode network parameters," in *IEEE Transactions on Magnetics*, vol. 52, no. 3, 8102104, Mar. 2016.

[4] H.-P. Park, **Y. Ryu**, K. J. Han, J. Jung, "Design considerations of resonant network and transformer magnetics for high frequency LLC resonant converter," in *Journal of Electrical Engineering & Technology*, vol. 11, no. 2, pp. 383-392, Mar. 2016.

[5] K. J. Han, **Y. Ryu**, H. Jo, "High-Frequency Modeling of AC Motors for EMC-Aware Design of Electrical Drives," in *Proceeding of 2015 Korea-Japan Joint Conference on EMT/EMC/BE (KJJC-2015)*, pp. 13-16, Sendai, Japan, Nov. 2015.

[6] **Y. Ryu**, K. J. Han, "High-Frequency Stator-to-Frame Admittance Modeling for AC Machine by Using Debye Model," in *Proceeding of 2016 Asia-Pacific International Symposium on Electromagnetic Compatibility (APEMC 2016)*, Shenzhen, China, May 2016.

[7] **Y. Ryu**, K. J. Han, "Improved Transmission Line Model of the Stator Winding Structure of an AC Motor Considering High-frequency Conductor and Dielectric Effects," in *Proceeding of IEEE International Electric Machines & Drives Conference (IEMDC 2017)*, Miami, FL, USA, May 2017.

[8] **Y. Ryu**, K. J. Han, "Extraction of Network Parameters for the Winding-to-Shaft Coupling Effect of an AC motor," in *Proceeding of 2017 Asia-Pacific International Symposium on Electromagnetic Compatibility (APEMC 2017)*, p. 216, Seoul, Korea, Jun. 2017.